Proceedings of the 16th European Inter-Regional Conference of Ceramics CIEC16

CIEC16

Torino

CIEC 16

Proceedings of CIEC 16

16th European Inter-Regional
Conference of Ceramics

Torino, 9-11 September 2018

POLITECNICO DI TORINO

DiSAT

JECS Trust

Proceedings of CIEC 16
European Inter-regional Conference on Ceramics
Torino, 9-11 Septembre 2018

_____

Editorial

This e-book collects the extended abstracts of some of the oral and poster presentations, which have enlived the 16th International Inter-Regional European Conference on Ceramics, CIEC 16, held in Torino, Italy, from 9 to 11 September 2018.

The European Inter-Regional Conference on Ceramics (CIEC) is organised every two years, and it has a quite long history, starting from the will of some scientists, belonging to few founding European Regions.

A first meeting involving Baden–Württemberg and Rhône-Alpes was held in Karlsruhe, in 1989; in the same year, a COTRAO (Piemonte, Canton de Vaud, Rhône-Alpes) meeting was organized in Torino. The first appearance of the acronym CIEC (Colloque Interrégional Européen sur les Céramiques, European Interregional Conference on Ceramics) in 1991, is associated to the organization of the conference CIEC3, held in Lyon, and collecting the contributions from several regions, such as Baden-Württemberg, Catalunya, Canton de Vaud, Liguria, Lombardia, Piemonte, Rhône-Alpes.

The following conferences are here listed: CIEC 4, in Salou (1993), with the participation also of Provence-Alpes-Côte d'Azur; CIEC 5, Toulon (1996); CIEC 6, Stuttgart (1998); CIEC 7, Genova (2000), with the involvement also of Wales; CIEC 8, Lyon (2002); CIEC 9, Bardonecchia (2004); CIEC 10, Swansea (2006); CIEC 11, Lausanne (2008), involving also Wallonia/Hainault; CIEC 12, Mons (2010); CIEC 13, Barcelona (2012); CIEC 14, Stuttgart (2014); CIEC 15, Lyon (2016).

The number of Regions involved increased during time and now they are Baden-Württenberg, Catalunya, Canton de Vaud, Wallonia/Hainaut, Lombardia, Piemonte, Rhône-Alpes, Styria, Wales.

CIEC 16 has been held in Torino, Italy, on September 9-11, 2018 at the Valentino's Castle, an UNESCO's World heritage, and the historical seat of the Politecnico di Torino, the hosting Institution.

The Conference covered the major themes of basic research and technology advancements in ceramics, including powder development, processing and forming, conventional and non-conventional sintering procedures, mechanical and functional characterizations, properties optimization, components development and industrial applications of monolithic and porous ceramics, and CMC.

This Conference was mainly aimed to promote exchanges and cooperation among European research groups, to support their networking and the development of joint projects at a European level, as well as to create a friendly meeting place for young researchers.

2

_____

A special session of CIEC16 was dedicated as a tribute in memory of Prof. Paolo Nanni, an Italian outstanding scientist who strongly contributed to the establishment of the European network supporting CIEC initiatives.

We are grateful to:

- the International Scientific Committee, to have supported the local organizing committee in assuring a very high quality of the scientific communications presented during the conference;
- the invited speakers, for their outstanding contributions;
- the JECS Trust, for the relevant support in fostering the participation of young scientists and for awarding some prizes to the best oral as well as poster presentations;
- Politecnico di Torino, to have supported the organization of this event.

Paola Palmero
Jean-Marc Tulliani
Laura Montanaro
Politecnico di Torino

_____

Index

4

_____

_____

5

_____

Advanced experimental techniques for monitoring the initiation and progression of damage in ceramic matrix composites

M. R. Bache

Institute of Structural Materials. Swansea University, Swansea, SA1 8EN, UK

Abstract
Ceramic matrix composites (CMCs) continue to attract attention for their potential employment in high performance engineering applications. A critical contribution to gaining confidence in these materials is acquired via mechanical property testing employing a range of test coupons in the laboratory. Standard test procedures have been developed for CMC assessment, to describe methods of monotonic, low and high cycle fatigue, creep and complex thermo-mechanical loading regimes. These various tests generate invaluable data to describe mechanical performance across a wide range of temperatures and environments.

However, to gain an improved understanding of mechanical behaviour usually requires some form of ancillary measurement alongside the basic definition of time or cycles to failure as controlled by the stress or strain conditions employed. So for example, extensometry has long been employed as a means of measuring bulk strain accumulated within the critically stressed volume of a test specimen. Over the past two decades in particular, damage monitoring techniques have become ever more sophisticated to the extent that localised and anisotropic strains developed in these highly complex architectures can be recognised and progressively monitored through to ultimate failure as a function of time or cycles.

The present paper will focus upon the employment of specific techniques employed in our laboratory for the detection of damage, employing a variant of the SiC_f/SiC system as the demonstration vehicle. The complimentary nature of these monitoring techniques will be emphasised in order to gain a detailed understanding of initiation and progression.

Keywords
Ceramic matrix composite (CMC); digital image correlation (DIC); acoustic emission (AE); electrical resistance (ER); in-situ scanning electron microscopy (I-SSEM).

Introduction
With reference to high performance engineering applications where long-term exposure to high temperature environments is envisaged, fibre reinforced ceramic matrix composites (CMC's) offer a unique combination of low density and thermal stability when compared to traditional metallic systems. The composite nature of CMCs offers an improvement in damage tolerance over and above that of their monolithic counterparts, however, the high cost of the raw constituents (particularly the high quality fibres) together with expensive processing routes has limited the engineering interest to aerospace, power generation and high end automotive sectors to date.
Mechanical assessment of CMCs on the laboratory scale has relied upon relatively established forms of monotonic, fatigue and creep testing, albeit often employing

6

_____

extremes of test temperature to match the potential service conditions. Such studies have often been reported at previous CIEC meetings (particularly from the research teams based in the Universities of Lyon, Stuttgart and Swansea) and together with wider research on the International stage have guided incremental improvements in mechanical capability. A gradual increase in composite strength, ductility and resistance to creep, achieved largely through the optimization of the reinforcing fibres and fibre/matrix interfaces, has been characterized over the period. Associated experimental techniques have relied upon measurements of bulk deformation through the employment of extensometry. However, the initiation and progression of damage in these complex structural materials is far from homogeneous.

Swansea based research has been driven towards obtaining an improved understanding of the onset and progression of damage, in order to achieve these goals a number of advanced monitoring techniques are now employed on a routine basis. These techniques include combinations of: electrical resistance (ER); acoustic emission (AE); digital image correlation (DIC); X-ray tomography (XCT) and in-situ scanning electron microscopy (I-SSEM). Although independent techniques in their own right, various combinations of these methods offer improved understanding of the damage mechanisms controlling structural integrity in CMCs. This will be demonstrated using a two dimensional reinforced SiC_f/SiC CMC system incorporating 0° and 90° woven fibre tows as a demonstration material.

7

Electrical resistance (ER)
Potential drop monitoring of crack initiation and growth in metallic test specimens is a common technique employed to define damage tolerant behavior. Although the electrical conductivity is relatively low, similar PD based approaches can still be applied to silicon carbide based CMCs. Current and/or voltage/resistance monitoring probe attachment is more difficult but can be achieved using various mechanical fixings or conductive adhesives depending on the temperature of assessment. A progressive increase in specimen resistance is illustrated in Figure 1 as a function of fatigue life, for a plain SiC_f/SiC coupon tested at room temperature [1]. The "resistance curve" takes a sigmoidal form, with high rates of accumulation marking the initial and final stages of material response and a relatively steady state condition between. This change in resistance is a direct response to the reduction in effective cross section conducting the constant applied current as cracks initiate and grow throughout the structure. The onset of failure in this particular specimen may have been predicted from the increase in resistance rate at approximately 18,500 cycles.

Acoustic Emission (AE)
Given the predominantly elastic properties of the two main constituents, i.e. the silicon carbide matrix and fibres which in isolation would both fail in a catastrophic fashion, the onset of cracking and detection of the associated acoustic emissions is easily monitored. The monitoring sensors can be attached directly to the test coupon

_____

or if necessary to the adjacent mechanical grip assembly, especially useful under some high temperature test scenarios. A single sensor is sufficient to detect damage events within the specimen, however, multiple sensors are preferred to allow time of flight analysis between the opposing sensors and therefore definition of the event location, typically within an accuracy of +/- 1mm. The most advanced AE equipment interfaced to sophisticated waveform analysis can even identify differences between matrix and fibre fracture events [2].
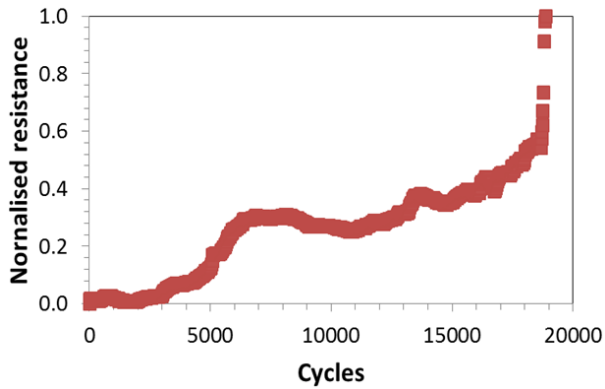
Fig. 1. ER data for a fatigue test. test).
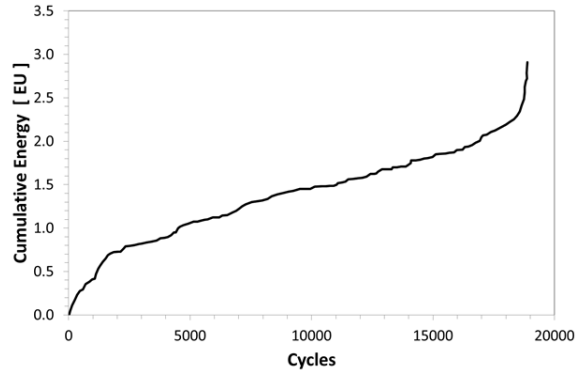
Fig. 2. Cumulative AE data (same test).

By plotting the cumulative energy associated with each successive acoustic event the progressive nature of damage can be seen as a function of fatigue life. Figure 2 illustrates this for the same test previously described by the ER technique in Figure 1. A broadly similar temporal trend is noted in the damage detection, with a marked increase in AE during the early stages of life plus a sharp acceleration in AE energy immediately prior to failure.

8
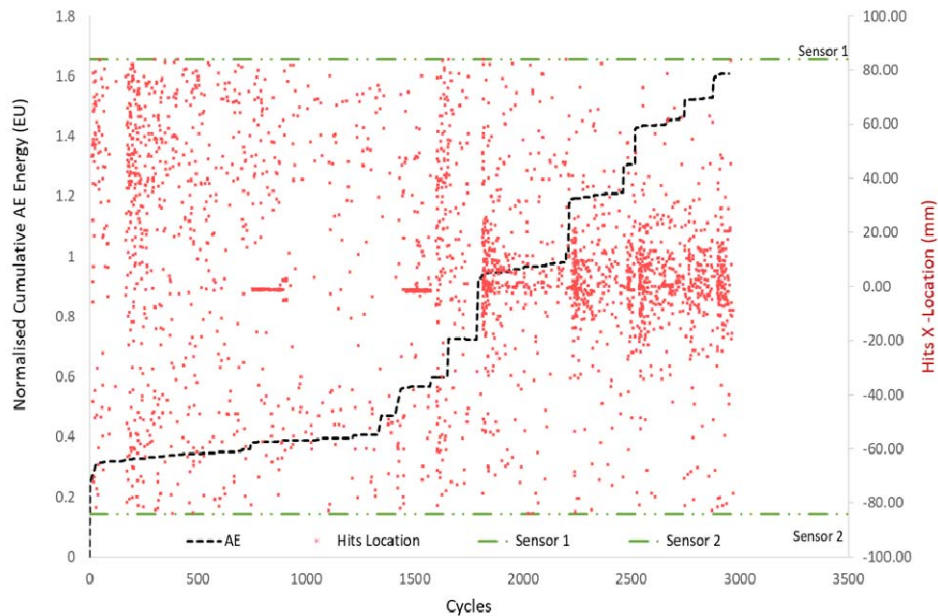
Fig. 3. Individual and cumulative acoustic energy signals from a fatigue test.

Both temporal and spatial representation of AE data from a different test are illustrated in Figure 3 [3]. Each data point represents a single event with respect to fatigue cycle and position relative to the gauge section of the specimen. The distribution of damage throughout the gauge volume is evident. This is a pertinent feature of the AE technique, identifying damage (often sub-surface) that would normally be undetected by optical inspection. Distinctive steps in this specific AE data are noted, presumably related to significant cracking events. Such steps are often induced with deliberate increases in peak applied load, for example, under stepped load fatigue testing. During the latter stages of the test the individual damage events become concentrated around the central plane of the gauge section, the region where catastrophic failure eventually occurred in this specimen.

Digital Image Correlation (DIC)
Considering the multi-phase nature of CMCs and the complex structural fibre reinforcement architecture, strain accumulation is naturally inhomogeneous. The volume of material sampled by contact extensometry or even miniature strain gauges will be too large to resolve the localised strains developing during loading. By sequential comparisons of digital images of the surface of the deforming test specimen with reference to the original un-deformed state, digital image correlation (DIC) is a powerful technique for detecting elastic and plastic strain which can eventually initiate cracking in the composite. High quality optics are required to record the sequence of images and the surface of the specimen may need coating with a speckle pattern prior to testing, unless sufficient surface detail is inherent following processing. The line of sight between the optical system and the specimen is rarely problematic under room temperature testing. However, to apply DIC to high temperature tests usually requires a ported furnace with suitable quartz window, optical filters and controlled exposure to alleviate the effects of thermal drift and black-body radiation on imaging. Once optimized, successful DIC monitoring on CMCs can be achieved at temperatures exceeding 1000°C [3].

When successful, DIC can detect the early stages of localised strain well before cracking occurs and even then, visual confirmation of fracture is extremely difficult by typical optical means. The resulting strain distribution is controlled by the matrix/fibre architecture, either randomly distributed throughout the gauge section of a plain specimen or concentrated close to stress raising features in geometries incorporating holes or notches. Figure 4 illustrates a sequence of DIC images, mapping strain distribution in a waisted coupon under monotonic loading through to the point immediately prior to ultimate failure [4]. Under progressive loading, damage becomes concentrated within a relatively confined zone through which the critical, unstable crack eventually forms. In this specific composite, the early matrix damage and cracking was predominantly focused on the transverse fibre tows.
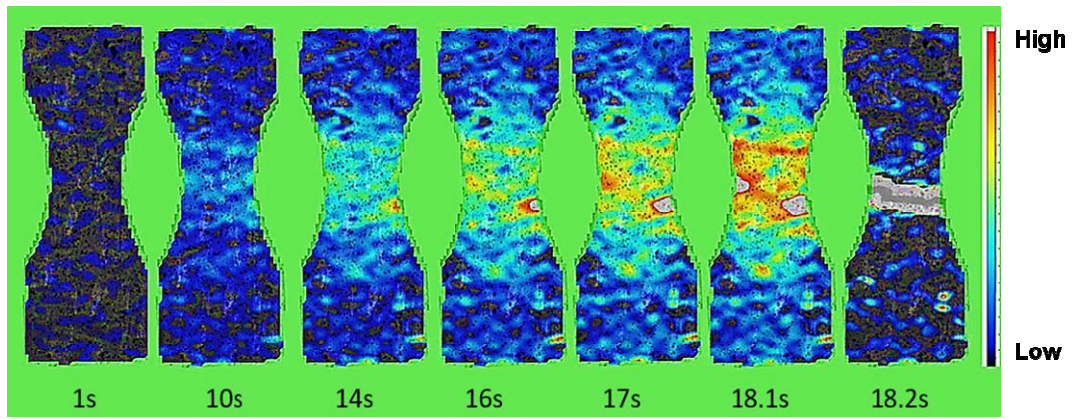
Fig. 4. Strain evolution during a monotonic test monitored by DIC.[4]

X-ray Computed Tomography (XCT)

A combination of damage monitoring techniques, e.g. ER, AE and DIC, can be employed as a means to terminate static or fatigue tests prior to ultimate failure, allowing for subsequent high resolution inspection via computed tomography (XCT). This allows for correlations between DIC strain measurements and the detection of cracking in particular. XCT has helped to define the highly complex nature of fracture. Crack bridging by 0° fibres is clearly identified and cracks will naturally bifurcate on to multiple planes orthogonal to the tensile axis as they advance through the composite. Even when initiating from a high stress concentration feature (for example the notch of a compact tension style specimen) the crack will rarely form a simple profile through the coupon thickness, e.g. Figure 5, illustrating crack growth from the pre-machined notch of a CT specimen tested under fatigue [1].
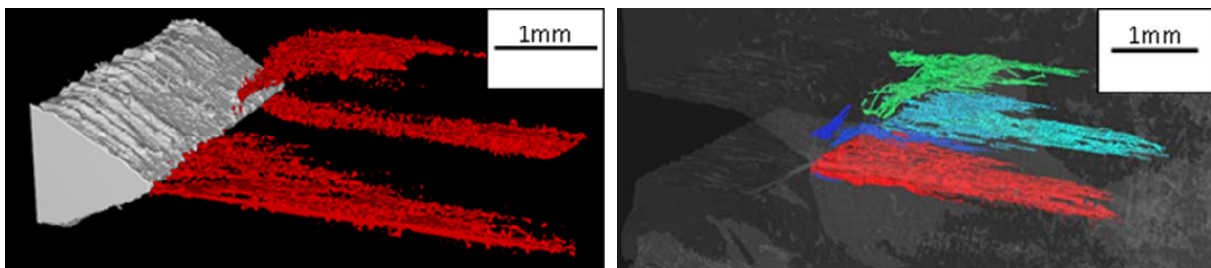
Fig. 5. XCT imaging of fatigue cracking from a sharp notch (CT specimen).

Retrospective XCT inspection of post tested specimens cannot, however, guarantee that all pre-existing cracks can be detected. This is now apparent since our recent studies [5] incorporating XCT imaging of specimens whilst under load, Figure 6. This example from a monotonic test with scans taken at four intervals (whilst the specimen is held under stationary displacement to allow XCT acquisition) demonstrates the early onset of cracking and progressive crack opening. Upon returning to zero load, however, many of the existing cracks become undetectable having fully closed along their crack wake, Figure 7. Similar networks of cracks were detected in fatigue specimens, with the earliest cracks appearing during loading within the very first cycle, Figure 8. This specimen was subsequently loaded for 650 cycles and re-inspected. The density of the crack network had increased, individual cracks demonstrated clear opening displacement and after unloading crack closure was again evident.
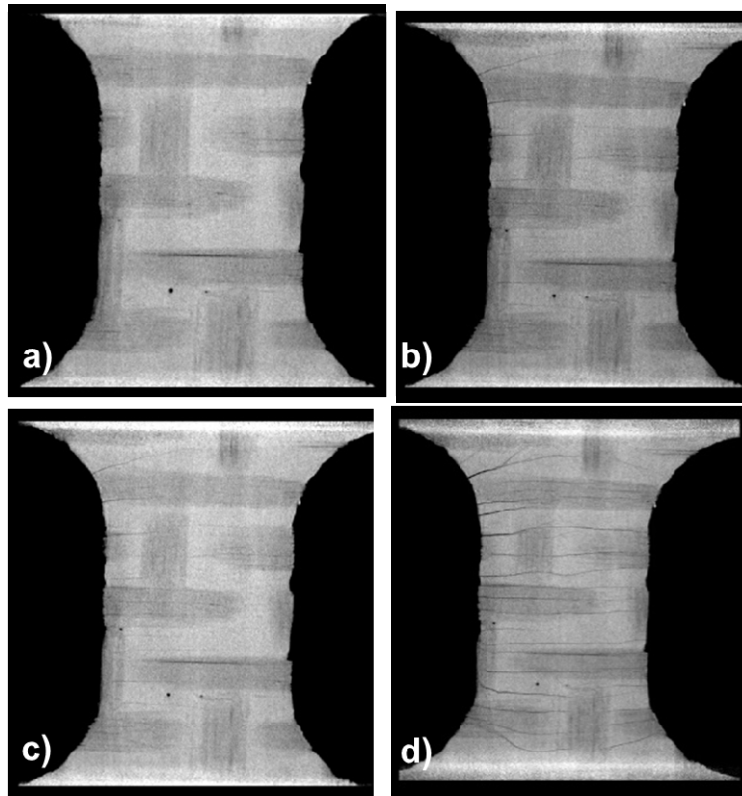
Fig. 6. XCT imaging of crack development under staged monotonic loading.
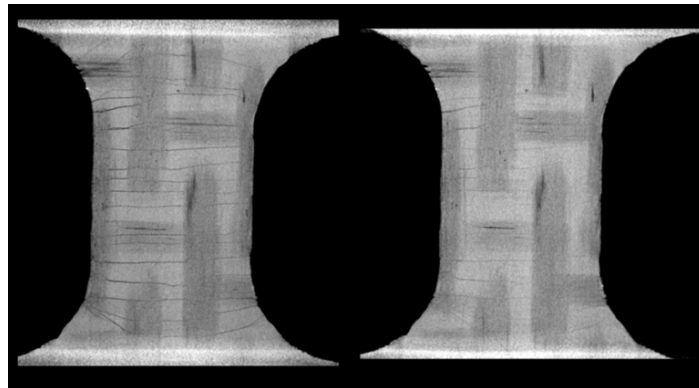
Fig. 7. XCT evidence for crack closure.
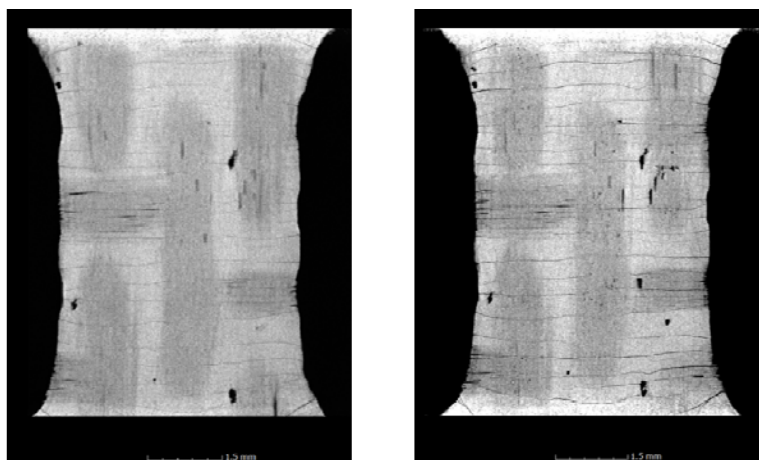
Fig. 8. Cracks initiated at N=1 (left) and after 650 cycles (right) of a fatigue test.

In-situ scanning electron microscopy (I-SSEM)

Our experience of inspecting cracking in CMCs by XCT whilst the specimen remains under load has led to the use of a miniature tensile loading stage within a scanning electron microscope [6]. Without applied load, the detection of surface cracks in post tested CMC specimens is inherently difficult, even under the relatively high magnification offered by SEM equipment. Figure 9a acts as an exemplar of these difficulties. A network of cracks is known to be present along the top edge of this specimen, however, their brittle nature with no accompanying plasticity or debris wedging along the crack wake makes them virtually invisible against the background of the silicon rich surface. Their presence becomes apparent upon loading in the SEM, however. The capture of sequential SEM images also allows for analysis of local strain distribution via digital image analysis, Figure 9b. Extended regions of high strain are noted orthogonal to the tensile load axis and distributed along the gauge section of the specimen. These regions initiate cracks, eventually becoming visible under increasing load levels. The superior resolution and depth of field of the SEM can then be utilized to view the condition of sub-surface bridging 0° fibres, with some individual fibres demonstrating fracture, Figure 10.
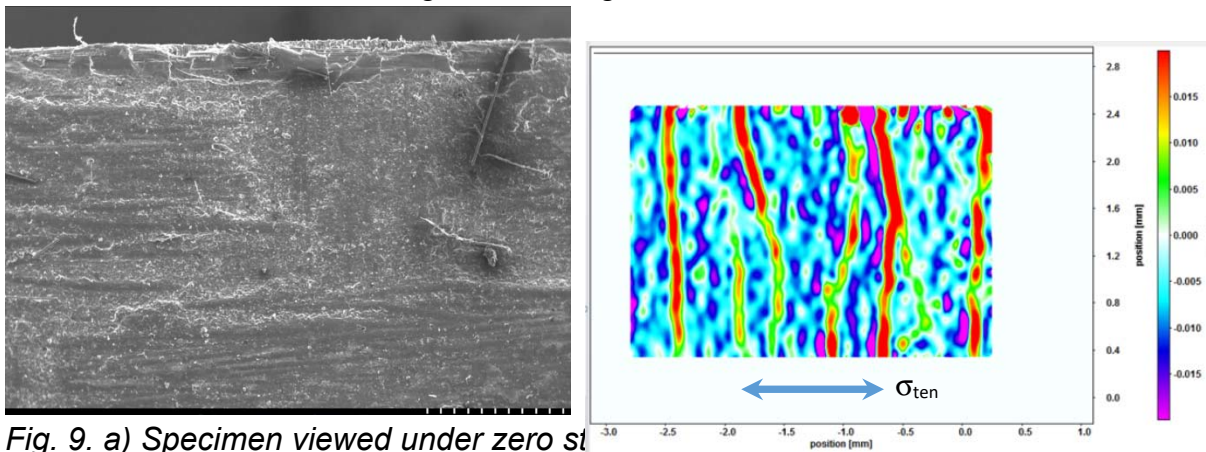
Fig. 9. a) Specimen viewed under zero st[...]
loading and analysed via DIC (right).
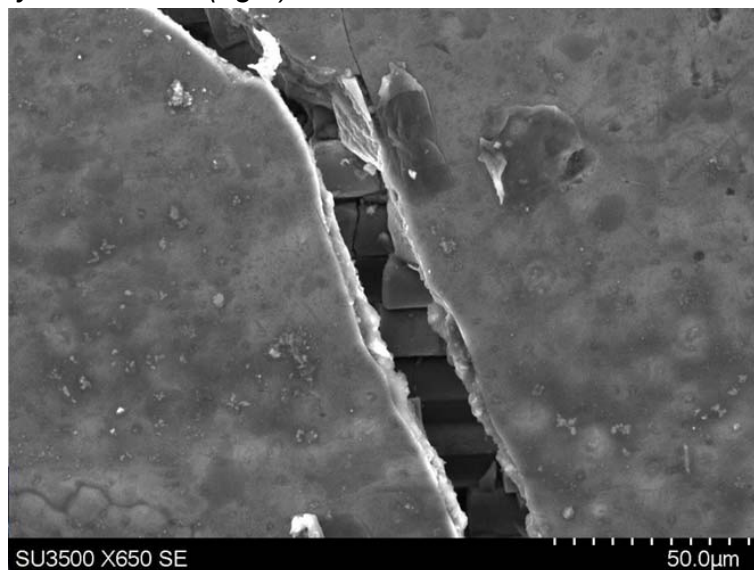
Fig. 10. Sub-surface fibres exposed under in-situ loaded SEM inspection.

13

Summary

A variety of inspection and measurement techniques and their employment for the characterization of CMCs have been described. Over the past two decades in particular, the resolution of such methods have improved. But also, ergonomic improvements to the user interface and control systems have proven beneficial to the investigator and many of the techniques described can be automated alongside long term creep and fatigue experiments. No single technique stands out as being more reliable for the detection and monitoring of damage in these materials, rather, a comprehensive understanding of material behaviour is gained by adopting a number of these in combination. The accumulation of critical strains, localized in nature but distributed throughout the critically stressed volume, is an important pre-cursor to the initiation of matrix cracks and clearly identified using digital image correlation. The temporal and spatial distribution of cracks within the volume is best identified through acoustic emission. XCT and optical inspections are able to illustrate the form and location of cracking to the user, however, the critical role played by in-situ inspection to detect cracks whilst remaining under load has been demonstrated.

14

References

[1] M.R. Bache, Z. Quiney, J.P. Jones and L. Gale; "Damage Development in SiC$_f$/SiC Composites Through Mechanical Loading", in Proc. of ASME Turbo Expo 2017: Turbomachinery Technical Conference and Exposition, GT2017, June 26-30, 2017, Charlotte, NC, USA, GT2017-64370.

[2] M.P. Appleby, D. Zhu, G.N. Morscher. Mechanical properties and real-time damage evaluations of environmental barrier coated SiC/SiC CMC's subjected to tensile loading under thermal gradients, Surf. Coat. Tech. 284. (2015). 318-326.

[3] C.D. Newton, L. Gale, J.P. Jones & M.R. Bache, "Detection Of Strain And Damage Distribution In SiC$_f$/SiC Mechanical Test Coupons", Proceedings of ASME Turbo Expo 2018: Turbomachinery Technical Conference and Exposition, GT 2018, June 11-15, 2018, Oslo, Norway, GT2018-75791.

[4] C.D. Newton, J.P. Jones, A.L. Chamberlain & M.R. Bache, "Inhomogeneous Strain Distribution in SiC$_f$/SiC Coupons Under Tensile Loading", in Proceedings of ASME Turbo Expo 2017: Turbomachinery Technical Conference and Exposition, GT 2017, June 26-30, 2017, Charlotte,NC, USA, GT2017-63045.

[5] M.R Bache, P.I. Nicholson & E. Williams, "In-situ Assessment of Fracture in SiC$_f$/SiC Under Computed X-Ray Tomography", in Proceedings of ASME Turbo Expo 2018: Turbomachinery Technical Conference and Exposition, GT2018, June 11-15, 2018, Oslo, Norway, GT2018-75795.

[6] S. Jordan, C.D. Newton, M.R.Bache and L. Gale; "In-situ Tensile Testing of SiC$_f$/SiC Specimens Using a Tensile Test Stage within a Scanning Electron Microscope", in Proc. CIEC 16, Torino, Italy, September 9-11, 2018 (this volume).

Mechanical Spectroscopy in Cemented Carbides and physical interpretation of their mechanical properties

D. Mari[1]

[1] *IPHYS, Station 3, Ecole Polytechnique Fédérale, Lausanne, Switzerland, daniele.mari@epfl.ch*

Abstract

Composites made of transition metal carbides, with a ferrous metal binder, commonly defined as hardmetals, are used for cutting tool applications. We investigate the mechanical behavior of the two main families of hardmetals: the cemented carbides, constituted of WC-Co, and the cermets made of a combination of TiC-TiN-(Co,Ni). The mechanical behavior of hardmetals is controlled by the microstructure of the constituents. The mechanical spectroscopy is a technique that is very sensitive to the movement of crystal defects. By measuring the damping capacity as a function of temperature or time and frequency, one can detect when a specific defect becomes mobile. Therefore, a series of damping peaks can be successively associated with the movement of dislocations in the cobalt, the sliding of WC or TiCN grain boundaries at high temperature. The movement of the dislocations in the cobalt at intermediate temperature is beneficial to the toughness since the WC skeleton maintains its cohesion. Instead, at high temperature, grain boundary sliding (GBS) leads to the decohesion of the WC skeleton and finally extensive plastic deformation is observed. It is interesting to notice that the cobalt plays a major role in (GBS) by progressively infiltrating the WC-WC grain boundaries. The presence of a coating (supposed to prevent from surface wear) also modifies the motion of defects in the cobalt phase. A recent study seems to prove a direct link between the tool life and the dislocation dynamics in the cobalt in presence of a coating.

15

Keywords

Internal friction, cobalt, tungsten carbide, grain boundary sliding, cutting tools

Introduction

Composites made of transition metal carbides with a ferrous metal binder are widely used for the manufacturing of cutting tools. They are commonly defined as hardmetals. Among them, two main families of materials can be distinguished: the cemented carbides, mainly constituted of WC-Co, and the cermets made of a combination of TiC-TiN-(Co,Ni) with other carbides [1]. The main qualities required for a cutting tool are a good toughness and a good resistance to deformation at high temperature. The cemented carbides have a very high toughness and good hardness. However, the performances of such materials are rapidly deteriorated when high cutting speed and high temperatures are involved, because WC-Co has a poor chemical resistance and undergoes plastic deformation at high temperature [2].

_____

This is why most of cemented carbides are coated to prevent from wear. The cermets have in general a better resistance to high temperature deformation but toughness is lower than in cemented carbides. The morphology of hardmetals is well described by a structure made of two interpenetrated skeletons: the ceramic and the metal ones. The ceramic skeleton is an arrangement of joined single-crystal carbide or carbonitride grains. In WC-Co, grains are faceted with triangular or rectangular shape revealing the hexagonal structure of WC. In TiCN based composites, the grains have a core-rim structure where the core corresponds to pure TiCN and the rim to (Ti,M)CN precipitated during solid-liquid phase sintering [3-5]. M represents a transition metal carbide former. Fig. 1 shows the typical morphology of a cemented carbide and of a cermet. The changes of the mechanical properties with temperature can be summarized by Table 1 [6].

Table 1. Schematic description of the changes of the mechanical properties of different cermets or cemented carbides as a function of temperature.

Mechanical spectroscopy is a powerful tool to analyse the properties and the evolution of these composite materials since its spectroscopic character allows the separation of the microplasticity mechanisms that occur in each phase. A wide range of hardmetals has been studied to date [6, 7]. The analysis of internal friction spectra is complex because of the wide range of phenomena that may occur in such composite materials. The purpose of this paper is to show a unified view of the mechanism underlying the internal friction spectra. Only the comparison of the spectra obtained in different materials allows the attribution of each internal friction peak to a specific phase and mechanism in the composite. Such analysis is extremely fruitful if compared with macroscopic mechanical properties and improves the understanding of the evolution of the hardmetals with temperature.

Experimental techniques and materials
Different hardmetals are presented in this study as summarized in Table 2. Samples were produced by sintering at a typical temperature of 1673 K for WC-Co and 1723 K for the cermets. The samples for internal friction (IF) measurements were spark-cut

_____

at the final dimension of 1x4x40-60 mm³. In order to separate the effect of the ceramic skeleton from that of the binder, the metal phase was extracted from the IF samples by chemical etching with boiling concentrated HCl. Mechanical spectroscopy was performed in a sub-resonant, forced, inverted torsion pendulum [6]. Measurements were carried out at constant heating rate (1 K/min.) and at a frequency of 1 Hz in a temperature range from 300 K to 1500 K, and isothermally in a frequency range from 1 mHz to 10 Hz. In forced mode, the IF is measured by the tangent of phase lag: tan(δ).

Alloy:	Co/Ni	W	Ti	Mo	N	C
WC-18Co	16.93	41.53	0.00	0.00	0.00	41.53
WC-10Co	9.71	45.15	0.00	0.00	0.00	45.15
TiCN6Mo18Co	9.13	0.00	38.96	3.65	11.69	26.99
TiCN5WC10Co	9.13	3.92	42.08	0.00	16.41	28.46

Table 2. Composition of the alloys presented in this work. Phase fractions are given in at.%. The grade denominations instead refer to vol.%. In TiCN-based cermets, the ratio C/N is 30/70.

17
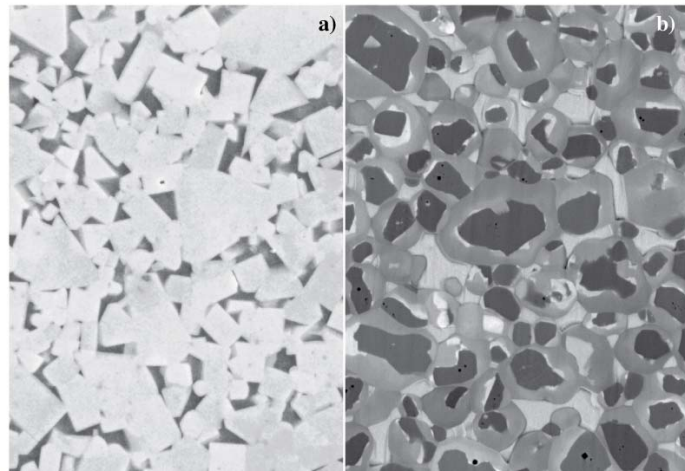
Fig. 1. Grain structure of a) WC-18Co cemented carbide and b) TiCN5WC10Co cermet. The cobalt is bright in the cermet and darker in the WC-Co. In the cermet, the typical core-rim structure can be observed

The spectra obtained both from frequency and temperature scans are deconvoluted into several, possibly broadened, Debye peaks, each of which is described by a function:

$$tg(\delta) = \Delta \frac{(\omega\tau)^{\alpha}}{1+(\omega\tau)^{2\alpha}} \qquad 0 < \alpha \leq 1 \qquad (1)$$

where Δ is the relaxation strength, ω the angular frequency, τ the relaxation time and

$1/\alpha$ the broadening factor [8]. For a thermally activated mechanism, the relaxation time depends on temperature according to an Arrhenius law

$$\tau = \tau_0 \, e^{\frac{E_{act}}{kT}} \qquad (2)$$

where E_{act} is the activation energy, k is Boltzmann's constant and τ_0 is a constant corresponding to the inverse of the attempt frequency n_0.

Results and discussion

A characteristic spectrum of WC-18Co is presented in fig. 2. In the first heating (curve A), only a bump at 1150 K can be clearly distinguished. A peak PW_1 is better defined in the second heating with maximum at 1100 K (curve B). The spectrum of curve B is stable during the following heating-cooling cycles. However, if the sample undergoes a long annealing at 1000 K, a new spectrum characterized by a peak at 900 K is obtained. Curve C clearly shows a transition at 1050 K between the two spectra. If the sample is heated above 1050K the curve B is obtained again. The spectrum of the WC skeleton does not show any of the above features but some increasing background above 1100K.

18
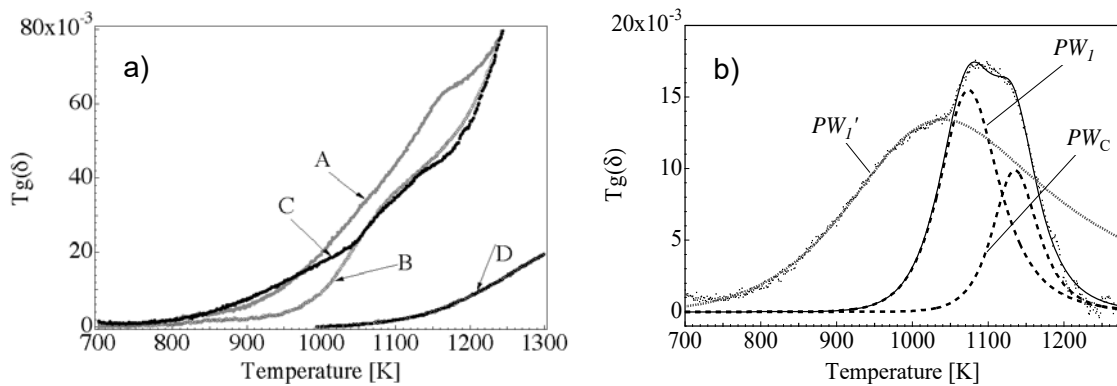
Fig. 2. a) Internal friction spectra in a WC-18Co measured at 1 Hz as a function of temperature upon heating. Curve A represents the as received state. Curve B is observed after heating above 1200 K and is stable. Curve C is obtained from status B after annealing for 72 hours at 1000 K. Curve D represents the internal friction of the WC skeleton. b) Deconvolution of the internal friction spectrum shown in curve C after high temperature background subtraction.

In order to better extract the information provided by the IF spectra, the high temperature part of them can be assimilated to an exponential background and subtracted. Fig. 2b shows the spectrum of WC-18Co (curve C) after subtraction of the background. We can observe more clearly the transition from the low temperature state to the high temperature one at 1050 K. In order to drive the analysis of the spectrum, a peak is fitted to the low temperature part of the spectrum

and two are fitted to the high temperature state. The peak Pc has been introduced in the deconvolution based on the fact that the magnetic transition of the cobalt in WC-Co is expected at that temperature [9].

The peaks located between 900 K and 1200 K in Fig 2b should be attributed to the cobalt phase since they depend on the binder content and they are absent when the cobalt is etched (Fig. 2a) Clearly, the spectrum in Fig. 2b shows a transition at about 1050 K between two states of the material represented by the low temperature peak PW_1' that is replaced by PW_1 at higher temperature. These peaks should be attributed to the same defect. This transition in the binder behavior was first evidenced by Schaller et al. [10] and attributed to a change in solute W concentration together with a change in the dislocation structure from partial dislocations to recombined perfect dislocations [6, 11, 12]. The sharp peak that appears clearly at 1170 K (fig. 2b) should be attributed to the magnetic transition at the Curie temperature of the cobalt according to the interpretation of Gardon [9]. However, magnetic effects can produce a decomposition of Co-W that was first proposed in the calculation of phase diagram by Guillermet [13]. A ferromagnetic W-poor and a paramagnetic W-rich phase should form in fcc cobalt together with WCo_3. Östberg et al. [14] have given experimental evidences of the presence of bands in the cobalt phase of a cermet with periodically fluctuating W concentration. Therefore, we can envisage that annealing the material at 1000 K promotes such spinodal decomposition. The diffusion of W is however very sluggish and long annealing times are needed to obtain such microstructure. The presence of bands with different W densities would have a strong influence on the mechanical properties and on the dislocation dynamics. In [15], it was demonstrated with a number of details that indeed a spinodal decomposition in the cobalt binder justifies the presence of short dislocation segments at lower temperature. With the disappearance of the spinodal structure, longer free dislocations segments can be formed and the peak shifts at higher temperature. Obviously, this behavior is controlled by the amount of W that is dissolved in the cobalt. If more W is dissolved in the cobalt, the Curie temperature drops and only the paramagnetic phase is present. This phase is still characterized by the presence of a high density of stacking faults and the peak PW_1' becomes stable. A recent study (S. Adjam et al., this conference) shows that the features of this peak and in particular its temperature allow to predict the tool life. The lower the temperature of the peak, the longer the tool life. Since, the mechanism giving rise to PW_1' is the movement of stacking faults, it can be argued that stacking faults or hexagonal cobalt strongly harden the cobalt but decrease its toughness contribution to the composite.

A typical spectrum of TiCN6Mo18Co is shown in Fig. 3a. It shows two peaks PT_1 and PT_2 respectively at 1000 K and 1200 K and a background. The first peak PT_0 is also found in the skeleton spectrum while other features are less clearly visible. On the second heating, the peak PT_0 has disappeared making PT_1 more visible.

In the TiCN-Mo-Co alloys, the peak PT_1 has never shown a behavior similar to PW_1 even if from the phase diagram an equivalent spinodal decomposition could be

19

expected [16]. This peak was attributed to Mo dragging by dislocations [17]. The peak PT$_0$ is only observed in Co-based cermets. It characterizes the as sintered structure and disappears after the first heating above 1000 K. This peak is generally sensitive to material chemistry. It increases with the cobalt content and, it depends strongly on the nitrogen content in the ceramic phase. It was shown previously [17] that a thin cobalt film can be detected at grain boundaries when the peak is present.
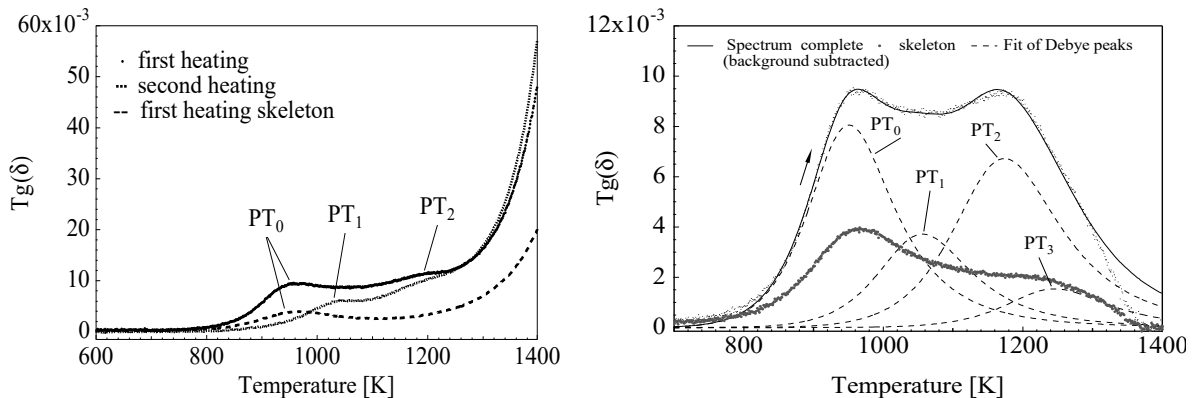
Fig. 3. a) Internal friction spectrum of TiCN6Mo18Co measured at 1 Hz upon heating. In the first heating, two peaks PT$_0$ and PT$_2$ can be distinguished. In the second heating, PT$_0$ is missing and reveals the presence of PT$_1$. PT$_0$ is also clearly present in the TiMoCN skeleton obtained by etching the binder. b) Deconvolution of the internal friction spectrum and of its respective TiMoCN skeleton after high temperature background subtraction (first heating). Four peaks can be fitted in the complete material but PT$_1$ is absent in the skeleton.

20

Therefore, the presence of PT$_0$ witnesses the ability of cobalt to infiltrate the grain boundaries in a more or less massive way. The similarity of the behavior of PT$_0$ with the PT$_2$-PT$_3$ pair suggests a different interpretation of these two peaks with respect to former literature. The presence of PT$_2$-PT$_3$ has been associated with the movement of dislocations in the TiCN grains controlled by a mechanism equivalent to the Bordoni peak for the ceramic phase [6, 18]. This interpretation was justified by the observation of dislocation multiplication when cermets are deformed in the temperature range where PT$_2$-PT$_3$ are observed at 1 Hz, and by the dependence of the peak amplitude on the binder content. This last effect was supposed to be induced, as the Bordoni peak, by internal stresses [19]. In fact, such stresses increase in the ceramic phase when the binder content increases. However, as demonstrated by diffraction measurements, the residual stresses are almost completely relaxed above 1200 K [20] where PT$_2$-PT$_3$ appear. As shown in [17], PT$_2$-PT$_3$ are also quite sensitive to the Mo content in the ceramic. The sensitivity to the ceramic composition and to the cobalt content suggests that the process involves both constituents. The process must however be located in the ceramic since it is present when the cobalt is removed. The most likely hypothesis is that grain boundary are involved and that the process is related to cobalt segregation at the

grain boundaries. Therefore, both PT$_0$ and the peaks PT$_2$-PT$_3$ involve diffusion processes at the TiCN grain boundaries enhanced by the solution of Mo or W into the binder.

Finally, at very high temperature, both WC-Co and TiCN-Co show a characteristic peak. In order to observe them at reasonable temperatures, one has to work at very low frequencies. Then a peak PT$_4$ is clearly observed at 1500 K for a frequency of 1Hz (Fig. 4a). It is interesting to notice that this peak has an amplitude that fades away when the temperature is lowered. Several arguments show that this peak depends on the infiltration of the grain boundary by the cobalt binder. So, the thermodynamical equilibrium of the boundary should change with temperature. This is also the case for the WC-Co, where a relaxation peak appears at very high temperature as shown in Fig. 4b.
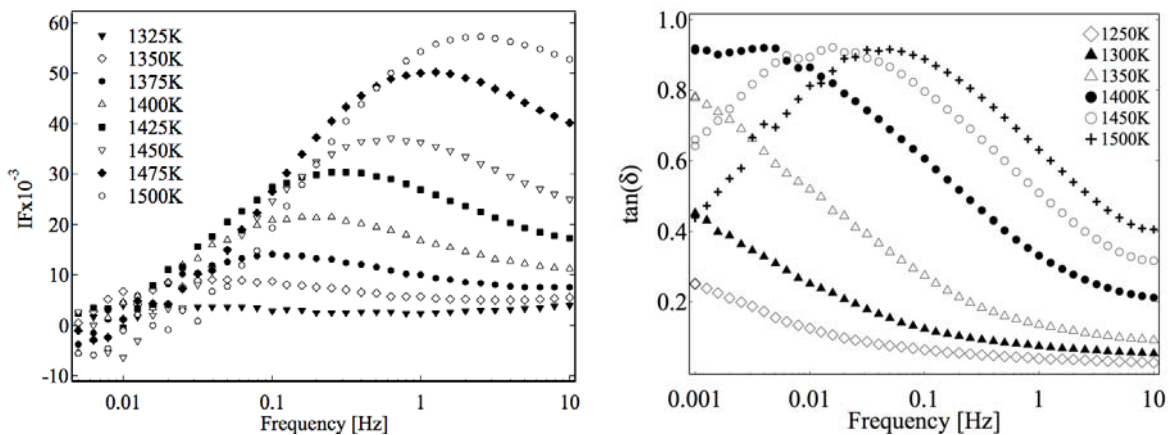
Fig. 4. a) Spectra measured as a function of frequency in TiCN5WC10Co, another peak PT$_4$ is clearly appearing between 0.1 and 1 Hz. The amplitude of this peak is increasing as a function of temperature in a reversible way. b) Spectra measured as a function of frequency in WC-10Co. A very high relaxation peak appears at high temperature and low frequency.

Conclusions

Hardmetals show a complex internal friction spectrum due to phase interaction.

The analysis of temperature scans in parallel with isothermal frequency scans demonstrates in a reliable way the presence of a multiplicity of relaxation peaks.

In WC-Co, a relaxation peak attributed to Co interaction with solute W has been identified. The abrupt change of its shape gives further evidence of a spinodal decomposition of the W-Co alloy constituting the binder. This peak is related with the toughness of the cemented carbides.

At intermediate temperature, different point defect located at the WC or TiCN grain boundaries reveal the progressive change of these grain boundaries due to binder segregation.

21

_____

At high temperature, the wetting of the binder of the grain boundaries produces a grain boundary sliding peak both in the cemented carbides and in the cermets. Extensive plastic deformation is induced by this mechanism.

References
[1] D. Mari, Cermets and Hardmetals, Encyclopedia of Materials, Elsevier Science Publisher Pergamon Press, Amsterdam, 2001, pp. 1118-1123.
[2] D. Mari, D.R. Gonseth, A New Look at Carbide Tool Life, Wear 165 (1993) 9-17.
[3] D.I. Chun, D.Y. Kim, Microstructural Evolution during the Sintering of TiC-Mo-Ni Cermets, J. Am. Ceram. Soc. 76 (1993) 2049-2052.
[4] H.-O. Andrén, U. Rolander, P. Lindahl, Phase Composition in Cemented Carbides and Cermets, Int. J. Refr. Metals Hard Mater. 12 (1993-1994) 107-113.
[5] J. Zackrisson, U. Rolander, H.-O. Andrén, Development of cermet microstructures during sintering, Metall. Mat. Trans. A 32 (2001) 85-94.
[6] D. Mari, S. Bolognini, G. Feusier, T. Viatte, W. Benoit, Experimental Strategy to Study the Mechanical Behaviour of Hardmetals for Cutting Tools, Int. J. Refr. Metals Hard Mater. 17 (1999) 209-225.
[7] D. Mari, S. Bolognini, T. Viatte, W. Benoit, Study of the mechanical properties of TiCN-WC-Co hardmetals by the interpretation of internal friction spectra, Int. J. Refr. Hard Metals 19 (2001) 257-265.
[8] R.M. Fuoss, J.G. Kirkwood, Electrical Properties of Solids. VIII. Dipole Moments in Polyvinyl Chloride-Diphenyl Systems, J. Am. Chem. Soc. 63 (1941) 385-394.
[9] M. Gardon, PhD Thesis, INSA, Lyon, 1993.
[10] R. Schaller, J.J. Ammann, C. Bonjour, Internal friction in WC-Co hard metals, Mater. Sci. Eng. A 105-6 (1988) 313-321.
[11] R. Schaller, D. Mari, M. Maamouri, J.J. Ammann, Mechanical Behaviour of WC-11wt%Co Studied by Bending Tests, Internal Friction and Electron Microscopy, J. Hard Mater. 3 (1992) 351-362.
[12] J.-J. Ammann, R. Schaller, Influence of a Changing Microstructure on High Temperature Relaxation Peaks, an Example: WC-11wt.%Co, J. Alloys Compounds 211/212 (1994) 397-401.
[13] A. Fernández Guillermet, Thermodynamic Properties of the Co-W-C System, Metall. Trans. A 20A (1989) 935-956.
[14] G. Östberg, B. Jansson, H.-O. Andrén, On spinodal decomposition in the Co-W system, Scripta Mater. 54 (2006) 595-598.
[15] D. Mari, Understanding the mechanical properties of hardmetals through mechanical spectroscopy, Mater. Sci. Eng. A 521-522 (2009) 322-328.
[16] A. Davydov, U. Kattner, Revised thermodynamic description for the Co-Mo system, Journal of Phase Equilibria and Diffusion 24 (2003) 209-211.
[17] S. Bolognini, G. Feusier, D. Mari, T. Viatte, W. Benoit, High Temperature Mechanical Behaviour of Ti(C,N)-Mo-Co Cermets, Int. J. Refr. Metals Hard Mater. 16 (1998) 257-268.
[18] S. Bolognini, D. Mari, T. Viatte, W. Benoit, High Temperature Mechanical Behaviour of Ti(C,N)-WC-Co Hardmetals, Advances in Mechanical Behaviour, Plasticity and Damage, Elsevier Science, Oxford, 2000, pp. 777-782.
[19] G. Fantozzi, C. Esnouf, W. Benoit, I. Ritchie, Internal Friction and Microdeformation due to the Intrinsic Properties of Dislocations : The Bordoni Relaxation, Progr. Mater. Sci. 27 (1982) 311-451.
[20] K. Buss, D. Mari, High temperature deformation mechanisms in cemented carbides and cermets studied by mechanical spectroscopy, Mater. Sci. Eng. A 370 (2004) 163-167.

_____

Failure of Varistor Ceramics

R. Danzer[1,2] and P. Supancic[1,2]

[1] Montanuniversität Leoben, Institut für Struktur- und Funktionskeramik, Peter Tunner Straße 5, 8700 Leoben, Austria, robert.danzer@unileoben.ac.at
[2] Materials Center Leoben Forschung GmbH, Roseggerstraße 12, 8700 Leoben, Austria

Abstract

Ceramic varistors are electronic components which have a sharp change (over several orders of magnitude) of their electrical resistance at a well-defined voltage (switching voltage). Starting at low voltages, the resistance is large. But by exceeding the switching voltage the resistance drops dramatically and the component acts as a good conductor. Mounted parallel to a consumer, they are used as protection devices against over voltage loading. In the technical routine yearly billions of varistors are used to protect power lines, transformation stations, electronic devices, micro-electronic systems or even LEDs.
In service large temperature differences may come into existence, which cause severe mechanical stresses, that even may destroy the components. The basic principles of the varistor behaviour are explained and examples of mechanical failure are discussed.

23

Keywords

Zinc oxide, varistor ceramic component, non-linear electric behaviour, Joule heating, component's failure

Introduction

Commercial varistors are – in general - made of ZnO-ceramics. The ZnO single crystals are hexagonal, polar and piezo-electric [1]. Pure ZnO crystals are isolators. In varistors the material is doped (in general with Al-donators) to become a good semi-conductor. Varistors have a polycrystalline microstructure, see Fig. 1.a, which is essential for the occurrence of the so-called varistor effect. During the sintering of the ceramics acceptor-like defects are deposited in the grain boundaries, which are partly occupied and therefore negatively charged. They cause positive space charge layers (depletion zones) at both sides of the boundaries, so-called double Schottky barriers. The potential barriers at the grain boundaries act as cage for the conducting electrons within the individual ZnO grains. In this stage the varistor ceramic is an isolator. An overview on varistors is given in [2, 3].
If an electrical potential is applied on the component the electron energy is shifted and the barrier height is lowered. If the potential is high enough some electrons overcome the barrier (the grain boundary). At the other side of the boundary, the electron falls down of the barrier, becomes accelerated and hits to other particles. If the electron energy is higher as the band gap (~ 3.2 eV) electron-hole pairs can be

generated. The positive charged holes get attracted to the boundary and can recombine with the negative charged acceptors. This causes a very quick destruction of the barrier (within some nanoseconds) [4, 5]. In this stage the grain boundary and the ceramic become conductive. The voltage, where the change of resistivity occurs, is called switching voltage. Fig. 1.b shows typical current voltage characteristics of a modern ZnO-varistor material. The increase of conductivity is more than ten orders of magnitude. Materials with such high non-linearity are exceptional. Note that this behaviour is a great challenge for the mathematical modelling of the parts.
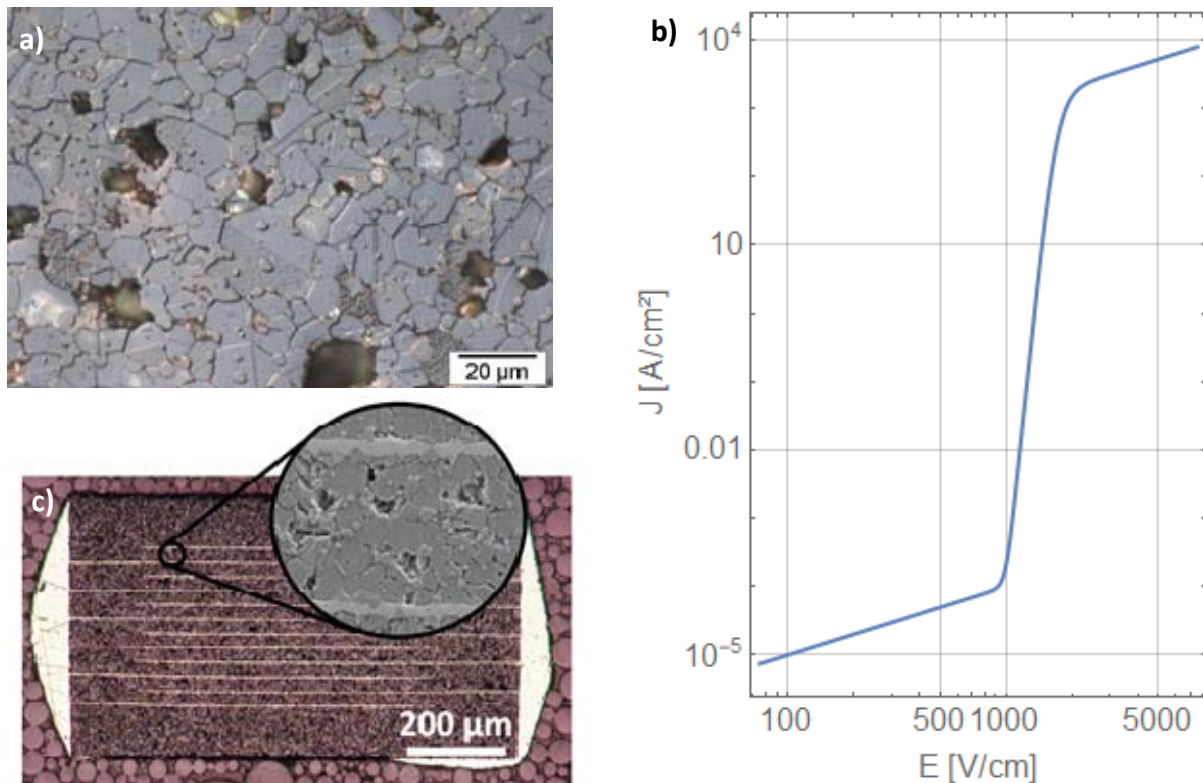
Fig. 1. a) Microstructure of a commercial ceramic varistor. b) Current voltage characteristics of a typical ZnO varistor component. Note that the change of the electrical resistance covers about 10 orders of magnitude. c) Cut through a multilayer varistor having a switching voltage of several volts.

The switching voltage of a single grain boundary is about 3 V. It mainly depends on the size of the band gap but also – to some extend - on the amount of charges in the boundary. Therefore the orientation of grains (due to their polarity) and mechanical stresses (due to the piezoelectric effect) have some influence on the switching voltage [6]. If a varistor component needs a switching voltage of e.g. 300 V, about 100 grains have to be connected in series. If the mean grain size of the material is e.g. 20 µm, the thickness of the correspondent varistor component would be 100 x 20 µm = 2 mm. Components for very high switching voltages are relatively large (or several smaller components are connected in series) and components for small switching voltage are very small. For a switching voltage of several volts the

24

"active" part of the component is only several grain diameters thick and the linear dimension of the components (made in a multilayer design, see Fig.1.c) is several 100 µm.

Varistors are used as protection devices against over voltages. They are mounted parallel to a component to be protected. In the normal state, the resistance of the varistor exceeds that of the component by many orders of magnitude, so that most of the current flows through the component. In the case of an over voltage event (which, per definition, is higher as the switching voltage) the resistance of the varistor dramatically decreases and becomes very small compared to the resistance of the device. Then almost the total current flows through the varistor.

Case studies of varistor failure

Case 1: Failures of a high power varistor during electric impulse testing, fracture origins are near the cylindrical surface of the varistor

This case is also described in [7]. It deals with high power varistors which, for example, are used to protect electric power lines or transformation stations. The investigated components have a cylindrical shape (Fig. 2.a). Typical dimensions are: diameters in the range from 2 to 12 cm, heights between 2 and 5 cm and switching voltages in the range of several kV.
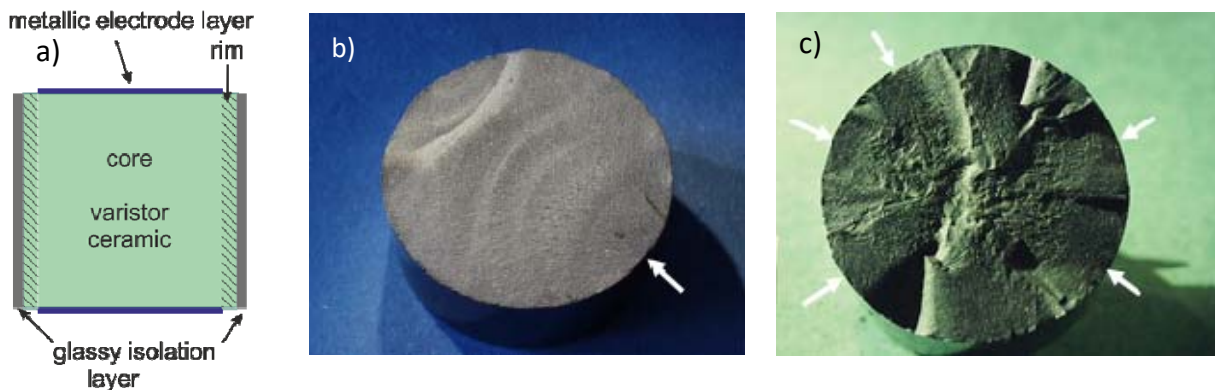
Fig. 2. a) Schematic sketch of a varistor component.
b) Fracture surface with one fracture origin in the ceramic.
c) Fracture surface with many fracture origins in the glass isolation. (Taken with friendly permission from [7]).

The components were end tested by an electric impulse, which simulates an overvoltage event (4 µs increasing and 10 µs decreasing voltage). Some of the components fractured (Fig. 2.a and 2.b) during the test. The cylindrical components have glass isolation at the cylindrical surface and a metallization at the circular top and bottom planes, which act as electric contacts (electrodes). To avoid spark overs the metallization does not cover the planes totally and there is some free space at the edges. During the electric pulse current flows between the electrodes. Note that there is a tubular part of the varistor (the rim), where no (or very little) current flows. So the inner part of the cylinder is Joule heated (the temperature can reach up to 150 °C)

but the outer part is not. The heated part expands. This causes significant tensile stresses in the rim and small compressive stresses in the inner part of the varistor. Estimations of the stresses give between 50 and 100 MPa in the ceramic rim and about half of this (due to the lower Young`s modulus) in the glass.

Strength tests on several types of commercial varistors showed (depending on the producer) a 4-point bending characteristic strength between 70 MPa and 100 MPa and a Weibull modulus between 14 and 25 [7], what fits to the estimated loadings and the observed fractures. In the bending specimens many fracture origins were remnants of hollow or not destroyed agglomerates which become defects after sintering. Similar defects can be observed in varistors with fracture surfaces according to Fig. 2.b. Examples of agglomerates and fracture origins are shown in Fig. 3 [8]. Hollow and strong agglomerates could be reduced by an optimization of the spray drying process. This also caused an increase of the strength of the varistor material and a clear reduction of rejects.

Failures as shown in Fig. 2.c started at the surface of the glass isolation. As discussed above there also exists significant tensile stress. Obviously many small defects of similar size exist on the glass surface, which probably come to existence during the surface finish. Improvements are possible by selecting a glass with a lower modulus (causing fewer tensile stresses) and a more gentle finishing and handling procedure of the glass surface (causing less and smaller surface defects).

26
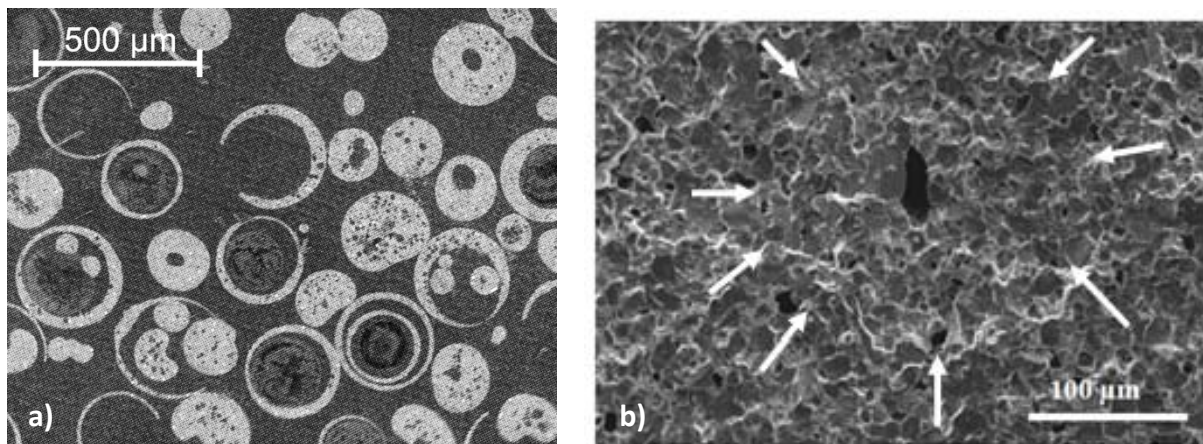
Fig. 3. (a) Hollow agglomerates made by spray drying and
(b) hollow agglomerates being fracture origins in bending specimens.

Case 2: Failures of a high power varistor during electric impulse testing, fracture origins are in the interior of the varistor

In the analysis of case 1 a quasi-static situation is analysed and inertia stresses are neglected. Large tensile stresses only occur in surface near regions of the varistor and the interior is under compression. Therefore fracture origins should always be at the surface or at surface near regions. But in some experiments having very short and strong pulses fracture from the interior has also been observed. In an excellent paper of Vojta and Clarke [9] (and later of Lengauer et al. [10]) this situation is analysed. The heating of the varistors occurs so quickly that the extension of the material is

hindered by inertia forces. Elastic waves cone to existence, which are reflected at the surfaces and interfere with each other. So, high tensile stresses may occur in the interior of the components. This case is relevant for pulses lasting of a few ten microseconds or less. Of course the interference of the waves depends on the geometry of the components: The highest tensile stress component is in the axial direction, if the aspect ratio (height/diameter) of the cylinder is larger than one and in the radial direction, if it is smaller than one [10]. In consequence the fracture plane is normal to the axial direction in the first and in axial direction in the second case. Examples of such failures are shown in Fig. 4.

This type of failure can be reduced by a careful design of the varistor geometry (in the cases analysed in [10], a height/diameter of about one is optimal) and by increasing the strength of the varistor ceramic.

27
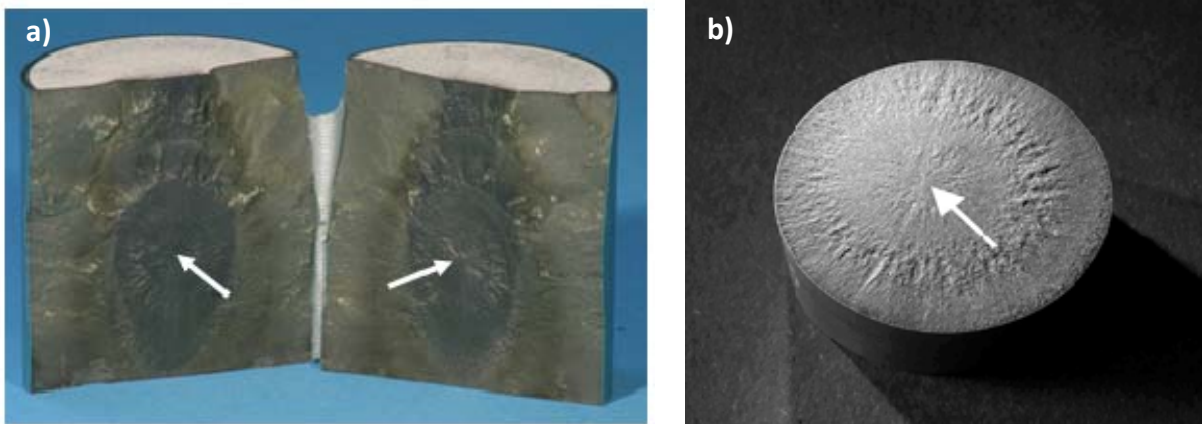
Fig. 4. Varistor components failed in a pulse test having the fracture origin in the interior. The fracture plane is (a) in axial and (b) perpendicular to the axial direction of the cylindrical component.

Case 3: Local melting of varistor components

Sometimes local overheating of varistor components arises. It may cause a local melting of the ceramic, what causes a tube like "worm hole" and as a consequence a short cut failure of the component. Occasionally the component than splits into two parts (along the axial direction) or it may even burst in many parts.

The reasons for this behaviour are related to macro- and microscopical inhomogeneities. Varistors are also NTC materials, i.e. their electric resistance strongly decreases with increasing temperature. It is also sensitively dependent on the chemical composition. Therefore local variations of the chemical composition cause a local variation of the resistance. As also shown by numerical simulations more electric current flows over the path having the lower resistance, which than produces more Joule heat as the other parts. Due to the NTC-effect this process is self-accelerating.

In the simulations the generalised Laplace equation and the heat transfer equation (including heat sources) have to be solved [11]. These non-linear differential equations contain the electrical resistance, i.e. they are coupled and have to be

solved simultaneously. If a voltage is applied on the varistor it causes an electric current, which varies with the local chemical composition. The current causes some Joule heating, which lowers the local resistance (varistors show an NTC behaviour) and heat flows into the vicinity. This again changes the local resistances. This complex control circuit has to be solved iteratively. Note that caused by the heat production thermomechanical stresses in the component will come to existence, which may strongly deviate from stress fields expected for idealised models.
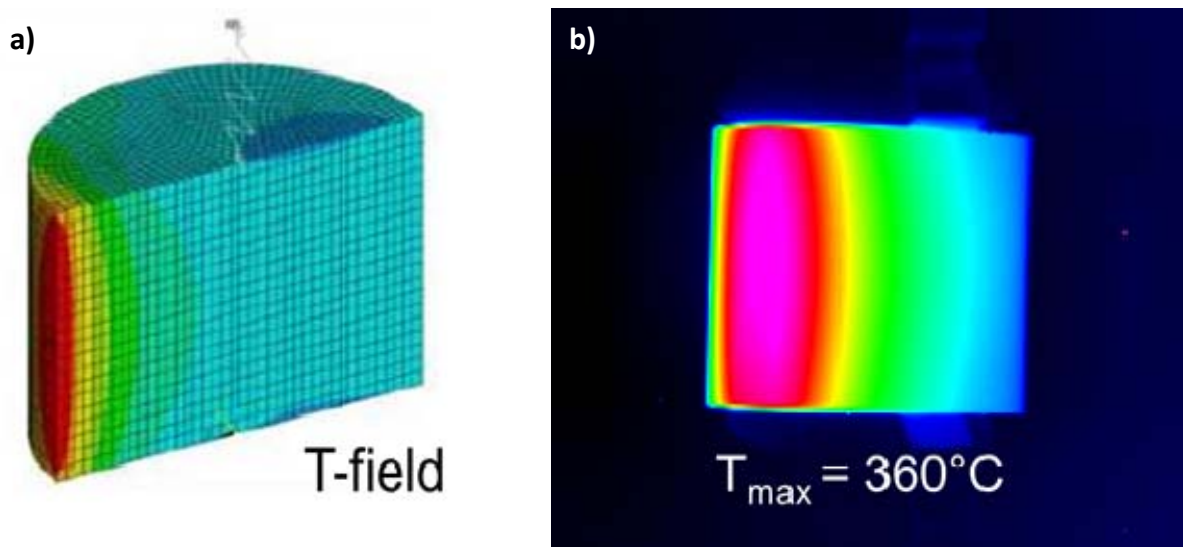
Fig. 5. Temperature distribution in the axial mid plane of a varistor with local inhomogeneities in service: (a) simulation and (b) measurement.

Fig. 5 shows FE-results of such simulations. Shown is the temperature distribution through a varistor cross section. It has been assumed that the resistance is locally distributed and has a maximum somewhere at the surface. Also shown is a measurement of the temperature at the surface of a varistor displaying similar behaviour. A qualitative correspondence can be recognised. Fig. 6 shows a varistor in the moment of an electric breakthrough.

Improvements can be reached by producing parts with an as homogeneous as possible micro-structure. This relates to the distribution of chemical elements but also on the grain size distribution. If the bursting of components should be avoided and a splitting into two parts is preferred (e.g. for safety reasons) slight property gradients may be beneficial, where areas with a lower resistance are at or near the surface of the component.

Final remarks

This article summarizes typical failures in high power varistors. It is interesting to realise that the reasons for mechanical and electrical failure are equal. Therefore a high strength of a varistor material is also beneficial for its electrical strength and reliability. The homogeneity of the micro-structure is decisive for a high share of active volume. In the case of low energy varistors having switching voltages of a few

_____

volts only a few grain boundaries exist in the active layer between the electrodes. Then the aspect of a highly homogeneous microstructure becomes even more relevant. These aspects will be treated in the paper of B. Kaufmann [12].
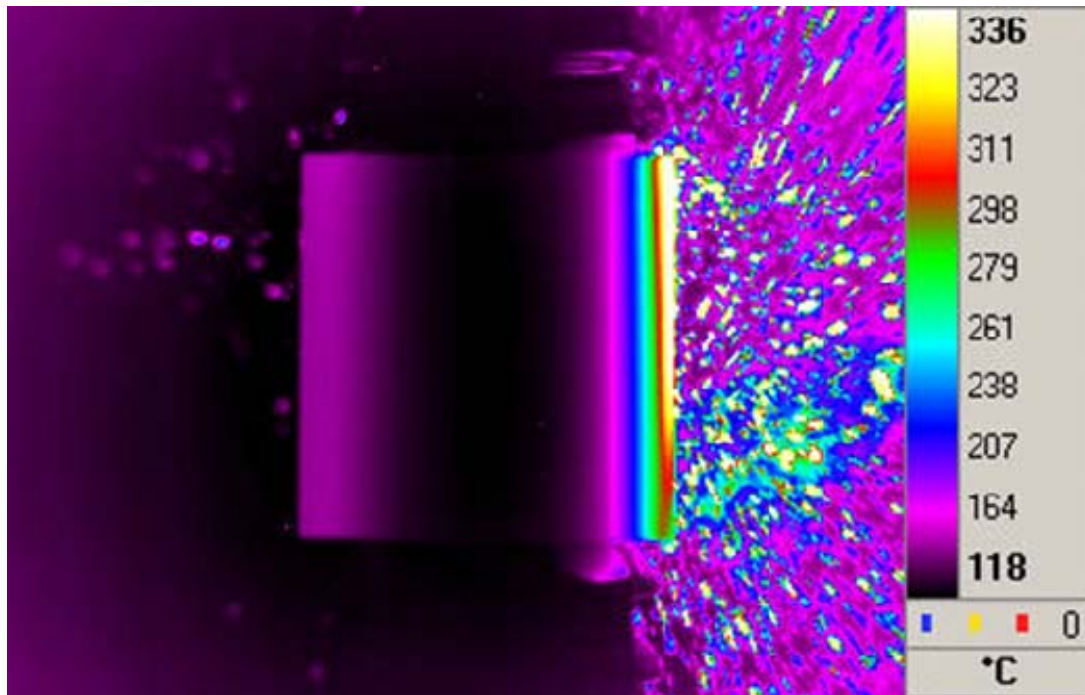
Fig. 6. Electric breakthrough of a varistor in an electric pulse test.

29

Acknowledgements

References

[1] H. Morkoç, Ü. Özgür, Zinc Oxide: Fundmentals, Materials and Device Technology, Wiley-VCH, Weinheim, Cambridge.2007.

[2] A.J. Moulson, J.M. Herbert, Electroceramics, Chapman & Hall, London, Weinheim, New York, Tokyo, Melbourne, Madras, 1997.

[3] D.R. Clarke, Varistor Ceramics, Journal of the American Ceramic Society 82(3) (1999) 485-502.

[4] F. Greuter, G. Blatter, Electrical breakdown at semiconductor grain boundaries, Physical Review B 34(12) (1986) 8555-8572.

[5] G.E. Pike, Semiconductor grain-boundary admittance: Theory, Physical Review B 30(2) (1984) 795-802.

[6] N. Raidl, P. Supancic, R. Danzer, M. Hofstätter, Piezotronically Modified Double Schottky Barriers in ZnO Varistors, Advanced Materials 27 (2015) 2031-2035.

_____

_____

[7] Z. Wang, P. Supancic, F. Aldrian, A. Schriener, R. Danzer, Strength and Fractography of High Power Varistors, Key Engineering Materials 290 (2005) 358-365.

[8] M. Hangl, Charakterisierung elektrokeramischer Grünkörper - Homogenität und mechanische Eigenschaften, Institut für Struktur- und Funktionskeramik, Montanuniversität Leoben, Leoben, 1999, p. 169.

[9] A. Vojta, D.R. Clarke, Electrical-Impulse-Induced Fracture of Zinc Oxide Varistor Ceramics, Journal of the American Ceramic Society 80(8) (1997) 2086-2092.

[10] M. Lengauer, D. Rubeša, R. Danzer, Finite Element Modelling of the Electrical Impulse Induced Fracture of a High Voltage Varistor, Journal of the European Ceramic Society 20(8) (2000) 1017-1021.

[11] P. Supancic, Mechanical Stability of $BaTiO_3$-based PTC Thermistor Components: Experimental Investigations and Theoretical Modelling, Journal of the European Ceramic Society 20(12) (2000) 2009-2024.

[12] B. Kaufmann, M. Hofstätter, N. Raidl, P. Supancic, Current dominating paths through ZnO varistor ceramics, abstract book CIE 2018.

_____

Defect properties of iron-doped hexagonal barium titanate ceramics

H. T. Langhammer[1], R. Böttcher[2], T. Walther[3], C. Eisenschmidt[4], S. Kücker[5], S. G. Ebbinghaus[6]

[1] Institut für Chemie, Martin-Luther-Universität Halle-Wittenberg, Germany, hans.langhammer@physik.uni-halle.de

[2] Fakultät für Physik und Geowissenschaften, Universität Leipzig, Germany, boettch@physik.uni-leipzig.de

[3] Institut für Chemie, Martin-Luther-Universität Halle-Wittenberg, Germany, till.walther@chemie.uni-halle.de

[4] Institut für Physik, Martin-Luther-Universität Halle-Wittenberg, Germany, christian.eisenschmidt@physik.uni-halle.de

[5] Institut für Chemie, Martin-Luther-Universität Halle-Wittenberg, Germany, stephan.kuecker@chemie.uni-halle.de

[6] Institut für Chemie, Martin-Luther-Universität Halle-Wittenberg, Germany, stephan.ebbinghaus@chemie.uni-halle.de

Abstract

X-ray diffraction (XRD) patterns, electron paramagnetic resonance (EPR, 9 and 34 GHz) and the magnetic moment in dependence on temperature and magnetic field of $BaTiO_3$ + 0.04 BaO + $x/2$ Fe_2O_3 (0.005 ≤ x ≤ 0.05) ceramics and $BaTi_{0.98}Fe_{0.02}O_3$ single crystals were studied to investigate the incorporation of Fe ions into the hexagonal $6H\text{-}BaTiO_3$ lattice and their defect properties. Angle-dependent single crystal EPR investigations and simulations of the ceramic powder EPR spectra revealed three different spectra which can be unambiguously attributed to Fe^{3+} ions incorporated at crystallographically different Ti sites. Two spectra explained by an axial-symmetric spin-Hamiltonian belong to isolated Fe^{3+} ions incorporated at Ti(1) sites (exclusively corner-sharing oxygen octahedra) and Ti(2) sites (face-sharing oxygen octahedra). The third one is caused by an associate of Fe^{3+} with a next neighbor oxygen vacancy. A corresponding model for the location of the associate is proposed. The macroscopic molar magnetic susceptibility (χ_{mol}) data of the samples confirm the existence of isolated Fe^{3+} ions. Whereas the temperature dependence of $\chi_{mol}(T)$ (5 – 300K) of the samples with x ≤ 0.01 can be explained exclusively by isolated Fe^{3+} ions, the samples with higher Fe doping content (x ≥ 0.02) exhibit deviations from that $\chi_{mol}(T)$ curve which become more pronounced with increasing Fe concentration. The deviations can be explained by direct exchange antiferromagnetic coupling between neighboring Fe^{3+} ions or by superexchange between Fe^{3+} ions mediated by an oxygen ion between both iron ions. The magnetic field dependence of $\chi_{mol}(T)$ revealed a further comparatively weak source of magnetic coupling between Fe ions which is of ferromagnetic nature.

Keywords

barium titanate, Fe doped, hexagonal phase, EPR, magnetic susceptibility

Introduction

Barium titanate (BaTiO$_3$), one of the most well-known ferroelectrics, is still in the focus of the solid-state research for example in the context of multiferroic materials and the investigation of the new class of dilute magnetic oxides (DMOs). In Fe-doped BaTiO$_3$ samples (single crystals, ceramic powders and thin films) room-temperature ferromagnetism has been previously reported [1-3]. On the other hand, distinct amounts of iron stabilize the hexagonal (6H) modification of BaTiO$_3$ at room temperature [4]. Despite the fact that hexagonal BaTiO$_3$ is not ferroelectric, Fe-doped 6H-BaTiO$_3$ samples are preferred for the investigation of ferromagnetic properties due to the very high Fe-solubility, the possibility of growing single crystals and the apparent absence of any spurious metallic Fe precipitates. For understanding the ferromagnetic properties in 6H-BaTiO$_3$ the incorporation of the paramagnetic Fe ions into the lattice and their interaction with oxygen vacancies is of fundamental importance. By means of local-probe measurements, such as electron paramagnetic resonance (EPR) on single crystals, the nature of such iron centers can be comprehensively studied. But till now, only little is known to such investigations of Fe-doped 6H-BaTiO$_3$ [3-5]. Moreover, there is a lack of systematic investigations of the magnetic susceptibility in dependence on temperature and magnetic field for this material. Hence, the goal of this work is the presentation of systematic investigations of EPR and of the macroscopic magnetic properties of Fe-doped 6H-BaTiO$_3$.

Iron substitutes for titanium in the BaTiO$_3$ lattice. In the hexagonal 6H structure (Fig. 1) there are two crystallographically different Ti sites. While Ti(1) is surrounded by 6 oxygen ions forming exclusively corner-sharing octahedra, Ti(2) is located inside the face-sharing oxygen octahedra. There are also two different oxygen sites with O(1) ions in the face-sharing planes and O(2) ions in the corner-sharing sites of the oxygen octahedra.

Fig. 1. Sketch of the crystal structure of 6H-BaTiO$_3$ with both types of oxygen octahedra viewed along the a direction.
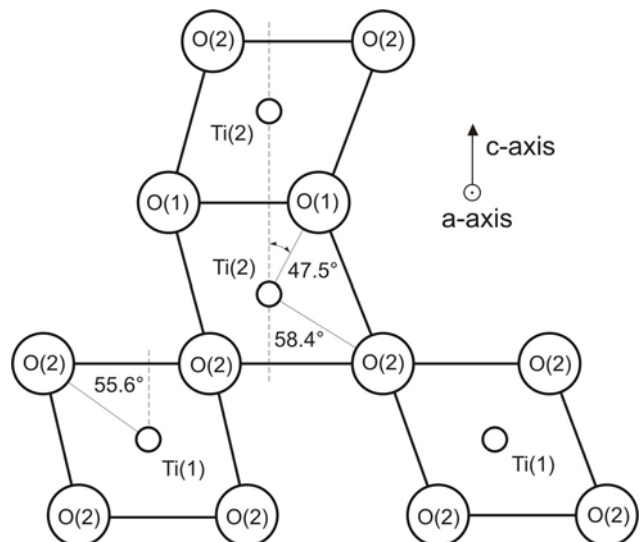
We investigated both single crystals with 2.0 mol% Fe grown by a floating-zone method and ceramics (0.5 – 5.0 mol% Fe) prepared by the conventional mixed-oxide powder technique and sintered at 1400 °C in air. EPR measurements were performed by Bruker spectrometers in X- and Q-band. Magnetic measurements were carried out using the ACMS magnetometer option of a PPMS 9 (Quantum Design).

32

Results and discussion

The EPR investigations (Fig. 2) revealed three different spectra (A, B, C) all caused by paramagnetic high-spin Fe^{3+} ions located in different defect configurations.
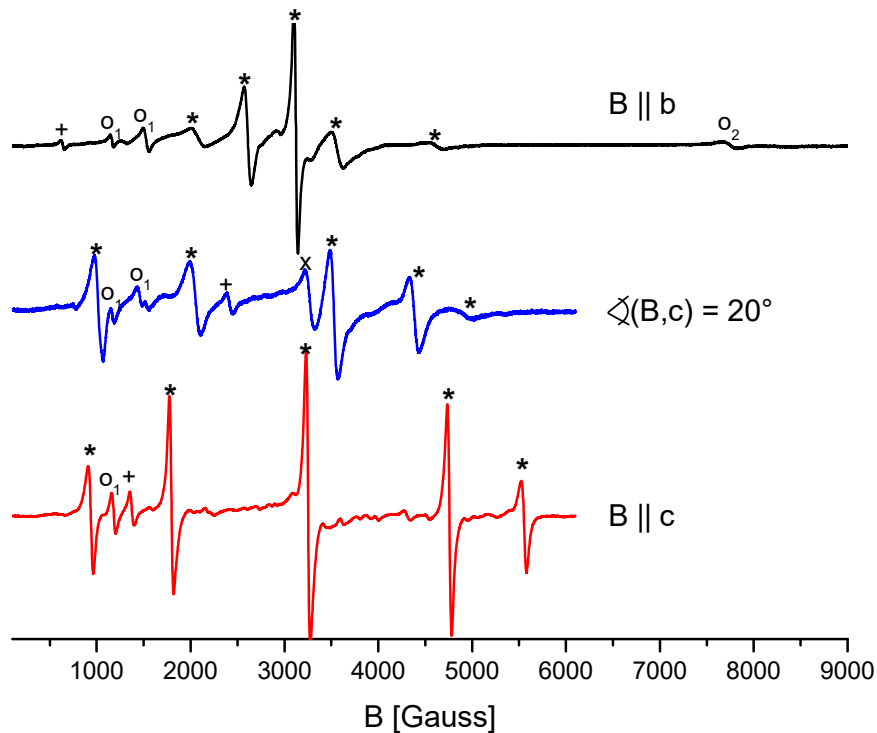
Fig. 2. EPR spectra of the 2.0 mol% Fe-doped 6H-BaTiO₃ single crystal for three orientations of the external magnetic field B. The allowed transitions of spectrum A are marked by *, the forbidden ones by +, respectively. From spectrum B only the central transition is clearly visible (marked by x). Spectrum C is marked by symbol o. o₁ identifies the transition of the doublet $m_s = \pm 1/2$ and o₂ the forbidden transition of the doublet $m_s = \pm 3/2$.

By detailed investigation of the angular dependences of these spectra (not shown here), they could be assigned to different defect centers. While the axial spectra A and B are related to isolated Fe^{3+} ions in the face-sharing and exclusively corner-sharing oxygen octahedra, respectively, the orthorhombic spectrum C is caused by a Fe^{3+} - V_O associate with the oxygen vacancy as nearest neighbor of Fe^{3+}. Analyzing the fine-structure tensor of spectrum C, the position of the vacancy was determined as the O(2) site associated with Fe^{3+} ions either at Ti(1) or Ti(2) site. The relative concentrations of these three defects amounts to $c_A : c_B : c_C = 10 : 12 : 1$.

Temperature(T)-dependent measurements of the magnetic susceptibility showed that the samples with Fe concentrations ≤ 1.0 mol% can be described exclusively with isolated Fe^{3+} ions whereas the samples with [Fe] ≥ 2.0 mol% exhibit a superposition of isolated paramagnetic (PM) Fe^{3+} ions and Fe^{3+} dimers with antiferromagnetic (AFM) exchange interaction either between two adjacent $Fe^{3+}_{Ti(2)}$ ions (direct exchange) or between $Fe^{3+}_{Ti(1)}$ and $Fe^{3+}_{Ti(2)}$ ions mediated by an oxygen ion in between

33

_____

(superexchange). The AFM interaction lowers the magnetic susceptibility shown as the effective Bohr magneton number n_{eff} (Fig. 3). Fitting of the magnetic susceptibility of the 5.0 mol% Fe-doped sample by calculated PM and AFM susceptibilities (program CONDON [6]) yields a ratio of 70% PM isolated Fe^{3+} ions to 30 % AFM Fe^{3+} dimers with an exchange parameter J = 20 cm^{-1}.
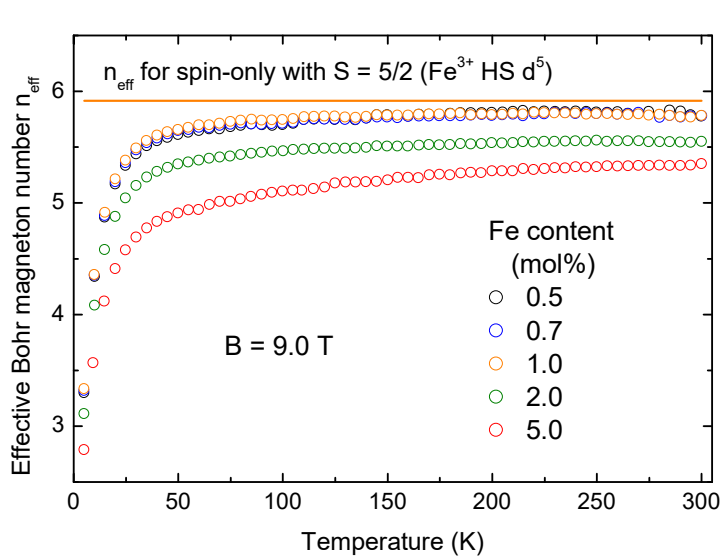
Fig. 3. Temperature dependence of the effective Bohr magnetons of 6H Fe-doped barium titanate ceramics measured at a magnetic field of 9 T

34
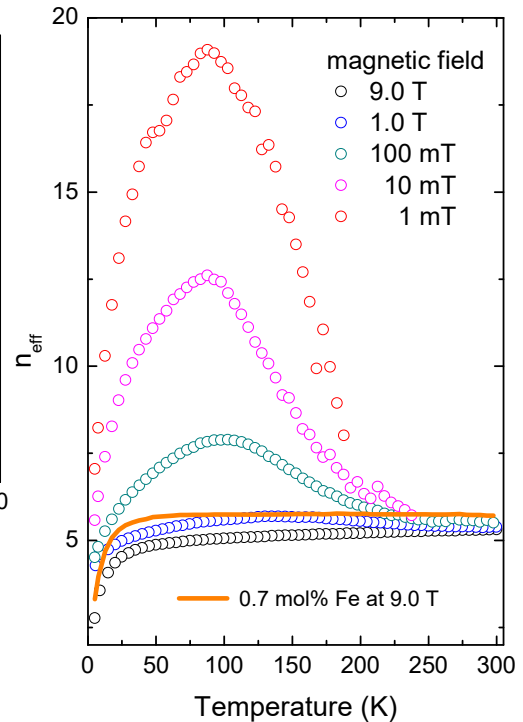
Fig. 4. Magnetic field dependence of the effective Bohr magnetons of 5.0 mol% Fe-doped barium titanate ceramics

Finally, the field dependence of the magnetic susceptibility revealed a third kind of magnetic contribution of the Fe^{3+} ions which is shown in Fig. 4 as the magnetic field dependence of the $n_{eff}(T)$ curves of the 5.0 mol% Fe-doped sample. This contribution is caused by a ferromagnetic (FM) interaction between the Fe^{3+} ions appearing below about 200 K. By subtraction of the PM and AFM contributions from the total susceptibility the FM contribution could be determined as a magnetic moment of about 0.005 Bohr magnetons per Fe^{3+} ion (averaged over all Fe^{3+} ions of the sample) at a magnetic field of 10 mT.

References

[1] S. Ray et al., Phys. Rev. B 77 (2008) 104416.
[2] T. Chakraborty et al., Phys. Rev. B 83 (2011) 144407.
[3] A. Zorko et al., Sci. Rep. 5 (2015) 7703.
[4] R. Böttcher et al., J. Phys.: Condens. Matter 20 (2008) 505209.
[5] K. Ohi et al., J. Phys. Soc. Jpn. 58 (1989) 3781-7.
[6] H. Schilder, Programm CONDON, Fachhochschule Aachen, Germany, http://www.condon.fh-aachen.de, 2014 (accessed 08.07.2018)

_____

_____

High temperature piezoelectric glass-ceramics for SAW sensors

M.Gonon[1], F.Dupla[1], M. S. Renoirt[1], N. Smagin[2], M. Duquennoy[2], G. Martic[3]

[1] *University of Mons, Materials Institute, Rue de l'Epargne 56, 7000 Mons, Belgium,* maurice.gonon@umons.ac.be
[2] *University of Valenciennes and Hainaut-Cambrésis (UVHC), IEMN-DOAE (UMR CNRS 8520), Le Mont Houy, 59313 Valenciennes, France*
[3] *Belgian Ceramic Research Center (BCRC), Avenue du Gouverneur Emile Cornez 4, 7000 Mons, Belgium*

Abstract

The work reported in this paper demonstrates that glass-ceramics containing piezoelectric non-ferroelectric crystals can be used as substrates to design Surface Acoustic Waves (SAW) sensors for pressure and, or, environment monitoring up to temperatures reaching 800°C. The paper focuses on the control of the glass-ceramic processing, the characterization of the preferential orientation of the crystallization and the ability of the material to generate and propagate SAW.

Keywords

Piezoelectric ceramics, High temperatures, Sensors, Surface Acoustic Waves

Introduction

During the last ten years, interest in sensors and transducers based on surface acoustic waves has been growing. Basically, these devices use two sets of interdigitated electrodes on a piezoelectric substrate (Fig.1) to generate, propagate and receive an acoustic signal [1-2]. Changes in propagation conditions, by mean of a sensitive zone located between the emitter and the receiver, allows the detection and the quantification of an external solicitation (pressure, temperature, environmental composition…).
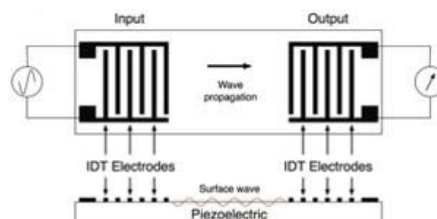
Fig. 1. Principle of SAW sensors.

Numerous applications for these devices, at room or moderate temperatures, already exist. Extension of these applications at high temperatures are inhibited by a lack of suitable piezoelectric substrates. Indeed, most of conventional piezoelectrics are ferroelectric ceramics. Their macroscopic polarization and piezoelectric properties result of an initial poling under a high strength electric field. Consequently, their use

_____

_____

in temperature is limited as depoling occurs rapidly when approaching the Curie point. Due to their intrinsic polarization and piezoelectric properties, non-ferroelectric singles crystals are stable and then potentially good candidates for high temperature applications. However, they are difficult and expensive to process. Highly textured polycrystalline materials can be seen as an alternative to single crystals. Hardly obtainable by conventional ceramic powder process, such materials can be produced by glass-ceramic route when surface crystallization mechanism is controlled. The piezoelectric non-ferroelectric phase selected in this work is the strontium fresnoite $Sr_2TiSi_2O_8$. Its tetragonal unit cell shows a dipole moment along the [00l] direction [3-4]. The glass-ceramics are produced by controlled crystallization of parent glass compositions belonging to the Sr-Ti-Si-K-Al-O system [5].

Results and discussion

Synthesis of the glass-ceramic: Parent glass plates of composition $2SrO-TiO_2-3.3SiO_2-0.2K_2O-0.1Al_2O_3$ are prepared by mixing, melting and casting reagent-grade of $SrCO_3$, TiO_2, SiO_2, Al_2O_3 and K_2CO_3. Crystallization of $Sr_2TiSi_2O_8$ fresnoite crystals is obtained by thermal treatment. An image of a cross section after 10h at 900°C, shows that crystallization starts from the surface and propagates into the bulk over time (Fig.2). After a dwell time of 15h at 900°C all crystallization fronts join. The resulting glass-ceramic is homogenous and composed of ≈70 vol% of fresnoite crystals and ≈30 vol% of residual glass $1.3SiO_2$ $0.2K_2O$ $0.1Al_2O_3$.

Characterization of fresnoite crystals orientation: X-ray diffraction (XRD) patterns collected after step-by-step grinding show a strong preferential orientation of (002) plans parallel to the specimen's surface for depth below 100 µm, and a progressive tilt of the preferential orientation at the benefit of (201) plans for depth between 100 and 300 µm. This means that, c-polar axis is first perpendicular to the surface, then rotates, and finally keeps an angle of ≈50° for depths over 300 µm (Fig.3). High temperature HT-XRD measurements performed on a glass-ceramic specimen after grinding the top 300 µm, show the high stability of the fresnoite crystals and of their (201) orientation from ambiance to 1000°C (Fig.4).

36

(a)   (b)
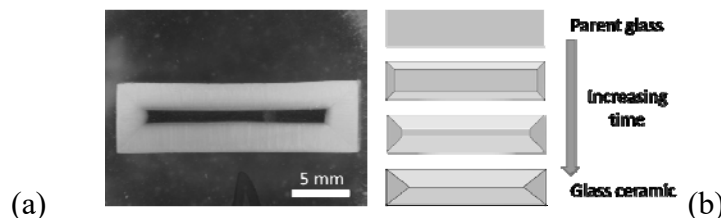
Fig. 2. (a) Image of a polished cross section of a specimen after heat treatment for 10h at 900°C; (b) schematization of the motion of the crystallization fronts over time.

*Evaluation of ability to generate and propagate surface acoustic waves:*Testing devices are composed of two sets of interdigitated platinum electrodes PVD deposited on a (201) oriented glass-ceramic substrate (Fig.5). These electrodes acts as transducers that respectively generate and receive the SAW.

_____

Evolution of signal collected by the output interdigitated electrodes (O-IDT), highlights that the amplitude progressively decreases when temperature rises from room-temperature (RT) to 600°C (Fig.6). However, the signal remains good enough (over 55 % of RT) to be used in a sensor. Surprisingly, the amplitude increases over 600°C and nearly reaches that of RT at 750°C. We may assume that the residual glass plays a key role on this evolution as 600°C is very close to its T_g.
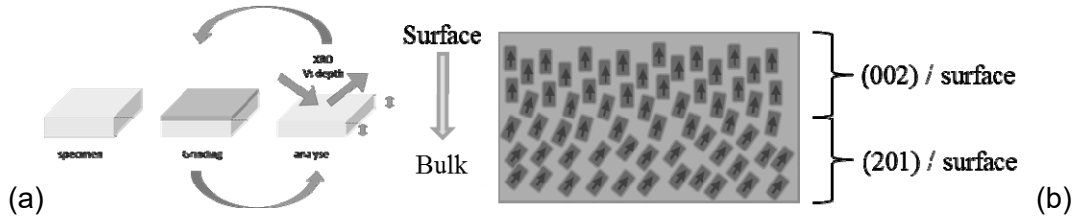
Fig. 3. (a) Analysis of preferential orientation by XRD ; (b) schematization of evolution of polar direction (arrows) over depth.
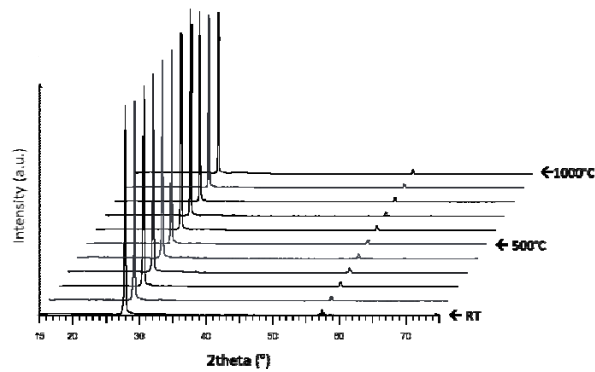
Fig. 4. HT-XRD patterns collected from ambiance up to 1000°C by step of 100°C.
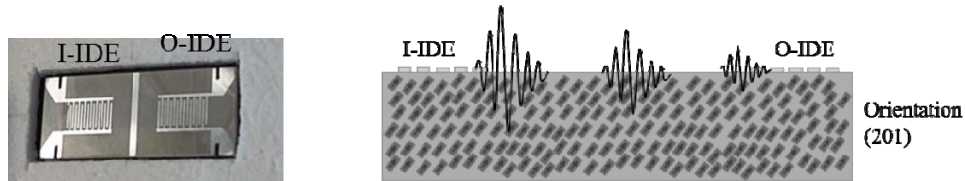
Fig. 5. (a) image of testing device ; (b) schematization of SAW generation, propagation and detection on the glass-ceramic substrate.
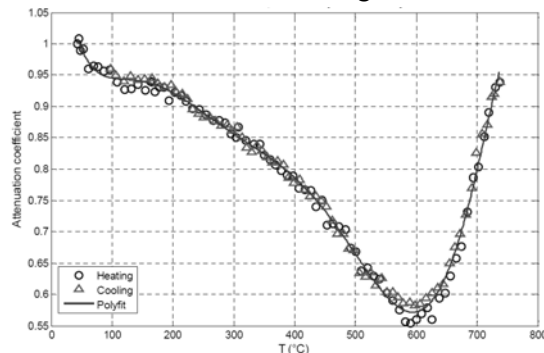
Fig. 6. Evolution of O-IDT signal amplitude (relatively to RT) vs temperature.

Fig. 7 shows the evolution with temperature of glass-ceramic's Young modulus E and damping coefficient both measured by Impulse Excitation Technique IET. It can be

37

seen that, due to the softening of the residual glass, E slowly decreases in the temperature range 600 – 800°C. This favours the SAW generation as the residual glass less constrains the piezoelectric fresnoite crystals. In this temperature range, damping is low, so that attenuation of the signal during propagation remains weak. Over 800°C, E falls dramatically while damping increases drastically. This will certainly have negative consequences on the amplitude of the received SAW signal. Further measurements at higher temperatures will be soon performed.
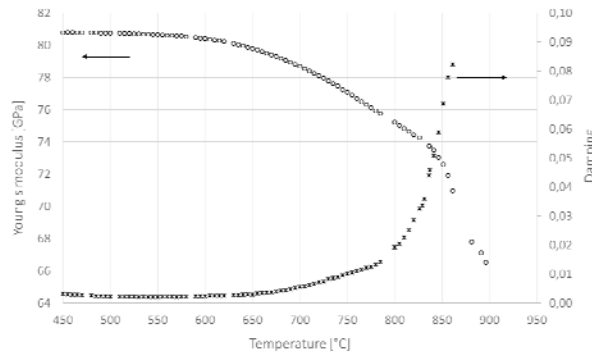
Fig. 7. Evolution of glass-ceramic's Young modulus E and damping coefficient with temperature.

Conclusions

Glass-ceramics containing 70 vol% of preferentially oriented piezoelectric non-ferroelectric Sr-fresnoite crystals have been synthesized and evaluated as substrates for generating and propagating surface acoustic waves at high temperatures. It is concluded that such materials can be used to design SAW sensors able to work up to temperatures reaching 800°C.

38

Acknowledgements

References

[1] Yang Li∗, Taotao Wu, Mujie Yang, "Humidity sensors based on the composite of multi-walled carbonnanotubes and crosslinked polyelectrolyte with good sensitivity andcapability of detecting low humidity, Sensors and Actuators B 203 (2014) 63–70
[2] D. Fall, M. Duquennoy, M. Ouaftouh, N. Smagin, B. Piwakowski, and F. Jenot, Sens. Actuators Phys. (n.d.).
[3] A. Halliyal, A.S. Bhalla, L.E. Cross, R.E. Newnham, "Dielectric, piezoelectric and pyroelectric properties of $Sr_2TiSi_2O_8$ polar glass-ceramic: A new polar material", Journal of Materials Science 20 (1985) 3745-3749.
[4] T. Höche, W. Neumann, S. Esmaeilzadeh, R. Uecker, M. Lentzen, C. Rüssel, "The Crystal Structure of $Sr_2TiSi_2O_8$", Journal of Solid State Chemistry 166 (2002) 15 - 23.
[5] N. Maury, F. Cambier, M. Gonon, "Bulk crystallisation of (00l) oriented fresnoite $Sr_2TiSi_2O_8$ in glass-ceramics of the Sr–Ti–Si–K–B–O system", Journal of Non-Crystalline Solids 357 (2011) 1079-1084.

_____

Synthesizing Barium Titanate Macrofibers Comprising of Electrospun Nanofibers

T. Sebastian*, A.Michalek$^{\$}$, T. Lusiola*, M. Bredol$^{\$}$ and F. Clemens*

*Empa – Swiss Federal Laboratories for Materials Science and Technology, Laboratory for High Performance Ceramics, Überlandstrasse 129, CH-8600 Dübendorf, Switzerland, frank.clemens@empa.ch
$^{\$}$Fachhochschule Münster, Fachbereich Chemieingenieurwesen, Stegerwaldstraße 39, 48565 Steinfurt, Germany

Abstract

The motivation of this work was to investigate the influence of $BaTiO_3$ (BT) nanofibers on the properties of $BaTiO_3$ macrofiber structure. $BaTiO_3$ nanofibers were synthesized using electrospinning process. The calcined nanofibers were chopped and mixed with $BaTiO_3$ powder to produce macrofibers. The $BaTiO_3$ macrofibers were fabricated using thermoplastic processing and was investigated by varying the calcination temperature of the nanofibers. It is realized that increase in calcination temperature of the nanofibers enhances the final electromechanical properties of the sintered macrofibers.

Keywords

Electrospinning, piezoelectric, thermoplastic processing, $BaTiO_3$

Introduction

Several strategies have been reported to improve the piezoelectric properties of a material. One of the most common approaches is enhancing the extrinsic properties by external doping and tailoring the properties by adjusting the dopant concentration. For e.g., Li^+ doped BT fabricated using solvothermal approach could be sintered at lower temperature, 1100 °C with a piezoelectric constant, d_{33} of 260 pCN^{-1}, electromechancial coupling factor, k_p of 43.7% and without any loss of Curie temperature, T_C = 130 °C.[1] Domain and grain size engineering has a noticeable influence in the final piezoelectric properties. An optimum grain size is essential to enhance the final piezoelectric properties of BT. Several literature have cited that, for BT a grain size between 1-2 µm would be the optimum value.[2-5] Too big grains experiences high fraction of non-180° domains back switching exerted by the grain boundaries thereby decreasing the properties while too small grains suppress the ferroelectricity due to the decrease in the tetragonal phase along with increased grain boundaries that can act as a dead layer.[6, 7]

In the recent past, piezoelectric fibers gained particular attention for the fabrication of composites to use in applications such as ultrasound transducers, wearable biosensors, vibration absorbers, composite force sensors etc. It is reported previously that the morphology of the constituents affect the sintering process and influences the final ferroelectric properties and the density of the material.[8] In this contribution,

_____

BT macrofibers were fabricated using thermoplastic processing.[9-11] Due to their high intrinsic properties, BT nanofibers have been employed as ferroelectric fillers in the nanocomposites to improve the final electromechanical response. An investigation was performed to study how the calcination temperature affects the final fiber properties.

Experimental

A low shear mixing process developed at Empa was used for the development of feedstock for the thermoplastic extrusion of $BaTiO_3$ macrofiber.[10, 11] The feedstock was formulated with BT powder (Ticon F, Ferro Electronic Materials, Niagara Falls, NY, USA) and *in-house* prepared electrospun BT nanofibers along with thermoplastic binder, ethylene-vinyl acetate copolymer resin (Elvax® 410, DuPont, Switzerland), surfactant - stearic acid (Fluka, Sigma-Aldrich, Switzerland), paraffin wax (Sigma-Aldrich, Switzerland) and toluene as solvent. The BT electrospun nanofibers were synthesised by sol-gel method by mixing barium acetate and titanium (IV)-isopropoxide. After electrospinning with NEU-Pro electrospinning machine and a drum collector, calcination of the nanofibers were made at four different temperatures (1000 °C, 1100 °C, 1200 °C and 1350°C) before mixing with BT powder and the results were compared with macrofiber without any nanofibers. Stoichiometric amount of materials were weighed and allowed to mix at room temperature using a magnetic stirrer for 30 minutes followed by 1 h mixing at a temperature just below the boiling point of the solvent, 110°C. The mixture was dried over 2 days at 90 °C and the feedstock was collected for extrusion. The thermoplastic extrusion of the $BaTiO_3$ feedstock was performed with a vertically mount capillary rheometer (RH7 Flowmaster, Rosand Precision Limited, UK) through a 500 μm die. The macrofibers were extruded using the rheometer at 60 °C at a shear rate of 500 s^{-1}, with an adapter to reduce the diameter of the cylinder from 24 mm to 4 mm. The macrofibers were sintered further at 1350 °C for 5 hours to densify the macrofiber and structural and electrical characterizations were carried out. The crystallographic structure of the fibers was characterized by X-ray diffraction measurements using X-ray diffractometer (X'Pert Pro MPD, PANalytical. The Netherlands) with CuK$_\alpha$ radiation ($\lambda = 0.154$ nm). Ferroelectric behaviour of the fibers were measured with a novel piece of equipment (FerroFib) developed in collaboration between Empa and aixACCT System GmbH. The large signal polarization and strain hysteresis as a function of applied electric field was recorded at 0.1 Hz.

40

Results and discussion

The effect of calcining temperature of the nanofibers on phase analysis and crystallite growth of the sintered macrofibers at 1350 °C is shown in Fig**. 1**. To get better understanding of the crystal structure of the fibers, the crystallite size was calculated using XRD data and the Scherrer equation and tetragonality (c/a) of the peaks were calculated by refinement.

$$D_p = \frac{k\lambda}{B\cos\theta}$$ Scherrer equation   (1)

where D_p is crystallite size, k is the Scherrer constant, λ is x-ray wavelength, B is full width at half maximum of XRD peak and θ is the XRD peak position.

In all the cases, the amount of calcined nanofibers added is fixed to 20 vol%. XRD shows $BaTiO_3$ peaks with tetragonal crystal structure, characterized by the 200_p peak splitting and an increase in crystallite size with temperature. However, a considerable increase in tetragonality is noticed when increasing the calcining temperature of BT nanofibers above 1000 °C, which could be due to the transition of BT nanofibers from cubic to tetragonal phase. A decrease in crystallite size and tetragonality is observed for macrofiber sintered without any nanofibers. It appears as if the presence of nanofibers with tetragonal phase favours crystallite growth and increase the tetragonality of the sintered macrofiber.
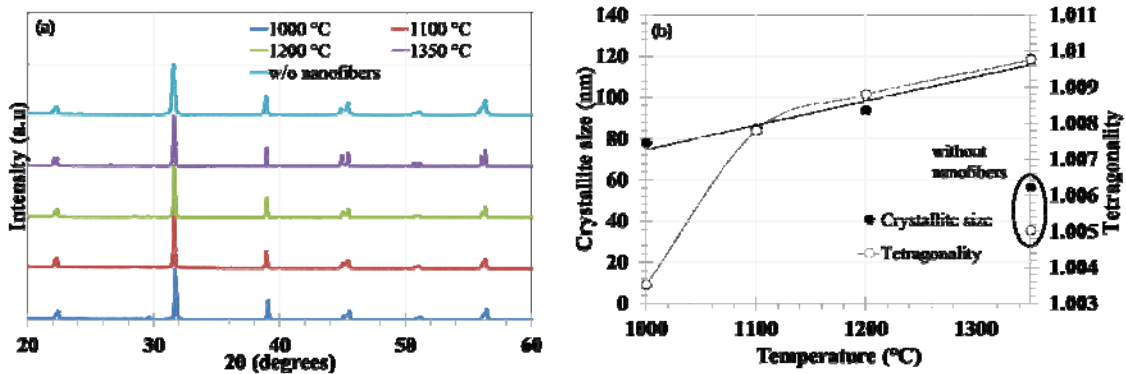
Fig. 1. (a) XRD and (b) crystallite size of sintered BT macrofibers with and without nanofibers, which were calcined at different temperatures. The marked points in the ellipse are the results of the macrofibers without nanofibers.

41

Table 3. Piezoelectric properties of sintered BT fibers with nanofibers calcined at different temperatures and without any nanofibers

Properties	Calcination temperature (°C)	1000	1100	1200	1350	Without nanofibers
Piezoelectric constant, d_{33} (pm/V)		82.5 ±4	79.8 ±2	74 ±2	67 ±11	88.8 ± 3
Relative permittivity (-)		1108 ±3	1578 ±9	1460 ±17	1780 ±13	1106 ±13
Strain (%)		0.07 ±0.02	0.08 ±0.03	0.095 ±0.02	0.103 ±0.02	0.016 ±0.004
Remanent polarisation ($\mu C/cm^2$)		5.04 ±1.2	4.54 ±1.05	6.25 ±0.78	7.6 ±1.17	1.95 ±0.3
Grain size (μm)		41 ±4	37 ±2	30 ±6	25 ±6	65 ±2

The piezoelectric properties of sintered BT fibers with nanofibers calcined at different temperatures and without any nanofibers are shown in *Table 3*. An increase in relative permittivity is observed with increase in nanofiber calcination temperature. It can be considered that high dielectric constant of BT is correlated with high tetragonality which originates from the tetragonal lattice distortion.[12] Higher

calcination temperature enhances the crystallite growth of nanofibers with tetragonal structure which thereby increases the tetragonality of the sintered macrofibers resulting in higher permittivity. Addition of nanofibers also restricts the grain growth in the macrofibers which improves the electrical properties of the macrofiber.

Conclusions

A new approach has been proposed to improve the dielectric and piezoelectric properties of BT fibers. BT nanofibers were synthesized using electrospinning technique and macrofibers were synthesized using thermoplastic processing, successfully. Piezoelectric properties of the sintered BT macrofibers sintered at 1350°C increase with the calcination temperature of nanofibers. Higher calcination temperature of the nanofibers favours crystallite growth and tetragonality of BT thereby enhancing the final properties of the sintered fibers. Nanofiber addition does not influence piezoelectric constant while an improvement is observed in the dielectric constant. A restriction in grain growth is also observed with nanofiber addition which could be the reason for higher dielectric constant.

Acknowledgements

References   42

[1] Kimura, T., et al., *Synthesis and piezoelectric properties of Li-doped BaTiO₃ by a solvothermal approach.* Journal of the European Ceramic Society, 2013. 33(5): p. 1009-1015.

[2] Huan, Y., et al., *Grain Size Effects on Piezoelectric Properties and Domain Structure of BaTiO₃ Ceramics Prepared by Two-Step Sintering.* Journal of the American Ceramic Society, 2013. 96(11): p. 3369-3371.

[3] Tan, Y., et al., *Unfolding grain size effects in barium titanate ferroelectric ceramics.* Scientific Reports, 2015. 5: p. 9953.

[4] Hirofumi, T., et al., *Lead-Free Barium Titanate Ceramics with Large Piezoelectric Constant Fabricated by Microwave Sintering.* Japanese Journal of Applied Physics, 2006. 45(1L): p. L30.

[5] Takahashi, H., *Development of lead-free BaTiO₃ ceramics possessing enhanced piezoelectric properties.* Electronics and Communications in Japan, 2012. 95(4): p. 20-26.

[6] Tan, Y., et al., *Enhancement of electric field-induced strain in BaTiO₃ ceramics through grain size optimization.* physica status solidi (a), 2014. 212(2): p. 433-438.

[7] Zhao, Z., et al., *Grain-size effects on the ferroelectric behavior of dense nanocrystalline BaTiO₃ ceramics.* Physical Review B, 2004. 70(2): p. 024107.

[8] Ge, H., et al., *Facile synthesis and high d₃₃ of single-crystalline KNbO₃ nanocubes.* Chemical Communications, 2008(41): p. 5137-5139.

[9] Heiber, J., et al., *Thermoplastic Extrusion to Highly-Loaded Thin Green Fibres Containing Pb(Zr,Ti)O₃.* Advanced Engineering Materials, 2005. 7(5): p. 404-408.

[10] Lusiola, T., et al., *Low shear compounding process for thermoplastic fabrication of ferroelectric lead-free fibres.* Journal of the European Ceramic Society, 2014. 34(10): p. 2265-2274.

[11] Sebastian, T., T. Lusiola, and F. Clemens, *Ferroelectric hybrid fibers to develop flexible sensors for shape sensing of smart textiles and soft condensed matter bodies.* Smart Materials and Structures, 2017. 26(4): p. 045003.

[12] Cochran, W., *Crystal stability and the theory of ferroelectricity.* Advances in Physics, 1960. 9(36): p. 387-423.

Influence of the Crystallization Conditions on the Microstructure of a Piezoelectric Glass-Ceramic

F.Dupla[1], M.S. Renoirt[1], M.Gonon[1]

[1] *University of Mons, Materials Institute, Rue de l'Epargne 56, 7000 Mons, Belgium*

Abstract

The work here presented aims at understanding the surface crystallization mechanism of non-ferroelectric piezoelectric $(Sr,Ba)_2TiSi_2O_8$ Fresnoite crystals in glass-ceramics belonging to the Ba-Sr-Ti-Si-K-Al-O system. It focuses on the influence of the interface conditions on the surface crystallization speed, microstructure, and preferential orientation.

Keywords

Fresnoite ; Glass-ceramic ; Surface crystallization ; Piezoelectricity ; Orientation

Introduction

Fresnoite crystals $Sr_2TiSi_2O_8$ and $Ba_2TiSi_2O_8$ belong to the tetragonal system and the P_4bm space group. These phases are pyroelectric, the unit cells present an electric dipole along the c axis thanks to the titanium-centered square pyramids (figure 1). However, fresnoite crystals do not divide into electric domains, they are non-ferroelectric. Consequently, in a polycrystalline material, fresnoite crystals must be preferentially oriented to induce a macroscopic piezoelectricity. If so, the material shows no Curie temperature and no depolarization over time.

43
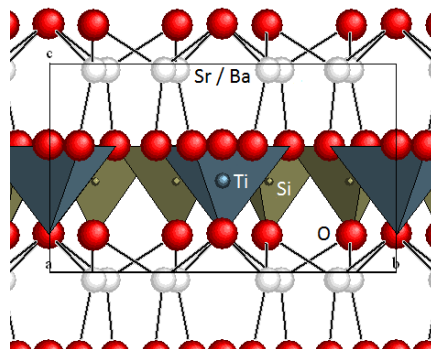
Fig. 1. Fresnoite structure

The piezoelectric properties of fresnoite-based glass-ceramics were extensively studied during the 1980's by Halliyal and al. because they show a polar orientation when surface crystallized [1]. Crystallization starts from the specimen surfaces and propagates in depth over time. Different processes can be used to induce surface crystallization such as thermal gradient or electrochemical nucleation [1,2]. In this work, the crystallization step is realized during an isothermal treatment in order to assess the possibility of obtaining a piezoelectric material without costly apparatus.

The main problems in the processing of fresnoite glass-ceramics are the control of the preferential orientation over depth when the crystallization front progresses and the competition between surface crystallization (piezoelectric) and volume crystallization (non-piezoelectric). Surface crystallization phenomenon is not well known yet, but is surely influenced by the glass composition, the surface roughness, the presence of foreign particles on the surface and by the temperature [3].

Synthesis of fresnoite glass-ceramics

Parent glass of compositions $(2-x)SrO–xBaO–TiO_2–3.3SiO_2–0.2K_2O–0.1Al_2O_3$ [x = 0; 0.5; 1] are prepared by mixing, melting and casting reagent-grade of $SrCO_3$, $BaCO_3$, TiO_2, SiO_2, Al_2O_3 and K_2CO_3. Glass plates, 6 mm thick, of different surface roughnesses: Ra = 0.02 μm (mirror polishing) and Ra = 1.5 μm (P220 grade polishing) were prepared (figure 2). They were further crystallized in Al_2O_3 or ZrO_2 powder beds (mean particle size D50 = 0.5 μm) by isothermal treatments at 850, 900 or 950°C and various holding times.

Fig. 2. Fresnoite glass (left) and glass-ceramic (right)

The obtained glass-ceramics (figure 2) are composed of approximatively 70 vol% of fresnoite crystals and 30vol% of residual glass of composition $1.3SiO_2–0.2K_2O–0.1Al_2O_3$.

Results and discussion

Crystallization of $Sr_2TiSi_2O_8$ glass-ceramics

Glass-ceramics obtained from mirror-polished parent glass plates exhibit no volume crystallization, contrary to high roughness plates (figure 3). This difference occurs whether crystallization is realized in Al_2O_3 or ZrO_2 powder beds. A low roughness certainly decreases the nucleation time before crystallization starts, preventing the apparition of volume crystallization.

For mirror-polished glass plates, the measurements of crystallized thickness for different temperatures and times show that the speed of the crystallization front is higher in Al_2O_3 beds than in ZrO_2 beds (Table 1). This means that the nucleation time is shorter in Al_2O_3.

The crystallization speed strongly increases with temperature, as the viscosity rapidly falls and then allows an easiest propagation of the crystallization front.
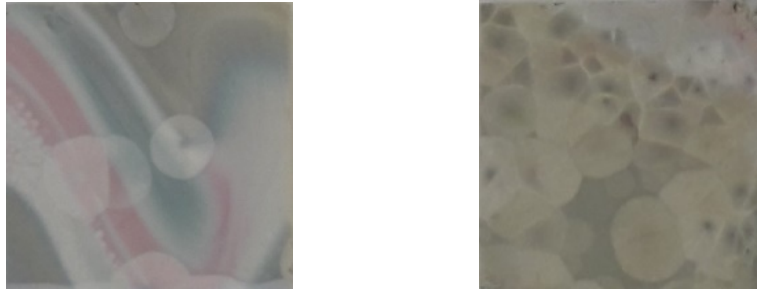
Fig. 3. Volume crystallization for Ra = 0.02 µm (left) and Ra = 1.5 µm (right) after isothermal treatment at 900°C for 20h

T(°C)	V_{crist} Al_2O_3 (mm/h)	V_{crist} ZrO_2 (mm/h)
850	0.03	0.03
900	0.21	0.13
950	1.09	0.68

Table 1. Crystallization speed in Al_2O_3 and ZrO_2 for different temperatures for mirror-polished samples

Preferential orientation of $Sr_2TiSi_2O_8$ crystals
The results presented hereunder are the same whether an Al_2O_3 or ZrO_2 bed is used. Samples are crystallized at 900°C.

45
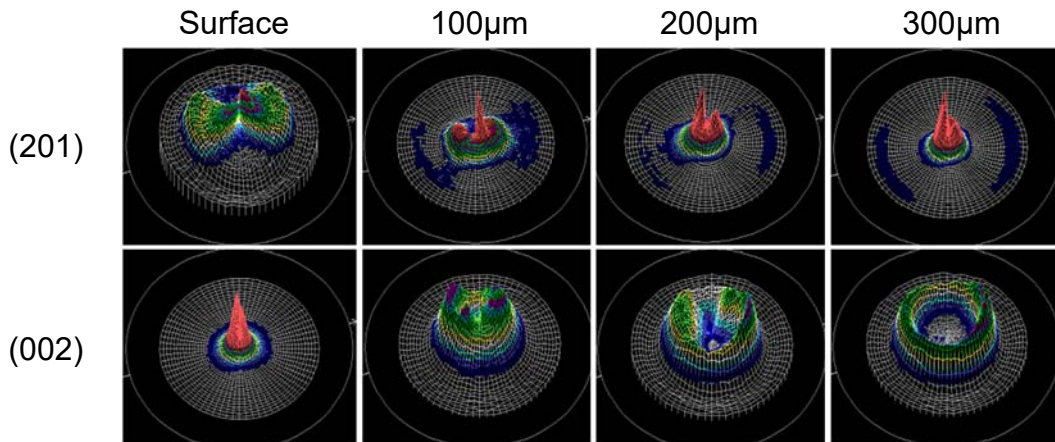
Fig. 4. Pole figures of a mirror-polished sample (ZrO_2 powder ; 900°C)

Figure 4 shows the preferential orientation usually obtained for $Sr_2TiSi_2O_8$ crystallized from mirror-polished glass plates. The orientation of the crystals planes is (002) from the surfaces down to 100 – 300 µm, and further tilts to (201). This means that the c polar axis is perpendicular to the specimen's surface first, and then rotates to an angle of ≈50° between 100 and 300 µm.
For glass plates with a surface roughness Ra = 1.5 µm, the surface crystallization orientation is not reproducible. Half of the samples show exactly the same behavior than mirror-polished samples, whereas the other half exhibits a strong (002)

orientation down to more than 1500 µm. This non-reproducibility is observed with both Al_2O_3 and ZrO_2 powder beds.

Barium substitutions

Substituting Sr by Ba in the parent glasses in order to form $Sr_{1.5}Ba_{0.5}TiSi_2O_8$ and $SrBaTiSi_2O_8$ leads to strong volume crystallization. Less than 1 mm is surface crystallized. In order to quantify the orientation over depth, orientation coefficients R for (002) or (201) planes are calculated from the peaks' intensities:

$$R(201\ or\ 002) = \frac{I(201\ or\ 002)}{I(201\ or\ 002) + I(211)}$$

With (211) being the main diffraction peak for a non-oriented sample.

The preferential orientations obtained do not significantly differ with Ba fraction, powder beds or surface roughness. For all samples (002) orientation is strong from the surface down to approximatively 600 µm where it is stopped by the volume crystallization (figure 5). Contrary to non-substituted samples, there is no (201) orientation that appears.
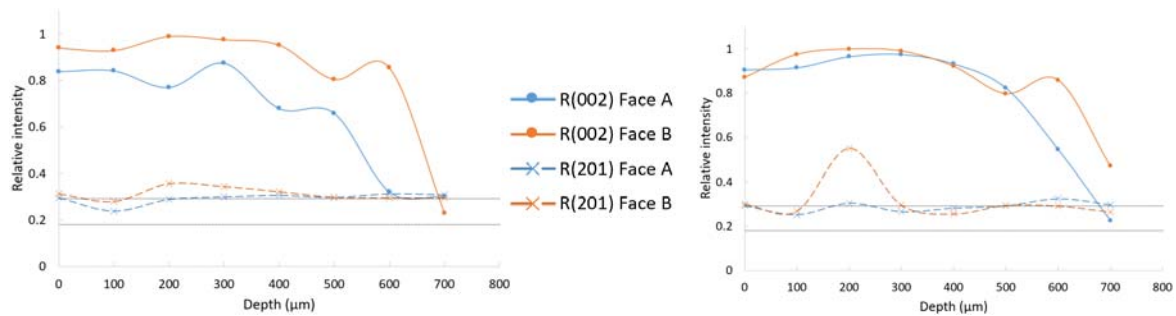
Fig. 5. Orientation coefficients of (002) & (201) planes for $Sr_{1.5}Ba_{0.5}TiSi_2O_8$ samples crystallized in Al2O3 (left) and ZrO2 (right) (Ra = 0.02 µm ; 900°C)

Conclusion

Crystallization of $Sr_2TiSi_2O_8$ glass-ceramics realized by an isothermal treatment in powder bed shows that the surface roughness has an influence on the orientation over depth, whereas the powder only affects the nucleation time. Substituting Sr by Ba leads to a strong volume crystallization, but with a constant (002) orientation over 600 µm below the surface.

Acknowledgements

References

[1] A. Halliyal, A. Safari, A. S. Bhalla, R. E. Newnham, and L. E. Cross, "Grain-oriented glass-ceramics for piezoelectric devices," Journal of the American Ceramic Society, vol. 67, no. 5, pp. 331–335, 1984.
[2] T. Höche, R. Keding, and C. Rüssel, "Microstructural characterization of grain oriented glass ceramics in the system Ba2TiSi2O8," Journal of Materials Science, vol. 34, pp. 195–208, 1999.
[3] R. Müller, E. D. Zanotto, and V. M. Fokin, "Surface crystallization of silicates glasses: Nucleation and kinetics," Journal of Non-Crystalline Solids, vol. 274, pp. 208–231, 2000.

46

Current dominating paths through ZnO varistor ceramics

B. Kaufmann[1], M. Hofstätter[1,2], N. Raidl[1,2],
P. Supancic[1,3]

[1] *Institut für Struktur- und Funktionskeramik, Montanuniversität Leoben, Peter-Tunner-Straße 5, 8700 Leoben, Austria, benjamin.kaufmann@unileoben.ac.at*
[2] *AMS, Tobelbader Strasse 30, 8141 Premstaetten, Austria*
[3] *Materials Center Leoben Forschung GmbH, Roseggerstraße 12, 8700 Leoben, Austria*

Abstract
This work attempts a comprehensive characterization of n-doped ZnO varistor ceramics in regard to their electrical functionality and introduces multiscale modelling tools for simulating device performance.

Keywords
Zinc oxide, varistor, electrical characterization, piezoelectric, micro thermography

Introduction
N-doped ZnO ceramics are vital in today's electronic industry. One of their most popular scopes is based on the sought property of being a voltage dependent resistor (VDR). Up to a certain voltage the material is non-conductive. Exceeding this voltage limit the conductivity of the ceramic increases by several orders of magnitude. This unique trait is used in myriads of electronic devices where it acts as overvoltage protection element. From low voltage applications in microelectronics to high voltage usage in transformer stations, almost all modern VDRs, or "varistors" (variable resistors), are made from n-doped ZnO ceramics.

Although, the varistor effect of sintered ZnO is known since the 1960's and a lot of work was done in this field to explain the sudden increase of conductivity the strict dependency on sinter parameters as well as the influence of the complex microstructure are not sufficiently understood. Especially the urge to create even smaller, versatile and reliable parts brings manufacturers to the limits of their abilities. For further enhancement and down-scaling of varistors a better understanding of the microscopic processes is needed.

In this work, a number of delicate experimental methods are used in order to investigate the varistor behavior of modern low voltage devices with dimensions in the sub-millimeter range: micro lock-in infrared thermography (MLIT) (Fig. 1) to detect current paths [1], a micro 4-point method (M4PM) system (Fig. 2) to measure the current-voltage characteristics between single ZnO grains, electron back scattering diffraction (EBSD) to determine grain orientations and stress tests to verify the influence of the piezoelectric effect on the varistor behavior. Furthermore, simulation tools were developed and a realistic model of the microstructure was set up in order to describe and predict the electrical properties of modern low voltage VDRs.

47

The first attempts to describe these properties with the help of 2D microstructural models were made in the 1990's where it was found that current is localized at electrically favorable paths. [2, 3, 4, 5]
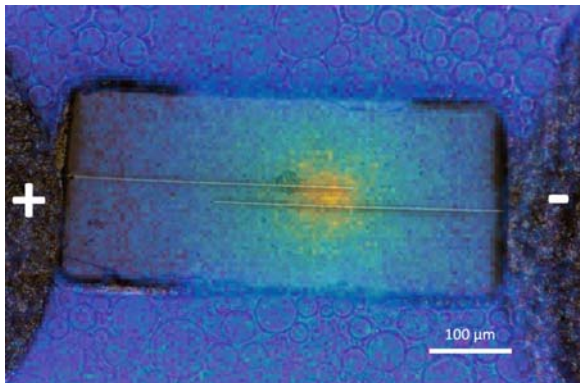
Fig. 1. MILT image of a varistor; warm colors indicate a dominant current path.
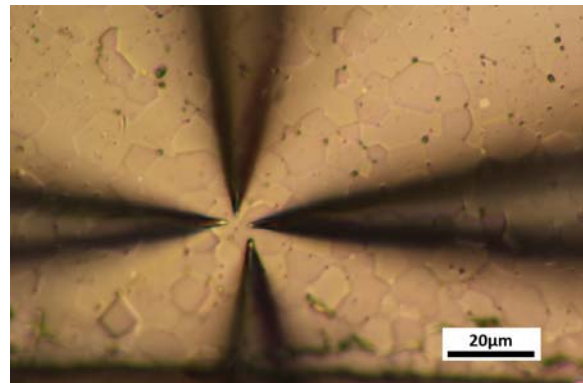
Fig. 2. Micro 4-point measurement between two individual ZnO grains.

In our work we use a more realistic 3D model to study the influence of microstructural characteristics like, for example, the grain size distribution [6] and combine this model with experimental data. Our focus is on low voltage varistors where only a few or even a single grain boundary can determine the electrical behavior of a device. The found results deepen the knowledge of influencing microscopic factors on ZnO varistor performance and show that in particular the grain orientations have a strong influence on path selection and current-voltage characteristics.

48

Results and discussion

MLIT investigations exhibited that different current paths can form, depending on voltage polarity. [1] (Fig. 3) M4PM measurements showed that grain-to-grain contacts can be asymmetric [7] and make a contribution to polarity dependent path formation. The electrode-to-grain contacts are even more asymmetric and were found to behave like Schottky diodes with Schottky barrier heights between 0.4eV and 0.55eV. (Fig. 4)
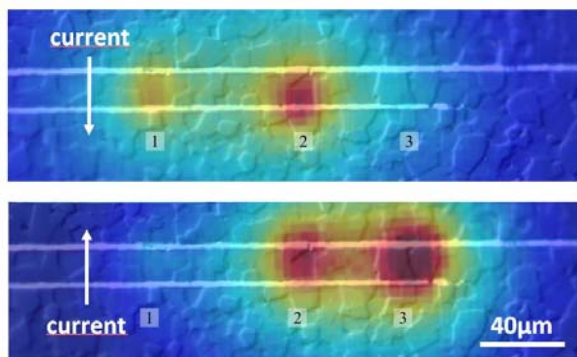
Fig. 3. MILT image showing different currents paths depending on voltage polarity, reprinted from figure 4 in [1].
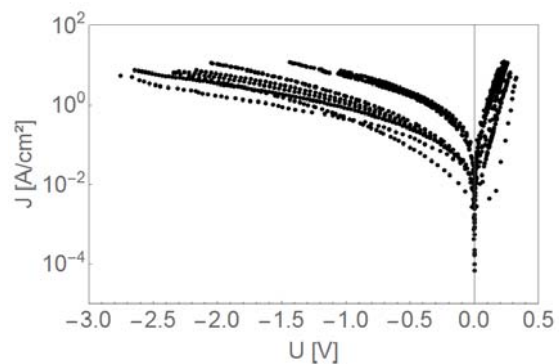
Fig. 4. I-V characteristics of electrode-to-grain contacts show typical Schottky behavior.

Compared to the grain-to-grain contacts the electrode-to-grain contacts are three orders of magnitude more conductive. However, the electrode-to-grain conductivity is distributed over a range of more than a magnitude. I.e. some of these Schottky contacts are more than ten times more conductive than another. This, and asymmetric grain-to-grain I-V characteristics, is regarded as the main reason for polarity dependent current path selection in the low voltage varistors under investigation. Comparison with EBSD data revealed a correlation between grain orientations (c-axis of the hexagonal wurtzite structure to the electrode surface) and Schottky barrier heights. (Fig. 5)

ZnO is polar. One side of a crystal is terminated with a single atomic layer of O atoms, while the other side is terminated with Zn atoms. The surface termination of the grains has been determined by investigation of etching patterns. [8]
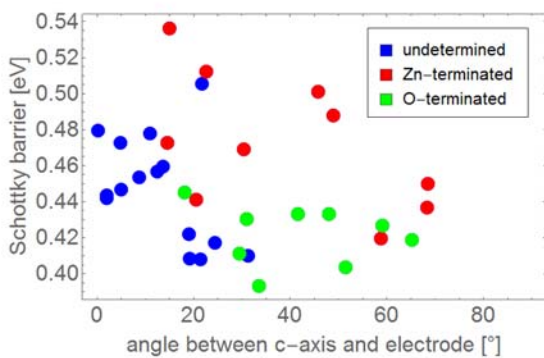
Fig. 5. Schottky barrier heights compared to grain orientations.
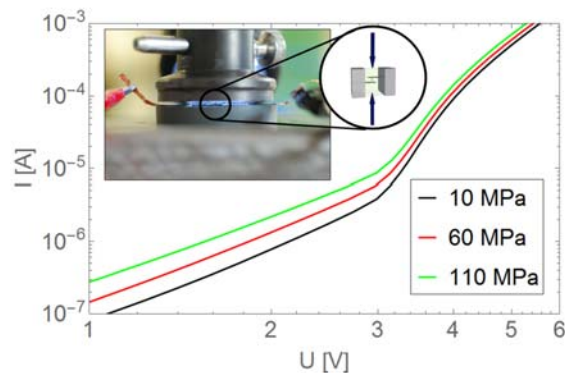
Fig. 6. I-V characteristics of a varistor under different stress loads.

49
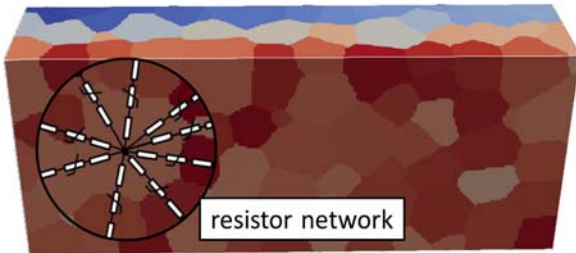
Fig. 7. 3D model of the ZnO microstructure as a basis for a resistor network.
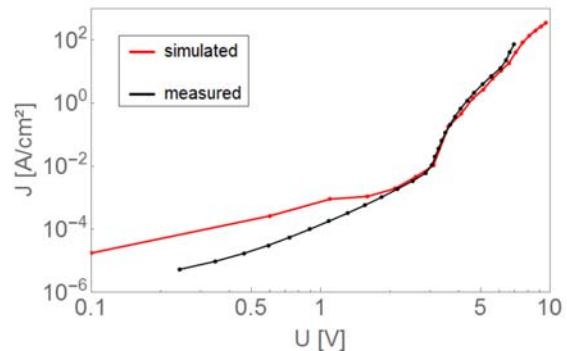
Fig. 8. Comparison between a simulated and a real I-V curve of a VDR.

The mean Schottky barrier height of the grains contacting an electrode with their O-terminated side was found to be 0.42eV, whereas the mean Schottky barrier height of the grains with a Zn-terminated side to an electrode was found to be 0.47eV. Higher Schotty barriers for Zn-termination are consistent with other ZnO-metal contact investigations reported in the literature. [9]

Furthermore, the influence of mechanical stress on the I-V characteristics was studied where it was found that stress can increase leakage currents. (Fig. 6) This effect is attributed to piezoelectrically induced charges in the grain boundaries. [10]

For describing the I-V characteristics of low voltage VDRs, a 3D model of the ZnO microstructure was used and a network of variable resistors (the grain boundaries) was build up. (Fig. 7) The grain-boundary characteristics were adopted from M4PM measurements and the electrical network was solved numerically. Good agreement could be achieved between the calculated and the real I-V curves of low voltage varistors. (Fig. 8)

Conclusions

The combination of detailed investigations of the ZnO microstructure with complementary experimental methods and computer models were demonstrated to be successful in describing the electrical characteristics of low voltage ZnO varistors. The acquired knowledge provides fundamental understanding of varistor behavior and affords a promising basis for device improvement.

Acknowledgements

References

[1] M. Hofstätter, N. Raidl, B. Sartory, P. Supancic, Nonlinear Lock-In Infrared Microscopy: A Complementary Investigation Technique for the Analysis of Functional Elektroceramic Components, Microsc. Micoranal., 21 (2015) 1145–1152

[2] M. Bartkowiak, G. D. Mahan, Nonlinear currents in Voronoi networks,Phys. Rev. B, 51(16) (1995) 10825–10832.

[3] A. Vojta, T. Vojta, Current localization in nonlinear inhomogeneous media, J. Phys: Condens. Matter, 8 (1996) 461–467.

[4] A. Vojta, D. R. Clarke, Microstructural origin of current localization and "puncture" failure in varistor ceramics, J. App. Phys.,81(2) (1997) 985–993.

[5] H. Wang, M. Bartkowiak, F. Modine, R. Dinwiddie, L. Boatner, G Mahan, Nonuniform Heating in Zinc Oxide Varistors Studied by Infrared Imaging and Computer Simulation, J. of the American Ceramic Society, 81(8) (1998) 2013–2022.

[6] M. Hofstätter, Modellierung des elektrischen Verhaltens von Varistoren, PhD Thesis, Montanuniversität, Leoben, 2013.

[7] A. Nevosad, M. Hofstätter, P. Supancic, R. Danzer, C. Teichert, Micro four-point probe investigation of individual ZnO grain boundaries in a varistor ceramic, Journal of the European Ceramic Society, 34 (2014) 1963–1970

[8] N. Raidl, Einfluss des Gefüges auf die elektrischen Eigenschaften von Varistoren, PhD Thesis, Montanuniversität, Leoben, 2017.

[9] L. J. Brillson, Y. Lu, ZnO Schottky barriers and Ohmic contacts, J. Appl. Phys. 109 (2011) 121301

[10] N. Raidl, P. Supancic, R. Danzer, M. Hofstätter, Piezotronically Modified Double Schottky Barriers in ZnO Varistors, Adv. Mater., 27 (2015) 2031–2035

_____

A link between tool-life of WC-Co cutting tools coated by PVD TiAlN and the damping capacity spectra

S. Adjam[1], D. Mari[1]

[1] *Ecole Polytechnique Fédérale de Lausanne, SB IPHYS LPMC, Station 3, 1015 Lausanne, Switzerland, samy.adjam@epfl.ch , daniele.mari@epfl.ch*

Abstract

Cemented carbides represent a group of materials that is widely used for manufacturing cutting tools. Internal friction and elastic modulus measurements have been performed on WC cemented carbides bound with two different Co concentration and coated by physical vapor-deposited CrN/AlTiN. For all specimens, the internal friction spectrum measured in the 700-1400 K temperature range exhibits three peaks (P1, P2 and P3) and a high temperature exponential background. For WC-6wt.%Co uncoated specimen, the peaks P1, P2 and P3 appear respectively at about 920 K, 1125 K and 1355K in the 1Hz frequency range. The uncoated reference material was compared with coated grades. It is observed that P1 temperature is different in samples where the thin film is deposited. Such an effect may be related to residual stress relaxation stemming from the coating. Surprisingly, a strong correlation between the P1 temperature shift in coated samples and the tool life was found in all grades examined.

51

Keywords

WC-Co cemented carbides, PVD thin films, Mechanical Spectroscopy, Cutting tool lifetime

Introduction

Cemented carbides are tough and hard materials consisting of carbide grains embedded in a metallic binder that are widely used for cutting tools applications. The mechanical properties of cutting tools are closely related to their complex structure and efforts have been constantly devoted to optimizing their tool-life. Generally, WC-Co cemented carbides tools are used with TiAlN surface coatings. In this work, we demonstrate that there is a direct link between the tool-life, a macroscopic property, and the damping capacity of the material, which is a microscopic property.

The samples studied in this work contain either 6wt.%Co or 10wt.%Co and are coated with various types of CrN/AlTiN Arc-PVD layers with thickness between 4 and 12 μm.

Tool life measurements were made by turning a grooved steel piece that simulates interrupted cutting.

Due to their complex morphology, the mechanical properties are tested by using a technique capable of dissociating the effects of their different constituents. This technique, named mechanical spectroscopy, evaluates the damping capacity of a

_____

material caused by the movements of its microstructural defects, such as point defects, dislocations and grain boundaries. To be able to measure such damping, periodic stress oscillations at a certain amplitude σ_0 and angular frequency ω are applied to the sample:

$$\sigma = \sigma_0 \cdot \exp(i\omega t)$$

inducing the mechanical strain response:

$$\varepsilon = \varepsilon_0 \cdot \exp(i\omega t - \delta)$$

ε_0 being the strain amplitude and δ the phase lag between stress and strain caused by anelastic material behavior. The damping capacity of the material, called Internal Friction (IF), is then related to tan(δ). Its definition being given by:

$$IF = \tan\delta = \frac{1}{2\pi}\frac{\Delta W_{diss}}{\Delta W_{el.max.}}$$

where ΔW_{diss} is the energy dissipated during one oscillation cycle and $\Delta W_{el.max.}$ is the maximum stored elastic energy. Assuming a linear relationship between stress, strain and their time derivatives, the internal friction IF=IF($\omega\tau$) for a standard anelastic material is given by:

$$IF = \Delta\frac{\omega\tau}{1 + (\omega\tau)^2}$$

where ω is the oscillation angular frequency, τ is the relaxation time and Δ is the amplitude (strength) of the relaxation. Such a function appears as a peak, called Debye peak, exhibiting a maximum at $\omega\tau$=1. In case of a distribution of relaxation times, a broadening of the peak is observed. If the Debye peak is thermally activated, the relaxation time would then be given by:

$$\tau = \tau_0 \exp(E_{act}/k_B T)$$

where τ_0 is the limit relaxation time of the Debye peak and E_{act} its activation energy described by the following Arrhenius relationship:

$$\tau_0 = \left(\frac{1}{\omega}\right)_{1/_{T=0}} \qquad E_{act} = -k_B\frac{d(\ln\omega)}{d(1/T)}$$

The IF shows a peak both as a function of temperature and frequency. When a relaxation is caused by stable microstructure, the quantities E_{act} and τ_0 are of physical meaning. In the case of a changing microstructure, the quantities Δ, E_{act} and τ_0 will depend on the thermal history and more generally on the temperature of the measurement.

In this study, mechanical spectroscopy measurements are performed using a forced oscillation pendulum and carried out both at a fixed frequency while varying the temperature, and vice versa in isothermal conditions while varying the frequency. The resulting IF spectrum provides information about the mobility of structural defects as a function of frequency and temperature, representing mostly near surface phenomena, since the higher stresses occur at the edges of the sample.

52

Results and discussion

For all specimens, the characteristic internal friction spectrum measured in the 700-1400 K temperature range exhibits three peaks: P1, P2 and P3. The spectrum was deconvoluted with three Debye peaks and an exponential background (reflecting the presence of at least one relaxation peak at very high temperatures). At 1 Hz , the peak P1 appears at about 920 K and P2 at about 1125 K, for the uncoated reference samples (see Fig.1). These two peaks P1 and P2 should be related respectively to partial and perfect dislocations in the Cobalt phase [1,2,3]. The third peak P3 appears at about 1355 K at 1 Hz (see Fig.1) and is associated with grain boundary sliding of the WC hard phase [2,3].
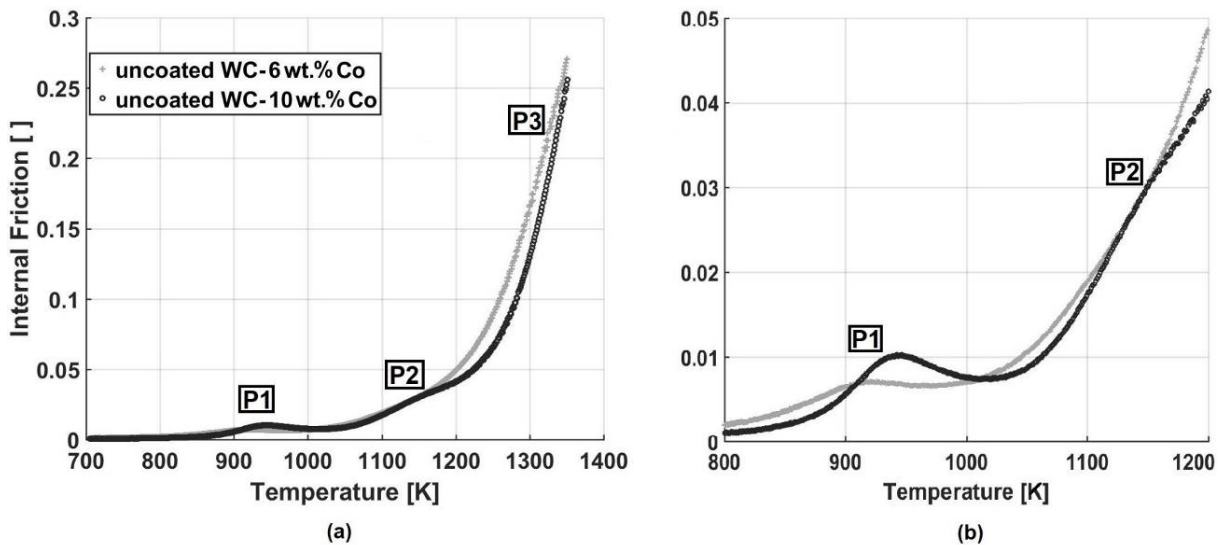
Fig. 1. Effect of the cobalt content on the internal friction spectra.
WC-6wt.%Co (light grey) and WC-10wt.%Co (black) for two scales (a) and (b).

It can be observed that the P1 peak is sensitive to heat treatment; this may indicate a metastable nature. Thereby, all analysis have been carried out after three annealing processes at 1050K of several hours. The relaxation peak P1 appears to be thermally activated. An increase in frequency induces a shift of the relaxation peak center position to higher temperatures. However, the analysis of the dependence of the temperature and frequency position of this peak according to Arrhenius law leads only to non physical and apparent values.

The previous analysis of uncoated WC-Co samples can be used for a comparative study of the effects of the application of various PVD coatings on cemented carbides on the IF spectra. The peak P1 appears to be sensitive to the presence of a coating, one can observe (Fig. 2(a)) a systematic shift to lower temperature of the peak in the 1Hz frequency range. The P1 temperature shift has been reported in Fig. 2(b) together with the tool-life data as a function of their coating. There is a clear correlation between these two values. The shift in temperature of the peak P1 becomes an indicator of the influence of a coating on the lifetime of a cemented carbide cutting tool. The change in position of peak P1 may reflect the influence of a

53

PVD layer on the movement of the dislocations occurring in the cobalt phase underlying the coating. A peak displaced at a lower temperature generally corresponds to a shortening of the length of the corresponding dislocations, and thus indirectly to a hardening of the cobalt metal phase under the coating.
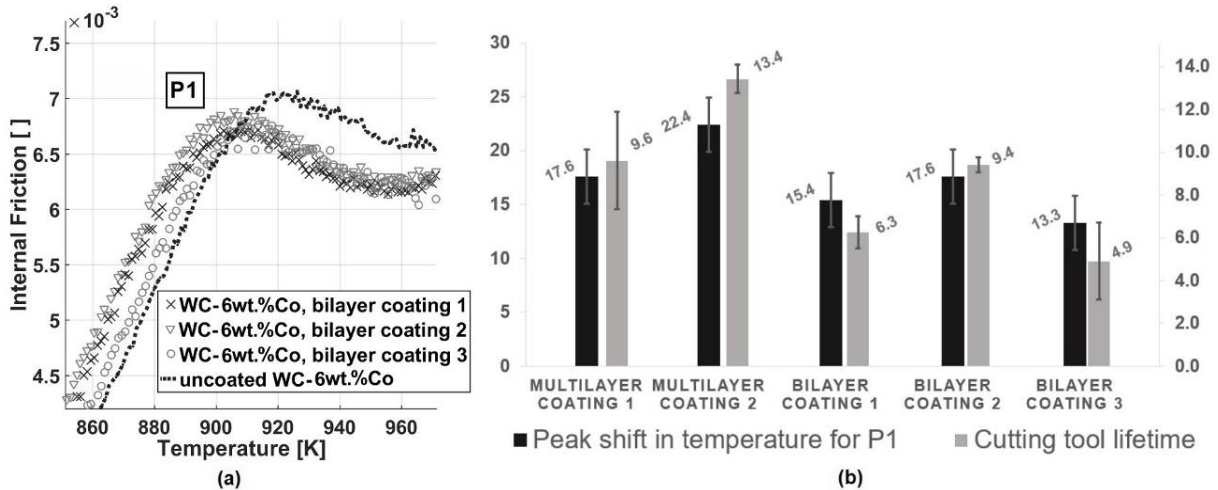
Fig. 2. IF measurements and cutting tool lifetime (a) Effect of the coating on the P1 internal friction peaks. (b) Variation of the position of the P1 internal friction peaks versus the cutting tool life as function of their coating.

Conclusions

54

Good coating adhesion and durability are crucial needs in industrial processes; unfortunately, they depend on many physical and chemical attributes of the interface, leading to chaotic and mainly qualitative results in most coating adhesion tests. The observed correlation between the P1 temperature shift in coated samples and tool life proves the importance of microstructural defects below the coating and of their mobility for cutting tools; it provides therefore a promising approach for predictive and non-destructive test for coating adhesion and tool durability for composite and complex structured materials in general.

Acknowledgements

References

[1] J.-J. Amman, R. Schaller, Influence of a Changing Microstructure on High Temperature Relaxation Peaks, an Example: WC-11wt.%Co, J. Alloys and Compounds. 211/212 (1994) 397–401.
[2] Mari D. Understanding the mechanical properties of hardmetals through mechanical spectroscopy. Mater Sci Eng A. 2009;521-522:322-8.
[3] K. Buss, High Temperature Deformation Mechanisms of Cemented Carbides and Cermets, Thesis EPFL N°3095, Lausanne, 2004.

In-situ Tensile Testing of SiCf/SiC Specimens Using a Tensile Test Stage within a Scanning Electron Microscope

S. Jordan[1], C. D.Newton[2], M. R.Bache[3], L. Gale[4]

[1] *Institute of Structural Materials, Swansea University, Swansea, SA1 8EN, UK*
[2] *Louise Gale, Rolls-Royce plc, P.O.Box 31, Derby, DE24 8BJ, UK*

Abstract
The present paper will introduce the use of scanning electron microscope based, in-situ testing as a method of detecting cracking in a SiCf/SiC CMC at room temperature. Small scale tensile specimens were prepared, but still sampling multiple longitudinal and transverse fibre tows. Monotonic loading was applied to initiate cracking, whilst contemporary time lapse imaging was recorded to demonstrate the development of surface cracks within the matrix phase.

Keywords
In-situ, Ceramic Matrix Composite, Tensile, Mechanical characterization, Scanning Electron Microscope.

Introduction
The next generation of high temperature materials to replace traditional super alloys is likely to be Ceramic Matrix Composites (CMC's), due to the superior high temperature mechanical properties demonstrated at temperatures exceeding 1000°C and the weight savings offered by the much lighter material.

To fully utilize the unique properties of this material a thorough understanding of the fracture and damage mechanisms occurring during loading is required.

Research within this field is mostly aimed at macroscopic investigation of surface cracks within the matrix during loading. Researchers have attempted to model and predict crack propagation within the bulk matrix, with varied success, due to the unpredictable nature of the materials response to stress and strain.

This study describes a micro scale investigation technique using an in-situ tensile testing stage within a Scanning Electron Microscope. The mechanisms of crack initiation and propagation along with the phenomenon of crack closure can be observed and studied through the high-resolution images produced by the SEM. The use of high resolution images allows strain fields to be resolved using Digital Image Correlation and time lapse video to observe crack opening and closing.

The use of stepped loading conditions allowed high resolution images to be taken between steps.

In-situ testing, using small scale specimens is a new field being increasingly utilized to investigate materials. Previous work with CMC's has been completed using in-situ equipment by Tracy [1] at an elevated temperature of 795°C and Sevener et al [2] investigating crack openings and displacements at room temperature. The work carried out by these researchers looked at cracks around fibres at a very small scale

_____

on polished specimens. The work in this study evaluates larger scale crack formation on a MI Sic$_f$/Sic CMC without polishing.

Several tests were completed using a stepped tensile load at ambient temperature to examine crack formation and propagation within the surface plane. To further examine a specific area within the bulk, a stress concentration was added in the form of a notch. The same test parameters as test 1 were followed for repeatability. The specimens used can be seen in (Figure 1.)

(a)

(b)
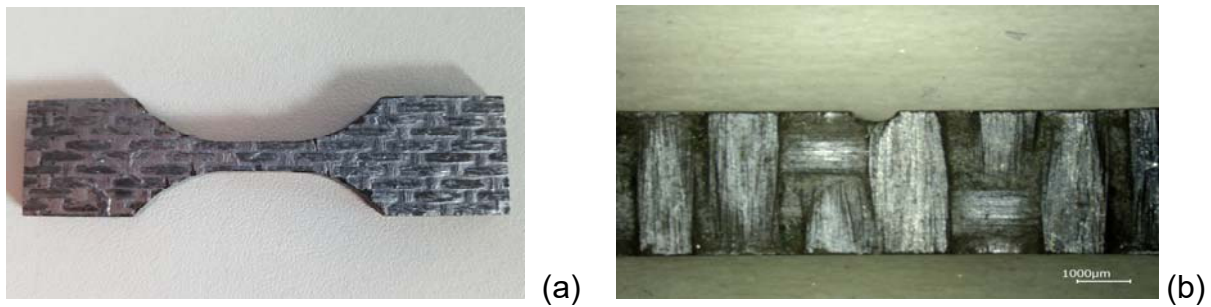
Fig. 1. Test specimens (a) Plain (b) Notched

Results and discussion

Tests completed using plain specimens exhibited parallel crack spacings across the bulk surface as seen in (Figure 2).

Notched specimens were used to increase the stress within a section to observe the trend produced. Specimens taken to failure exhibited a central crack at the root of the notch causing failure as shown in (Figure 3). Several other cracks appeared from the notch or within proximity but ultimately were not fatal.

56

(a)

(b)
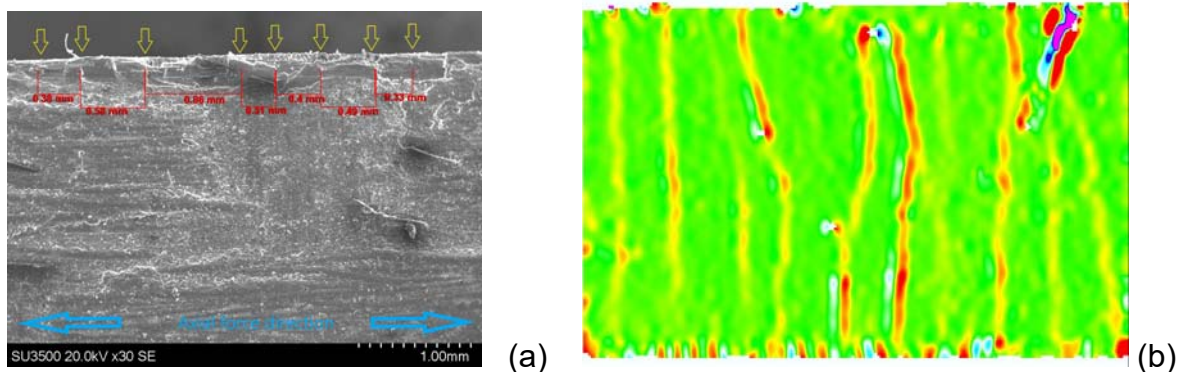
Fig. 2. Plain SiC$_f$/SiC specimen crack formation (a) SEM image (b) DIC image 50 Newtons from failure.

Conclusions

Micro-scale cracking mechanisms that occur within the bulk matrix can be observed and studied using the in-situ tensile stage with success. Progressive high-resolution

images resolved with a digital image correlation program can highlight crack formation and propagation.

Initial testing has shown a pattern of cracking observed along both edges of the plain specimen. There appears to be no initial indication of which crack is going to ultimately fail the specimen. As the global loading is increased greater levels of strain are observed within certain cracks and finally one crack dominates. This dominating crack propagates through the thickness of the specimen via several mechanisms including shearing and joining up of other cracks within the planes as can be observed in (Figure 4).

 (a) (b)
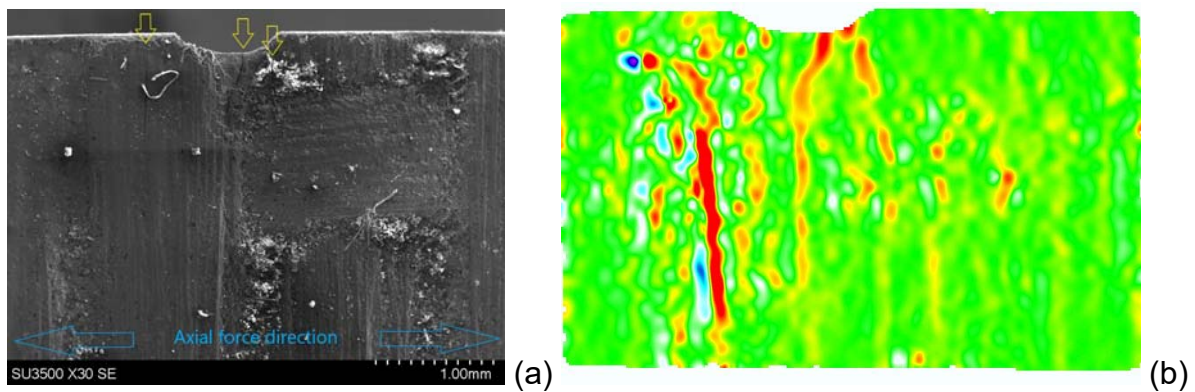
Fig. 3. Notched SiCf/SiC tensile test result (a) SEM Image (b) DIC Image 50 Newtons from failure.

57

 (a) (b)
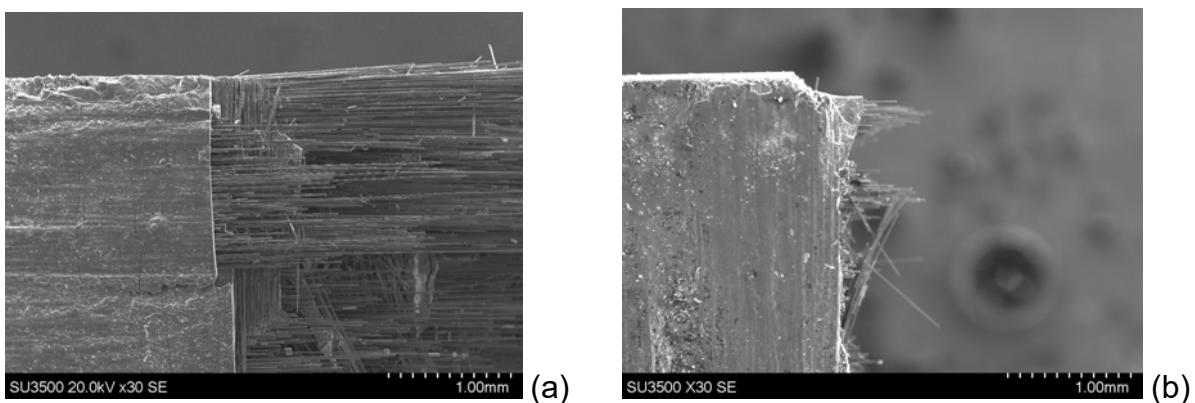
Fig. 4. Fractured tensile specimens (a) Plain (b) Notched

The in-situ tensile testing method has shown that it can be used as a method for early detection and identification of cracking before and during the proportional limit. When used in conjunction with DIC software cracks can be identified before observation with the naked eye.

Acknowledgements

_____

References

[1] J. M. Tracy, "Multi-scale Investigation of Damage Mechanisms in SiC / SiC Ceramic Matrix Composites by Jared Michael Tracy" pp. 1–188, 2014.
[2] K. M. Sevener, J. M. Tracy, Z. Chen, J. D. Kiser, and S. Daly, "Crack opening behavior in ceramic matrix composites," *J. Am. Ceram. Soc.*, no. May, pp. 1–14, 2016.

_____

_____

Detecting High Temperature Inhomogeneous Strain and Damage Evolution in Notched SiCf/SiC Specimens under Fatigue and Stepped Loading Conditions

C. D. Newton[1], S. Jordan[1], M. R. Bache[1], L. Gale[2]

[1] Institute of Structural Materials. Swansea University, Swansea, SA1 8EN, UK
[2.] Rolls-Royce plc, P.O.Box 31, Derby, DE24 8BJ, UK

Abstract

Many previous mechanical assessments of CMC's have concentrated on standard bulk material properties and from such studies the SiCf/SiC system has shown significant promise. However, before such materials can be selected for engineering service, more sophisticated mechanical characterisation is vital in support of a fundamental understanding of deformation in these materials.

The complex structural architecture and inherent processing artefacts within ceramic matrix composites combine to induce inhomogeneous deformation and damage prior to ultimate failure. Sophisticated mechanical characterisation is vital in support of a fundamental understanding of deformation in ceramic matrix composites. On the component scale, "damage tolerant" design and lifing philosophies depend upon laboratory assessments of macro-scale specimens, incorporating typical fibre architectures and matrix under representative stress-strain states.

Bulk measurements of strain via extensometry or even localised strain gauging will fail to characterise such inhomogeneity when performing conventional mechanical testing on laboratory scaled coupons. The current research has, therefore, applied advanced techniques such as digital image correlation (DIC) and acoustic emission (AE) along with post-test in-situ scanning electron microscopy, to the high temperature (800°C) axial assessment of a SiCf/SiC composite under cyclic fatigue and stepped cyclic loading. Data from these separate monitoring techniques plus ancillary use of optical inspection were correlated to monitor the onset and progression of damage during loading at high temperatures.

59

Keywords

SiCf/SiC Ceramic Matrix Composite, High Temperature DIC, Acoustic Emission, In-Situ SEM.

Introduction

Ceramic matrix composites (CMC's) offer a combination of low density and thermal stability for structural engineering applications where long-term exposure to high temperature environments is envisaged. The present paper will describe tests on double edged notched (DEN) coupons subjected to stepped axial stress, with real-time surface strain distributions measured via digital image correlation (DIC). Associated acoustic emission (AE) signals were also recorded to allow for a correlation between surface and bulk damage progression and also to monitor the

_____

_____

spatial distribution of damage events occurring throughout the critically stressed volume of the composite (for test set-up see Fig.1).
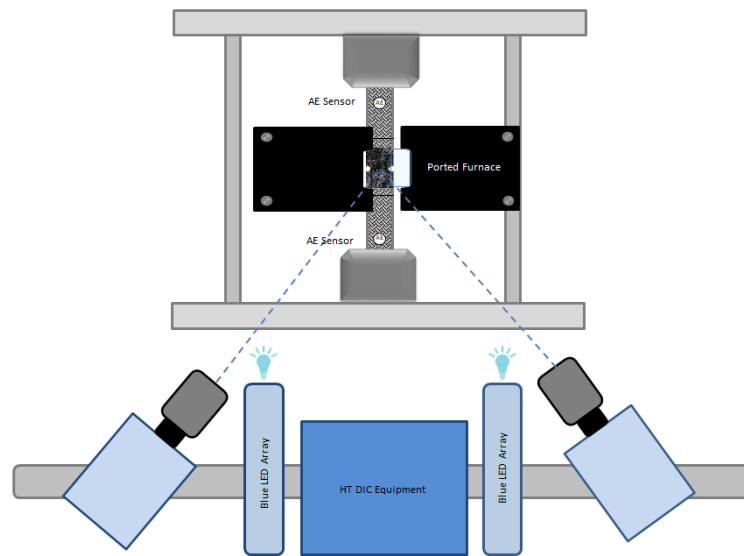
Fig. 1. Test Set-up.

Additional use of an in-situ SEM tensile stage combined with DIC also provides insight into the crack development and propagation path on the surface of the composite. Flat panels of approximate thickness 5mm and dimensions 150 x 230mm were manufactured by Rolls-Royce High Temperature Composites Inc. via a proprietary chemical vapour and melt infiltration based process. Fibre bundles were interwoven in a 0-90º format with a 5-harness satin weave architecture and fibre tow spacing of 6.3 end per centimetre. A more detailed description of the processing and architecture of this CMC variant has been reported previously [1]. DEN mechanical specimens were extracted from these panels, retaining the panel surfaces. Specimens incorporated 0.8mm radius notches into the central span of the sample with the width of the load bearing section being 8mm. Due to the proprietary nature of the mechanical data, stresses, strains and associated AE measurements will be quoted as normalised data against the peak values attained from each technique over the course of the test.

60

Results and discussion
Fig. 2 displays the DIC strain distribution maps along with the cumulative acoustic energy plot for a selected DEN specimen. The data shown below pertain to a single specimen tested using stepped cyclic fatigue, with peak cyclic stress increased every 10,000 cycles until failure or a significant damage event was noted. During this test, the trends in data from the different monitoring techniques correlated very well. Each method indicated an increase in response over the first 1k cycles, leading to a near steady rate of signal accumulation for the next ≈30k cycles until the initial onset of failure was detected by both DIC and AE almost simultaneously. At this point both techniques exhibit significant increases in damage recorded immediately following

_____

_____

the stress increase at stage 4. At this point DIC strain maps began to present indications of inhomogeneous strain development, with the regions of highest strain located at the root of the left hand notch when viewed from the "front" face of the specimen. Along with a relatively rapid accumulation in the localized strain, large high energy AE events were recorded, which retrospectively, due to the late stage of the test (and from previous work [2]) are expected to be fibre failures in the region of highest strain accumulation. At this point (≈40k cycles) the test displayed a significant region of high strain development which was accruing very rapidly, in order to preserve the specimen for post-test SEM inspection the test was terminated at this point (N~39,000).
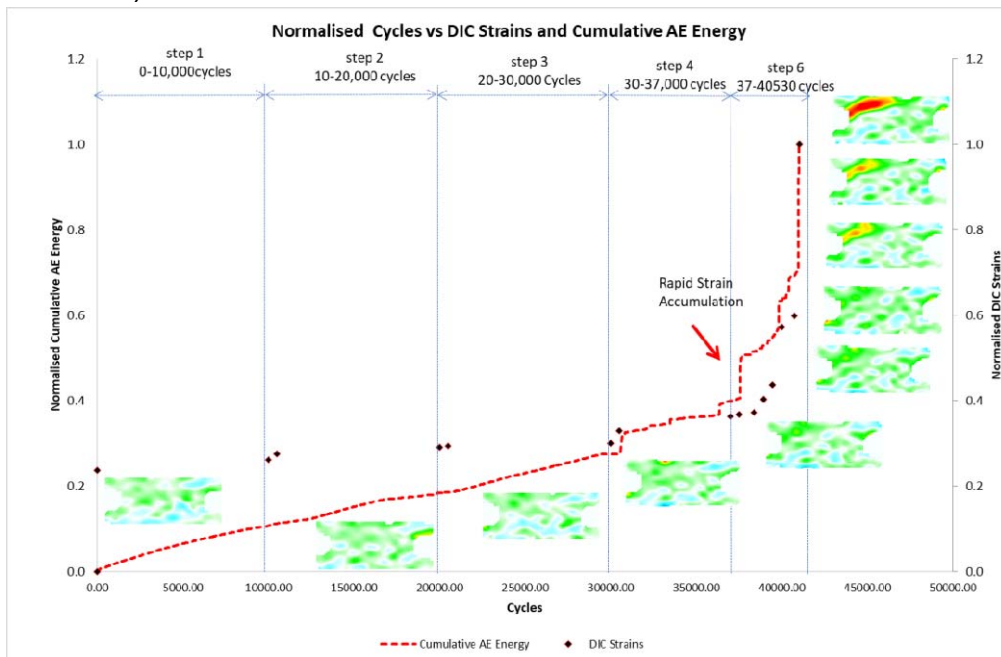
Fig. 2. Normalised DIC strains and cumulative AE energy as a function of normalized cyclic life.

The AE data were also analysed for spatial distribution, Fig.3. The time of flight for the acoustic signal from each single event to travel to the opposing AE detector positions at either extremity of the specimen gauge section was calculated in order to back extrapolate to the axial location of the event. This indicated that, in line with expectation from the macroscopic inspection of specimens, the majority of events were concentrated near the plane spanning the net section between the notches. This behaviour was not exclusive, however, particularly during the first 30k cycles of the test, with some events distributed up to 85mm either side of the mid-plane. After this point the marked steps in the cumulative AE signal are matched by high densities in the individual events occurring close to the ultimate plane of failure.

Separate use of an in-situ tensile stage within an SEM provides confidence in the high temperature DIC. This technique allows for the location of otherwise 'invisible' matrix cracks surrounding the dominating 'major' crack which has developed from the root of the notch as shown in in Fig.4. Additional images clearly show fibres bridging the crack below the surface of the specimen with several fibres exposed via pull-out

_____

or individually fractured. This behaviour agrees with the increased steps in the AE signal from Fig.2 suggesting an increased level of fibre failure late in the test which also aligns with evidence from alternative laboratories [2,3,4]. It should be noted that the damage appearing in Fig.4 is the opening of pre-existing cracks imparted in the composite during the very first loading cycle and illustrated here up to a maximum condition of 0.6 P_{max}.
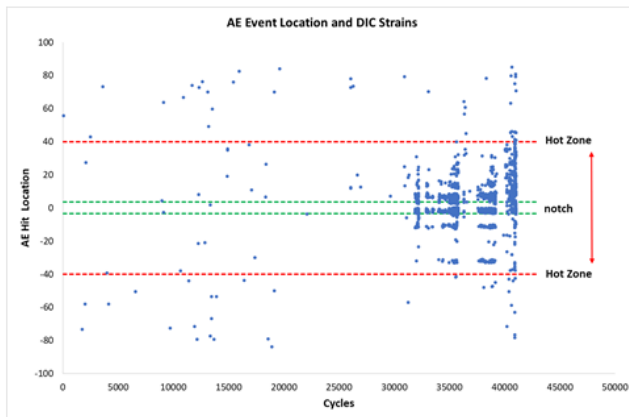
Fig.3. AE signal distribution.
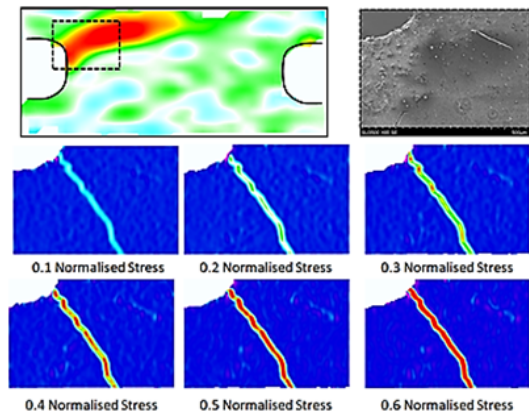
Fig.4. In-situ SEM DIC results.

Conclusions

Based upon the current research the following conclusions may be drawn:

- Acoustic emission and digital image correlation techniques are both capable of detecting the initiation and progression of damage at elevated temperature, with correlation possible between the contemporaneous monitoring techniques.
- Acoustic emission was the most reliable single method to detect damage, the eventual onset of failure and locations of major events.
- Additional use of an in-situ SEM tensile stage and DIC also provided knowledge of early stage, localised deformation and fracture.

Acknowledgements

References

[1] Z. Quiney, J. Jones, M. Bache., Inspection of SiC$_f$/SiC Ceramic Matrix Composite Specimens Employed for Thermo-mechanical Fatigue Experiments via Laboratory X-ray Computed Microtomography, 7th International Symposium on NDT in Aerospace, Bremen, Germany (2015).

[2] M.P. Appleby, D. Zhu, G.N. Morscher. Mechanical properties and real-time damage evaluations of environmental barrier coated SiC/SiC CMC's subjected to tensile loading under thermal gradients, Surf. Coat. Tech. 284. (2015). 318-326

[3] G. Ojard, M. Mordasky, R. Kumar. Acoustic emission monitoring in ceramic matrix composites: Effects of weaves and features. AIP conference proceedings 1949, 230028, (2018)

[4] C.E. Smith, G.N. Morscher, Z.H. Xia., Monitoring damage accumulation in ceramic matrix composites using electrical resistivity, Scr. Mater. 59(4). (2008).

62

Ceramic laminates integrating ZrB$_2$/SiC and SiC layers for TPS applications

E. Padovano[1*], F. Trevisan[1], S. Biamino[1], O. Ostrovskaya[1] and C. Badini[1]

[1] *Politecnico di Torino, Department of Applied Science and Technology, Corso Duca degli Abruzzi 24, 10129 Torino.*
[*] *Corresponding author. E-mail: elisa.padovano@polito.it*

Abstract

Multilayer structures integrating ZrB$_2$-SiC layers stacked in between SiC ones were successfully prepared using tape casting technique and pressureless sintering. Thin cracks propagated in the composite layers without affecting SiC ones; their formation was due to residual stresses developed in the two materials because of the differences in their CTEs and shrinkage during the cooling from sintering temperature. The measurement of the elastic modulus and the flexural strength of hybrid multilayer evidenced that the presence of these cracks do not significantly affect the mechanical behavior of laminates.

Keywords

Tape casting; Mechanical properties testing; Ceramics; Residual Stresses

63

Introduction

High temperature ceramics, ultra-high temperature ceramics and their composites are considered the most promising candidates for use in sharp leading edges and nose cones of atmospheric re-entry vehicles. These materials show in fact rather good mechanical properties combined with high melting temperatures and high resistance to environmental degradation. Among them SiC and ZrB$_2$-SiC composites are widely used for aerospace applications. It is well known that SiC shows excellent oxidation resistance up to 1600°C since a thin silica passive layer forms on its surface. However at high temperatures and under very low oxygen partial pressure the passive layer can be destroyed owing to active oxidation [3]. In addition cristobalite melts at 1725°C and then it evaporates, while the sharp profiles of space vehicles and hypersonic aircraft demand materials able to sustain temperatures up to around 2000°C. Differently the oxidation of ZrB$_2$ and ZrB$_2$-SiC composites results in the formation of a glassy phase that easily volatilizes, and solid zirconia which melts well above 2000°C. Therefore ZrB$_2$-based ceramics can be used under extreme temperature conditions, but unfortunately their oxidation resistance is much worse than that of SiC below 1700°C [4]. Then it is not possible using a single material showing superior oxidation resistance all over the range of temperatures that are experienced by TPSs. In this paper multilayer structures comprising ZrB$_2$-SiC layers stacked in between SiC ones have been successfully prepared by tape casting and pressureless sintering. The advantage of using laminates is related to their improved toughness with respect to conventional ceramics and the possibility of adjusting their

architecture and chemical composition. Such a kind of structure would allow to hinder the quick recession of TPS when the temperature exceeds 1700°C, thus providing structures able to sustain oxidation in a very wide temperature range. Two kinds of specimens were obtained: multilayer containing ten SiC or ZrB_2/SiC composite sheets and hybrid laminates comprising alternating layers of SiC and ZrB_2/SiC. They were designed according to the following symmetric structure: 3 SiC layers–1ZrB_2/SiC layer-2SiC layers–1ZrB_2/SiC layer-3SiC layers. The effect of composite thickness layers in hybrid structures (ZS-1 and ZS-2) was studied. Moreover the microstructure and the mechanical behaviour of laminates were investigated.

Results and discussion

Table I reports the thickness of SiC and ZrB_2/SiC layers in the different kinds of laminates. The interfaces between the two materials are clearly distinguishable; the thickness of the two composite layers is constant and uniform. Figure 1A and 1B show the microstructure of the hybrid laminates ZS-1 and ZS-2. It was observed a remarkable decrement of layers thickness during the sintering: cross section analysis showed that SiC layers shrank by 32% while the shrinkage observed for ZrB_2-SiC ranged between 45 and 46%. Figure 1C and 1D show the XRD patterns obtained by analysing the layers with different composition contained in the hybrid laminates. No difference was observed with respect to the XRD spectra recorded for laminates fully constituted by identical layers. The only additional phase with respect to SiC and ZrB_2 was carbon; its peak was due to the graphite flakes added as sintering aid and to the residuals of degradation of the organic compounds occurring during the de-binding.

64

Laminates	Layer thickness after sintering [μm]	Relative density [% of the theoretical]	Elastic modulus [GPa]	Flexural strength [MPa]
SiC	163 ± 5	91.9 ± 0.1	339 ± 19	324 ± 24
80ZrB_2-20SiC	105 ± 5	97.3 ± 0.2	444 ± 10	277 ± 29
ZS-1	SiC= 163; ZrB_2/SiC= 75	92.9 ± 1.8	297 ± 14	313 ± 10
ZS-2	SiC= 163; ZrB_2/SiC= 105	93.1 ± 1.0	319 ± 22	289 ± 56

Table I. Composition and mechanical properties of laminates
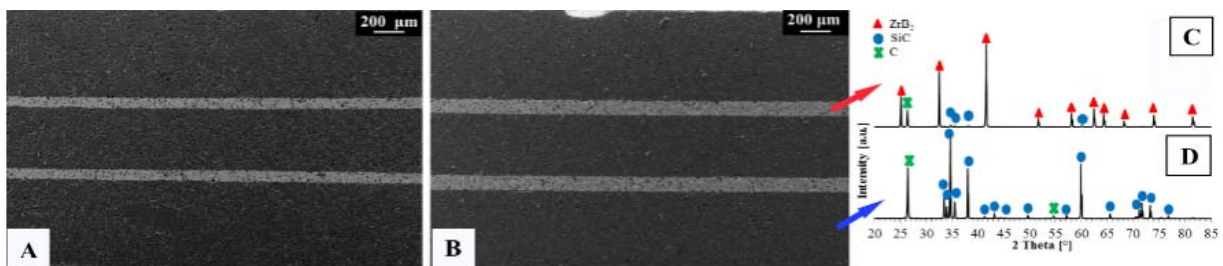
Fig. 1. SEM images of multilayer polished cross section for sample ZS-1 (A) and ZS-2 (B); XRD patterns of the two materials constituent the multilayer (C) and (D).
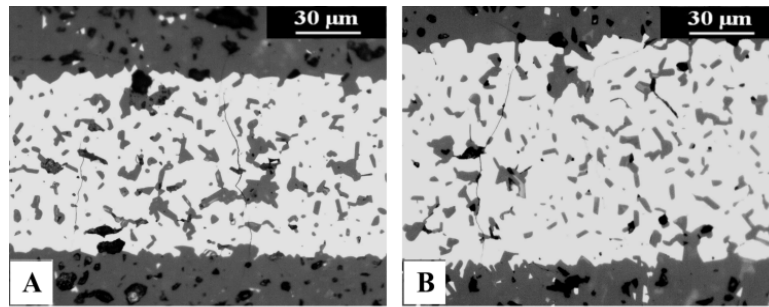
Fig. 2. Microstructure of hybrid laminates: optical images of polished cross section of laminates ZS-1 (A) and ZS-2 (B), detail of the composite layer.

Figure 2A and 2B show some cracks propagating in the composite layer without appreciably affecting the neighbouring SiC ones. These cracks were very thin and they could be observed in both ZS-1 and ZS-2 specimens.

They propagated inside the ZrB_2 matrix in a twisted manner, moving preferentially towards carbon and SiC particles. The presence of cracks was caused by residual stresses which arose from the different sintering shrinkage occurring for SiC and composite layers. In fact the shrinkage of composite layers was higher with respect to the SiC ones, which resulted in tensile residual stresses inside the composite sheets. In addition the presence of cracks was also very likely caused by residual stresses which developed during the cooling from the sintering temperature.

Hybrid laminates integrate SiC and ZrB_2-based composite which show different coefficient of thermal expansion. In fact the CTE of SiC is $5.9 \cdot 10^{-6}$ °C^{-1} (25-2500°C) while that of ZrB_2 is $8.3 \cdot 10^{-6}$ °C^{-1} (25-2500°C) [5,6]. The composite 80%ZrB_2-20%SiC has CTE value, calculated by the mixture rule, of $7.8 \cdot 10^{-6}$ °C^{-1} (25-2500°C). The composite shows higher CTE and consequently its contraction during the cooling from the sintering temperature is higher than for SiC. The mismatch between SiC and composite CTEs causes thermal stresses at the interface between layers with different chemical composition. This results in compressive stresses within layers with lower CTE, that is SiC layers, while tensile stresses develop in composite layers with higher CTE. The extent of the residual stresses depends on the composition of neighbouring layers, their properties (such as elastic modulus and Poisson's ratio) and the thickness of each layer.

For this kind of architecture the tensile residual stress sustained by the composite sheets can be evaluated according to the equation (1) [7]:

$$\sigma_2 = \frac{n_2 \, E_1 \, E_2 h_1 (\alpha_2 - \alpha_1) \Delta T}{n_1 (1 - \nu_1) E_2 \, h_2 + n_2 (1 - \nu_2) E_1 h_1} \qquad (1)$$

Where 1 and 2 are SiC and ZrB_2/SiC respectively, n_i is the number of layers, E_i and ν_i are the Elastic modulus and Poisson's ratio of the ith component, h_i is the thickness of the two kinds of layers, α_i their CTEs (from sintering to room temperature).

The residual stresses in the 75 µm thick composite was found to be around 450 MPa

and was only slightly lower for the 105 μm thick layers. Since this value is higher than the flexural strength of ZrB_2-SiC laminates, the presence of cracks is not surprising. The mechanical properties of laminates integrating different materials are compared in Table I with those of laminates made with all layers of the same composition.

The relative bulk density of multicomponent laminates was comparable to that of multilayer prepared by using only SiC or ZrB_2/SiC sheets. Probably due to the presence of micro cracks inside the composite sheets, the elastic modulus of hybrid multilayer was slightly lower with respect to the value of both one-constituent samples. These modulus values were however closer to those of SiC which represented the main component of ZS-1 and ZS-2 samples.

The flexural strength of hybrid laminates were very similar showing values of 313 MPa and 289 MPa for specimens containing respectively 75 μm and 105 μm thick composite sheets. The flexural strength values of hybrid laminates were close to that containing all layers with composition 80vol%ZrB_2-20vol%SiC. The presence of micro cracks crossing the composite layers without affecting the SiC material did not significantly affect the mechanical properties of the hybrid laminates.

Conclusions

Laminates integrating ZrB_2-SiC layers in between SiC ones were successfully prepared by the tape casting technique and pressureless sintering. The laminates showed the formation of thin cracks propagating only in the composite layers independently from their relative thickness with respect to SiC ones. These cracks were caused by residual stresses that may have arisen owing to various factors: the different sintering shrinkage of SiC and ZrB_2-SiC composite and the different contraction of these two materials occurring during the cooling from sintering temperature. The presence of these cracks weakly affected the mechanical properties of the hybrid laminates.

66

Acknowledgements

References
[1] S. T. Pichon, R. Barreteau, P. Soyris, A. Foucault, J.M. Parenteau, Prel Y., Guedron, CMC thermal protection system for future reusable launch vehicles, Acta Astronaut. 65 (2009) 165–176.
[2] J. Barcena, M. Lagos, I. Agote, C. Jimenez, X. Hernandez, C. Badini, E. Padovano, S. Gianella, SMARTEES FP7 Space Project – Towards a New TPS Reusable Concept for Atmospheric Reentry from Low Earth Orbit, in: 7th Eur. Work. Therm. Prot. Syst. Hot Struct., Noordwijk, The Netherland, 2013.
[3] E.A. Gulbransen, S.A. Jansson, The high-temperature oxidation, reduction, and volatilization reactions of Si and SiC, Oxid. Met. 4 (1972) 181–201.
[4] E. Padovano, C. Badini, E. Celasco, S. Biamino, M. Pavese, P. Fino, Oxidation behavior of ZrB_2/SiC laminates: Effect of composition on microstructure and mechanical strength, J. Eur. Ceram. Soc. 35 (2015) 1699–1714.
[5] J.F. Shackelford, W. Alexander, CRC Materials science and engineering handbook, in: New York, 2001: pp. 1557–1558.
[6] P.N. Bansal, Handbook of Ceramic Composites, Vol 200, 2006.
[7] X. Zhang, P. Zhou, P. Hu, W. Han, Toughening of laminated ZrB_2-SiC ceramics with residual surface compression, J. Eur. Ceram. Soc. 31 (2011) 2415–2423.

_____

_____

Processing effects on sintering of transparent Al$_2$O$_3$ and MgAl$_2$O$_4$ ceramics by FAST/SPS

S. Cottrino[1], V. Garnier[2], G. Fantozzi[3]

[1,2,3] *MATEIS, INSA de Lyon, bât. Blaise Pascal, 20 Avenue A. Einstein, 69621 Villeurbanne Cedex, France, sandrine.cottrino@insa-lyon.fr, vincent.garnier@insa-lyon.fr, gilbert.fantozzi@insa-lyon.fr*

Abstract

Highlights of the paper: (1) Obtain materials as large and transparent as possible by reducing the main transparency losses; (2) Fabrication process optimization of transparent alumina samples: reduce grain growth; (3) Sintering parameters optimization to obtain large size (diameter 40mm) transparent spinel samples

Keywords

Transparency, Alumina, Spinel, Fast sintering

Introduction

The Flash sintering (SPS) is a technique widely used since several years and allows the sintering of material with specific microstructure, not accessible by conventional sintering. It is the case of transparent ceramics, particularly birefringent ceramics which grain size is a limiting parameter to transparency. One of major advantage of Spark plasma Sintering is its fast heating rate. It allows a sintering of ceramics at lower temperature and limits the grain growth. In this work, we will present a fabricated process optimization of two transparent ceramics: alumina (Al$_2$O$_3$) and spinel (MgAl$_2$O$_4$). The objective was to obtain materials as big and transparent as possible by reducing the main transparency losses that are secondary phases, light scattering by porosity and for birefringent ceramics, light scattering at grain boundaries.

67

Methods

To fabricate transparent alumina the global process has been studied. At first, a step of slurry doping has been optimized with two different slurries (S1 and S2) and two dopants (zirconium and lanthanum). Then two shaping method have been tested: freeze drying or slip casting. The more appropriate shape process was the slip casting. To finish a flash sintering step is investigated. The optimized SPS sintering cycle depends of the properties of green body sample. A dilatometric SPS experiment has been done to determine the best sintering temperature of the green body, and then a specific cycle is realized. The objective in the case of alumina is to get a fully densify sample with a limited grain growth.

In the case of transparent spinel, the material is fabricated with granulated commercial powders, shaping and sintering in the SPS. Contrary to alumina, grain size in spinel is not a limiting factor to transparency. Three different granulated powders has been tested. Processing parameters which allow to obtain small (20 mm

_____

diameter) transparent samples will be presented. Then, the impact of stress heterogeneity of uniaxial pressing and temperature heterogeneity between the center and the edges of the sample in case of large sample diameter (40mm) will be studied. For both, the transparency (Real In Line Transmission, RIT) is measured with a spectrophotometer.

Results and discussion

In case of alumina, several parameters have been studied. First, two slurries S1 and S2 have been tested (different particle distribution size) with two dopants: zirconium and lanthanum. Both reduce the diffusion across grain boundary, and the grain boundary solubility limit is between 280 and 570 ppm for zirconium and between 200 and 310 ppm for lanthanum. Secondary phases have been observed at 310ppm in case of lanthanum and at 570 ppm in case of zirconium. However, with lanthanum doping, the densification is better and the alumina grain size is smaller than with zirconium doping. Therefore, lanthanum was selected for the rest of the processing. For the shaping step, the more appropriate shape process was the slip casting. It allows to obtain denser green body with of smaller size pore population. The optimized SPS sintering cycle depends of the properties of green body sample. A *dilatometric SPS* experiment has been done to determine the best sintering temperature T_f of the green body, and then a specific cycle is realized (as presented in the works of Kim and Morita) (cf. figure 1). The objective in the case of alumina is to get a fully densify sample with a limited grain growth. An alumina sample (thickness 0.88mm) with a RIT superior to 70% at 640 nm is obtained with the optimized process [1] (cf. figure 2 and 3).

68
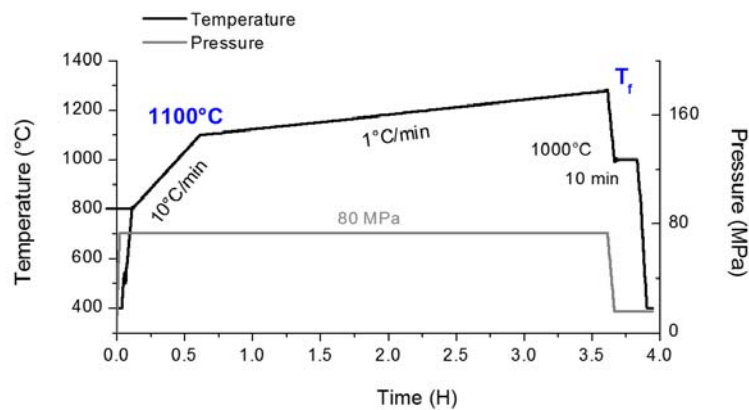
Fig. 1. Classical SPS cycle for birefringent ceramic

Conclusions

Alumina samples (thickness 0.88mm) with a RIT superior to 70% are obtained with an optimized process: 120cat ppm of lanthanum doping, slip casting as shaping step and SPS sintering at 1140°C under 80MPa.

For transparent spinel, SPS is an effective sintering technique to prepare small samples (Ø 20mm). Samples with a 85% RIT for 1.85mm thickness have been fabricated. SPS is a more complicated sintering technique to prepare large samples due to sample heterogeneity, thermal gradient and stress gradient.
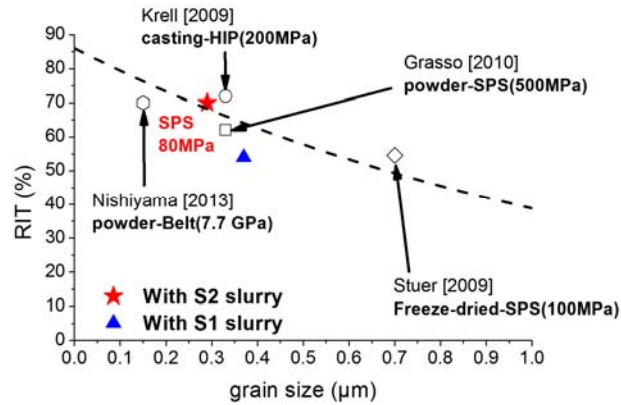
Fig. 2. Optical properties of samples elaborated via slip casting - SPS
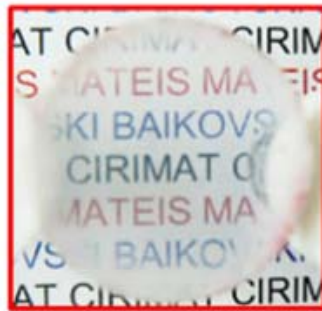
Fig. 3. Small alumina sample size (Ø 20mm Thickness 0.88mm) RIT > 70%

69

Fig. 4. Spinel sample RIT = 85% at 500 nm for 1.85 mm thickness

References

[1] Roussel N., Lallemant .L et al., J. Am. Ceram. Soc., (2013), 1 - 4.
[2] Bonnefont et al., Cer. Int. 38 (2012) 131–140

_____

Influence of molar composition and sintering conditions on Ti-Al-C/Ti-Al-N MAX phases synthesized by SPS

S. Signe Goumwe[1], M. Gonon[1], J-P Erauw[2], P. Aubry[2], V. Dupont[2]

[1] *Materials Science, University of Mons, Rue de l'Epargne 56, 7000 Mons, Belgium,* stella.signegoumwe@umons.ac.be
[2] *CRIBC, Avenue du Gouverneur Emile Cornez 4, 7000 Mons, Belgium*

Abstract

In the present work, synthesis of Ti_2AlN MAX phase by Spark Plasma Sintering (SPS) of TiN/Al/Ti powder mixture with a ratio of 1:1:1 under different sintering conditions is investigated. The phase quantitative analysis and microstructural characterization (anisotropy and grain size) are performed by X-Ray Diffraction coupled with Rietveld analysis. For all sintering conditions tested, Ti_2AlN is the main MAX phase obtained, TiN, AlTi and $AlTi_3$ were also identified as secondary phases. Phase weight fractions and microstructure of the obtained products strongly depend on the sintering temperature and the applied pressure during synthesis but weakly depend on the heating rate. The highest purity product ($\sim$ 80% Ti_2AlN) is obtained for SPS at 1300°C for 15 min under a pressure of 30 MPa.

Keywords

Ti_2AlN MAX phase, Rietveld analysis, Spark Plasma Sintering

Introduction

Ti_2AlN (Fig. 1) belongs to a new class of layered ternary ceramics called "MAX phases" (where n is 1, 2 or 3, M is an early transition metal, A is an A-group element and X is either C or N). It exhibits like others MAX phases, unusual properties that combine both those of metals and ceramics due to its metallic/covalent atomic bonding and its layered structure. For example, as metals, Ti_2AlN presents a low hardness, high electrical and thermal conductivity, a good machinability. Simultaneously, like ceramics it has a relatively low density, a high elastic modulus and a significant plasticity at high temperature [1]. Therefore, Ti_2AlN can be a suitable candidate for high temperature and structural applications [1].

In terms of bulk Ti_2AlN processing, the most commonly used technic is hot pressing of corresponding stoichiometric elemental and/or binary ceramic powder [2, 3]. However, this technic required relatively high temperature, pressure and long sintering duration. Consequently, Spark Plasma Sintering (Fig. 1) which is a fast sintering process (high heating rate up to 1000°C/min) using simultaneous application of electric pulsed current and uniaxial pressure during sintering appears to be a good alternative for obtaining MAX phases [1, 4]. Moreover, SPS allow to obtain high purity and dense bulk materials with fine microstructure [2, 4].

Therefore, the aim of this work is to investigate the suitable SPS sintering conditions (temperature, heating rate and applied pressure) for obtaining Ti_2AlN.

_____
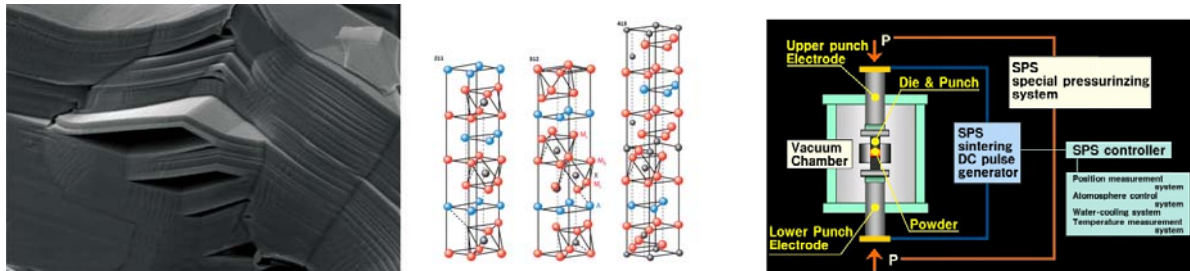
Fig. 1. Micrograph of layered MAX phase [5] and principle of SPS

Results and discussion

Ti₂AlN MAX phase elaboration

Powders mixtures of TiN, Al and Ti, with molar ratio of 1:1:1 are mixed in a glove box (to prevent oxidation) and inserted into a graphite mold of the SPS equipment for sintering. Sintered samples are 20 mm in diameter and about 4 mm of thick (see fig. 2). All tested sintering conditions are resumed in the table 1.

Table 1. SPS conditions tested

TiN : Al : Ti	Sintering temp. (°C)	Heating rate(°C/min)	Holding time (min)	Pressure (MPa)
	1200, 1250	100	15	15
1 :1 :1	1300, 1350	50/25*		30
	1400	25		60

(*)=50°C/min until 1000°C and 25°C/min from 1000°C to sintering temperature

Fig. 2. Sintered Ti₂AlN MAX phases samples

71

Characterization procedure

The crystalline phases are characterized by X-Ray Diffraction (D5000, Siemens Cu Kα,). Rietveld analysis applied to XRD patterns using MAUD software allows quantitative phase analysis and crystallite size measurement. Its principle is to minimized by least square method the residual function R between XRD experimental pattern (I) and calculated profile (I^{cal}): $R = \sum w_i (I_i - I_i^{calc})^2$

$$I_i^{calc} = S_F \sum_{j=1}^{N} S_j \sum_{k=1}^{N} m_{k,j} |F_{k,j}|^2 G_j(2\theta_i - 2\theta_{k,j}) P_{k,j} A_j L_k + bkg_i(2\theta)$$

As MAX phases are layered crystals, they give rise to preferred orientation of lamellar crystallites in the materials. So, crystal texture is evaluated through calculation of the P_{kj} factor (in "mrd" unity, "multiple of random density"). In this work the P factor is calculated for (00l) lattice planes (planes parallels to surface pressed) using Standard function model (implemented into MAUD software). P_{kl} factor correspond to the maximal intensity of the (00l) pole figure generated by this model.

Obtained phases

For all samples, XRD patterns show Ti₂AlN MAX phase as the major phase with small amount of TiN and intermetallic phases as secondary phases. As example, Fig.

3 shows the XRD pattern of sample sintered at 1200°C for 15min at 100°C/min under an applied pressure of 15 MPa. It indicates the formation of Ti_2AlN, TiN, AlTi and $AlTi_3$.
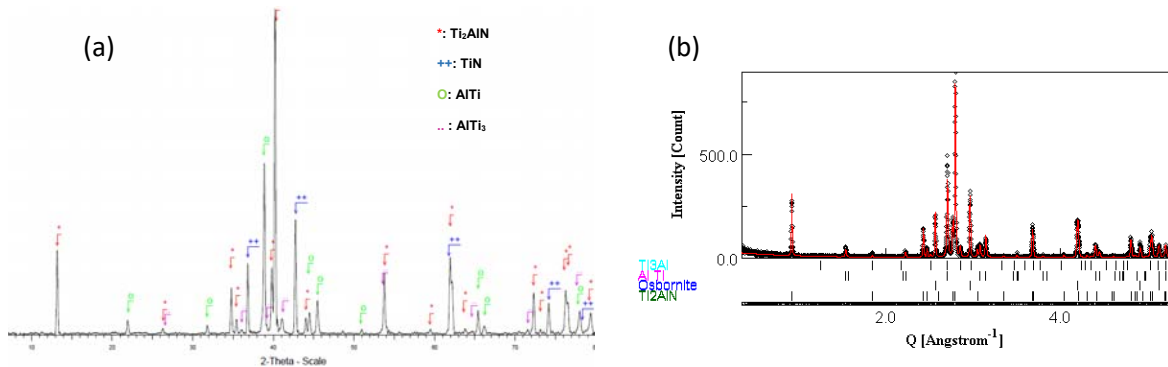
Fig. 3. (a) XRD pattern of sample sintered at 1200°C for 15 min at 100°C/min under 15 MPa; (b) graph of the corresponding Rietveld refinement

Heating rate and maximum temperature effects

Weight fractions, P_{00l} factor and Ti_2AlN crystallites size as function of temperature for different heating rate (between 100 and 25°C/min) under an applied load of 15 MPa, are shown in figure 4. It evidence that, whatever the heating rate, the amount of Ti_2AlN and the preferential orientation of the crystallites increase with the increase in temperature. In parallel, the amounts of the secondary phases (TiN, AlTi and $AlTi_3$) decrease (see table 2 for 100°C/min). This probably means that Ti_2AlN is formed through reaction between intermetallic phases and TiN. The increase of P_{00l} is probabily due to the increase of amount of lamelar crystallites. However, the trend for the crystallites size is not very clear particularly for the sample sintered at 25°C/min.

72
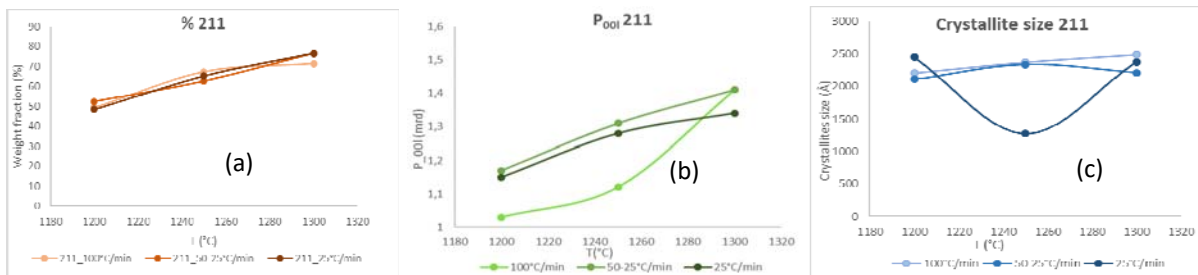
Fig. 4. Changes of (a) Weight fraction; (b) P00l factor; (c) crystallite size of Ti_2AlN with temperature

Table 2. Weight fractions of secondary phases at 100°C/min

H.R (°C/min)	T (°C)	P (MPa)	%211	%TiN	%AlTi	%AlTi₃
100	1300	15	71.5	12.1	16.4	0
		30	81.7	10.9	8.4	0
		60	76.9	12	11.1	0
	1250	15	64.4	14.4	18.2	0
	1200	15	49.4	21.7	25.5	3.3
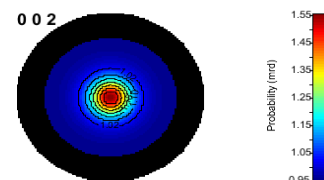
Fig. 5. (002) Pole figure of Ti_2AlN sample synthesized at 1300°C (1000C/min + 60MPa)

The heating rate does not strongly affect percentage and the microstructure of the obtained phases: except as mentioned, crystallite size at 25°C/min.

Applied pressure effects

For microstructural parameters, the increase of the pressure lead to a slight increase in the (00l) orientation of crystallite while the crystallite size remain almost constant (see fig.5 for samples sintered at 1300°C at 100°C/min). This probably means that applying pressure while sintering slightly directs crystals growth in the sample.
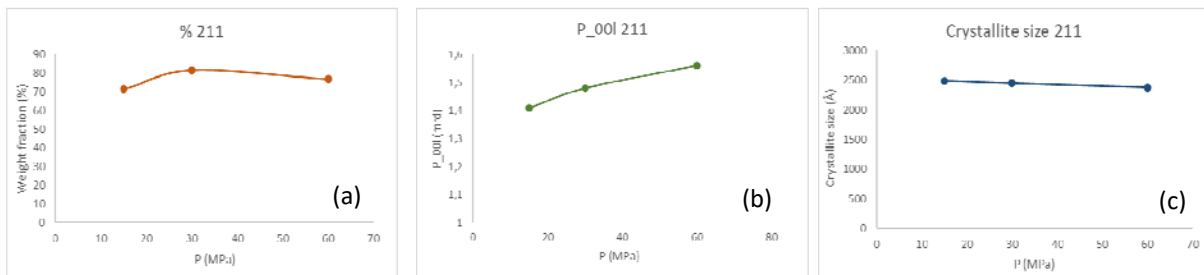
Fig. 6. Changes of (a) Weight fraction; (b) P00l factor; (c) crystallite size of Ti$_2$AlN with pressure

In terms of weight fractions (Fig. 6), the amount of Ti$_2$AlN reach a maximum for a pressure of 30 MPa and decrease after for higher values. We may assume that there no need to applied too high pressure for obtaining optimal amount of Ti$_2$AlN. Highest purity Ti$_2$AlN (~ 80%) was obtained for SPS at 1300°C for 15 min under 30 MPa.

73

Conclusions

Effects of SPS sintering conditions on the composition and microstructural characteriscs of Ti$_2$AlN MAX phase samples have been investigated. This work demonstrate the weak influence of the heating rate. On the opposite high temperature enhance the formation of Ti$_2$AlN. Applied pressure both influence the Ti$_2$AlN fraction (optimum for 30 MPa) and enhance the crystallites orientation. Notice that this crystallites orientation remains weak whatever the SPS applied conditions.

Acknowledgements

References

[1] Yi Liu *et al*., "Reactive consolidation of layered-ternary Ti2AlN ceramics by spark plasma sintering of a Ti/AlN powder mixture", Journal of the European Ceramic Society 31 (2011) 863–868.

[2] Bai Cui *et al*., "Microstructural evolution during high-temperature oxidation of spark plasma sintered Ti2AlN ceramics", Acta Materialia 60 (2012) 1079–1092

[3] C. Tang *et al*., "Synthesis and characterization of Ti2AlC coatings by magnetron sputtering from three elemental targets and ex-situ annealing", Surface & Coatings Technology 309 (2017) 445–455

[4] Guk-hyun Jeong *et al*., "MAX-phase Ti2AlC ceramics: syntheses, properties and feasibility of applications in micro electrical discharge machining", Journal of Ceramic Processing Research. Vol. 17, No. 10, pp. 1116~1122 (2016)

[5] W. Barsoum *et al*.: Ann. Rev. Mater. Res. 2011. 41:195–227

_____

Elaboration and impregnation of highly porous architectured ceramic matrix

L. Tabard[1], E. Prud'Homme[1], V. Garnier[1], L. Gremillard[1], Y. Jorand[1]

[1] MATEIS, INSA Lyon, 7 av. Jean Capelle, Villeurbanne, France, lucie.tabard@insa-lyon.fr

Abstract

The aim of this work was to fabricate composites for thermo-chemical energy storage for buildings application. Such composites are made of a ceramic host matrix and a hygroscopic salt of high-energy potential. Additive manufacturing was chosen to design the host architectural matrix (Al_2O_3; or ZrO_2 with or without porogen), that presents a high specific surface area.

Keywords

Additive manufacturing; porogen; inter-seasonal heat storage; hygroscopic salt

Introduction

Nowadays, the biggest challenge to reduce fossil fuel consumption is to find an alternative to provide heating requirements for buildings. Inter-seasonal heat storage seems to be the best option considered. Among the potential materials, that is to say showing reversible endothermic/exothermic reaction, hygroscopic salts are the best candidates. Indeed, by reversible hydration reaction they can exchange large quantity of heat.

74

Previous work on reactor based on hydration of hygroscopic salt by humid airflow reports a major technical issue: when hydrated, the salt irreversibly agglomerate, thus resulting in drastic loss of performances [C. Finck].

Our work is based on the hypothesis that spreading and attaching the salt on an inert and porous matrix would avoid its agglomeration. Nevertheless, the specific available surface area has to be maximal to aim the target of $300kWh/m^3$, fixed by DECARTH ANR project (*Development and characterization of high-energy dense composite architectures for the conception of thermo-chemical energy storage*), within which this work partakes place. To combine spreading, hydration, and high specific surface area, we thought of an architectured host matrix to ensure a high surface exchange between humid air and salt (figure 1).

This study focuses on the fabrication of a host matrix that develops high accessible specific area at macro and micro-scale; and on the verification of the salt bonding with the host ceramic matrix.
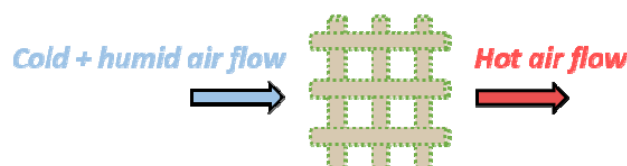

Fig. 1. Diagram of architectured matrix

_____

Methods

We designed the host matrix in scaffold shape and fabricated it by additive manufacturing with Robocasting to obtain high available specific area. Robocasting is a micro-extrusion technique that allows fabrication of complex shapes by extrusion of a printing paste. We compared two matrices materials to verify the salt bonding on the host matrix: zirconia and alumina. We choose zirconia for its good mechanical properties and both alumina and zirconia for their wide knowledge in additive manufacturing field. We also investigated the addition of porogen in printing paste in order to control various levels of porosity.

Printable pastes

We prepared three printable pastes. Alumina and zirconia pastes were formulated with 39 vol% of powder (Alumina, ceralox APA 0.5 µm, or zirconia Daiichi Ce-Z12 0.5µm) dispersed in an hydrogel (25 wt% pluronic PF127 in water). 0.5 wt% of Darvan 811 was added in the formulation as dispersant agent. 39 vol% paste with porogen was prepared with zirconia powder and wheat starch as porogen (VWR) in 60 vol%/(zrO$_2$ vol) in order to create interconnected porosity [E. Juste]. We homogenized the pastes in a planetary centrifugal mixer (Speedmixer) at 2000 rpm/mn for 10 mn. For each paste, we printed scaffolds of 10x10x5 mm^3 with 90° orientation and an offset in X and Y between each layer. The offset in X and Y between each layer aims at forcing the airflow of the future reactor to go through all the structure. We printed scaffolds with tips of 410 µm in inner diameter, and an interpenetration of 16% of the tip diameter between layers. We printed under controlled atmosphere: high humidity (98 %HR) and 25°C to inhibit paste drying or tips clogging during printing.

Post- Process

The printed samples were then dried in a climatic chamber during four days to slowly decrease the humidity rate from 98 %HR to 35 %HR. Once dried, the samples were debinded at 2°C/mn up to 500°C; samples containing wheat starch were slowly debinded (0.5 °C/mn up to 200; 2°C/mn up to 600°C). Finally, samples were partially sintered. We choose the temperature of partial sintering based on Thermo Mechanical Analysis (TMA) results in order to stop the sintering right after the consolidation step and right before the full densification step. Zirconia samples were sintered at 1250°C; alumina samples were sintered at 1330°C, with the same cycle (6°C/mn up to 800°C; 5°C/mn up to 1000°C; 3°C/mn up to 1250 or 1330°C).

Composite Fabrication

We fabricated the composite ceramic matrix/salt by impregnation. We prepared a saturated solution of MgSO$_4$,7H$_2$O at 710g.L^{-1} in which we plunged the scaffolds for 10mn. After the impregnation, we removed the samples to dry them in a climatic chamber at 150°C to remove water and recrystallize the monohydrate MgSO$_4$,H$_2$O [L.Okrhimenko].

Composite characterization

The scaffold architecture was characterized by x-ray tomography and Archimedes density. We evaluated the scaffold microstructure by SEM and local x-rays

tomography at a filament scale. We measured the porosity rate and the pores size range with mercury porosimetry.

We verified the salt bonding on the ceramic matrix surface with SEM and EDX.

Results and discussion

Microstructure

Results shows the fabrication of highly porous scaffolds, both on macro-scale thanks to the open channels of the matrix structure and on micro-scale due to the partial sintering and the addition of wheat starch as porogen.

Partial sintering for both alumina and zirconia scaffold leads to a filament with open porosity of 48%, with mono-modal pore distribution of 0.1 μm.

Addition of wheat starch combined with partial sintering leads to scaffolds with 78% of porosity, with bi-modal pore size distribution of 0.1μm and 1 to 92 μm, measured by mercury porosimetry. Pores created by wheat starch are indeed interconnected, as revealed by mercury porosimetry analysis and local X-rays tomography. Indeed, scans at 0.7 μm and further 3D image analysis with Fiji shows the interconnection of this family of pores. Interconnection of around 85% of the pores was measured with Fiji, figure 2.a. Moreover, Fiji analysis shows the alignment of pores in the length of the filament, that is to say the printing direction. SEM observation shows that pore created by wheat starch are ear-like shaped (figure 2.b (zoom window)).
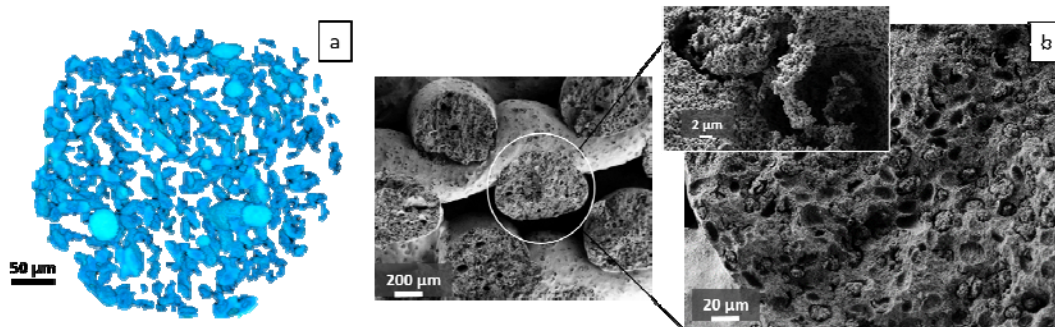
Fig. 2. a. Local x-rays tomography of interconnected pores (in blue) created by wheat starch ; b. Scaffold microstructure with pores created by wheat starh

Composite salt/host ceramic

SEM characterization showed that roughness induced by partial sintering promotes salt bonding. However, the recrystallization of the salt is different depending on the host material. $MgSO_4,H_2O$ crystallizes as big cracked layers of 2 to 10 μm in width on alumina surface (figure 3.a), whereas it crystallizes in a multitude of isolated small grains from 2 to 8 μm on zirconia surface (figure 3.b). Zirconia particle are round, whereas alumina particles are more angular, thus channels created by partial sintering show different shape. Consequently, during drying cycle, water is removed under different paths from the saturated salt solution, thus explaining the different bonding. Paths induced by porosity created by starch lead to deepest impregnation

of the salt in the filament. In-situ reactor testing of the performances of the composite will help conclude on the best composite type.
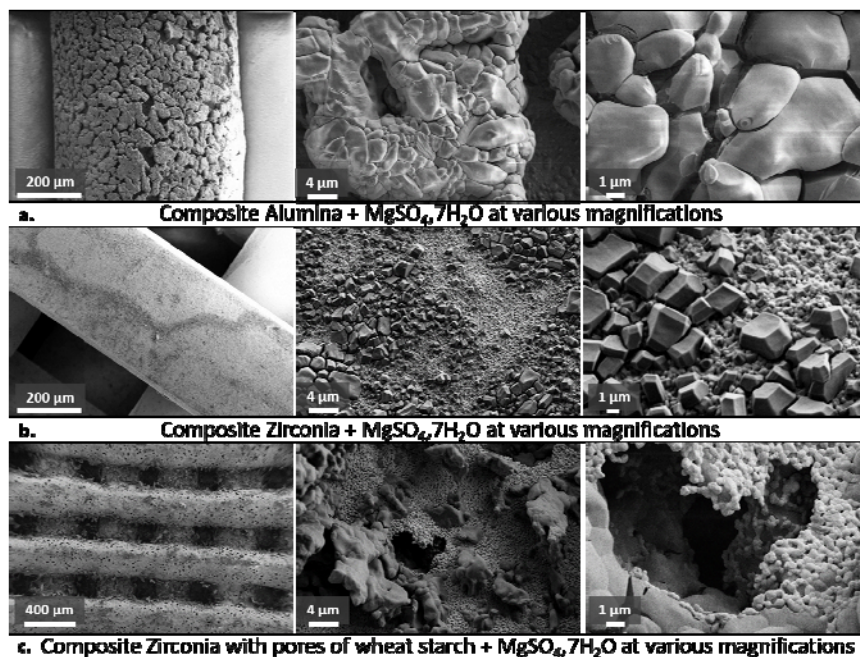
Fig. 3. Fabricated Salt/Ceramic matrix composites

Conclusions

In conclusion, architectural ceramic matrix with different level of controlled porosity were fabricated with additive manufacturing. Impregnation of such matrix with hygroscopic salt leads to the fabrication of a potentially high energy composite. Such composite could be used for thermo-chemical energy storage for buildings.

Mechanical properties are currently investigated, showing resistance up to 2 MPa in spite of the high porosity rate of the samples (between 50 and 80%). Permeability as well as in-situ reactor test of performances should be investigated.

Acknowledgements

References

[C.Finck] C. Finck *and al.*, "Experimental results of a 3 kWh thermochemical heat storage module for space heating application," *Energy Procedia*, vol. 48

[E. Juste] E. Juste, PhD thesis, Limoges university, 2007, « Elaboration d'une membrane de réacteur catalytique pour la production de gaz de synthèse »

[L. Okrhimenko] L. Okrhimenko, PhD thesis, Lyon university, 2018, "Stockage d'énergie thermique par un composite zéolite / $MgSO_4$: étude thermocinétique du système $MgSO_4–H_2O$ et étude expérimentale des composites"

Flexural strength and X-ray computed tomography analysis of zirconia specimens processed by additive manufacturing

F. Khaldoun[1], M. Saâdaoui[1], J. Adrien[2], H. Reveron[2], J. Chevalier[2]

[1]*Université Mohamed V de Rabat, EMI, LERSIM, Avenue Ibn Sina, 10000 Rabat, Morocco*
[2]*Université de Lyon, INSA de Lyon, MATEIS CNRS UMR5510, 20 Avenue Albert Einstein, F-69621 Villeurbanne Cedex, France*

Abstract

Typical defects in Y-TZP zirconia with two different architectures processed by the Lithography-based Ceramic Manufacturing (LCM) technique were identified using X- ray computed tomography (CT). Potential critical defects were detected and used to determine a CT derived strength, which showed a good correlation with direct strength measurements.

Keywords

Additive manufacturing, strength, X-ray tomography, zirconia

Introduction

Additive manufacturing (AM) or 3D printing is a process which enables to produce an object by adding materiel layer-by-layer from a 3D model. This technology is getting developed for ceramic materials to avoid expensive machining and to obtain complex shapes with fewer steps than conventional manufacturing methods. Different techniques have been used among which are direct ink-jet printing (DIP), selective laser sintering (SLS) and stereolithography (SLA) [1, 2]. The last has been adapted by Lithoz GmbH (Vienna, Austria) to the Lithography-based Ceramic Manufacturing (LCM) technology [3]. However, few works have been done on the reliability of AM of ceramic materials and its impact on their mechanical properties. In particular, characterization of the microstructure and the defects inherent to each AM technique is crucial for material optimization.

In this work, X-ray computed tomography (CT), which allows to obtain 3D information of materials microstructure [4], was used to identify typical flaws in Y-TZP zirconia with two types of architectures manufactured using the LCM technology. Systematic CT analysis was carried out before fracture to investigate typical defects generated in the studied materials and their correlation to the bending strengths.

Materials and Methods

3Y-TZP samples made by Lithoz Gmbh, using the LCM method were tested. The procedure is identical to that described in [3] with only a different bender system. The specimens were received as rectangular bars (2.5 mm x 2.2 mm x 25 mm) with

78

two different layer architectures produced by upright (U) or horizontal (H) building (Fig. 1).
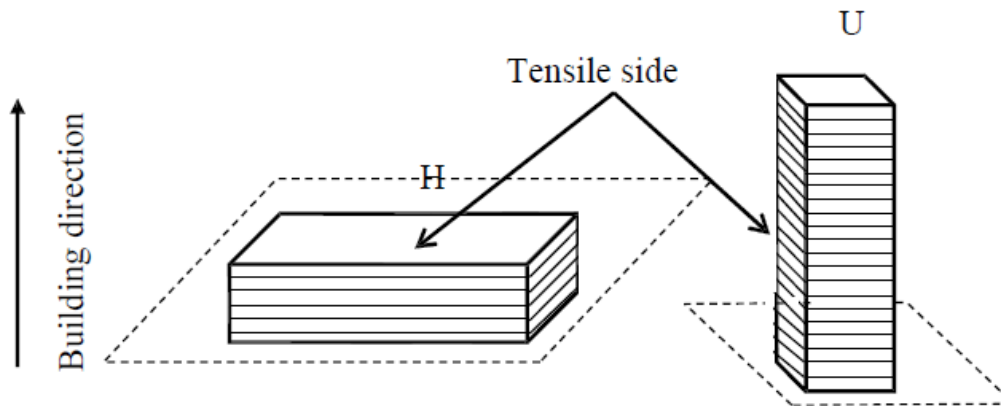
Fig. 1. Illustration of the layer architectures.

X-ray computed tomography was carried out before fracture and CT Scans were generated with a resolution of 2 μm at the center of the samples, over a total length of 10 mm. The analysis was performed using a commercial software.
The fracture strength of the as received samples was measured by three points bending tests (span of 20 mm). Before the bending experiment, all the samples were chamfered on the tensile side.

Results and discussion
The mean values of the measured strength are of 908 ± 86 MPa and 790 ± 149 MPa and the Weibull modulus of 12.6 and 6.24 respectively for U and H samples. The low value of the Weibull modulus for H samples reflects the large flow dispersion in this architecture, in accordance with the work of Harrer et al. [3]. Fig. 2 shows examples of cross-sectional CT-images and planar projections for H and U samples. Fig. 2a illustrates typical defects detected by CT analysis next to the tensile side of the samples: pores (P), surface defects (S) and agglomerates (A). Pores are present in both architectures and they are concentrated in plans near the building platform or within a central channel perpendicular to the layers for H samples (Fig. 2b). This can be attributed to trapped air bubbles formed due to the high viscosity of the slurry and that couldn't be eliminated due to the low building height for this architecture (2.2 mm). The agglomerates which correspond to under densified zones were detected in a greater proportion in U samples and are in the form of circular discs parallel to the layers that could be observed by scrolling through the slice projections. They are not visible on the planar projections as they don't provide sufficient contrast compared to pores. Large surface defects (Fig. 2a) are typical of H samples and could explain the lower values of the strength and the Weibull modulus for this architecture. They result from the removing of the

79

specimens from the building platform, as the lower layer (in contact with the platform in the LCM process) has not been removed for this study.

The investigation of the scanned volumes before fracture allowed to detect potential critical defects in the tensile area of 10 samples of each architecture. As the samples were chamfered, potential critical defects were rarely detected at the edges. For H architecture, almost all the investigated samples presented surface potential critical defects with a size between 13 and 85 µm. For H samples, the flows that could potentially initiate the fracture were essentially agglomerates. From the size of the potential critical defects detected by CT analysis, a CT-derived strength, $_{CT-f}$, was determined using the Griffith criterion.
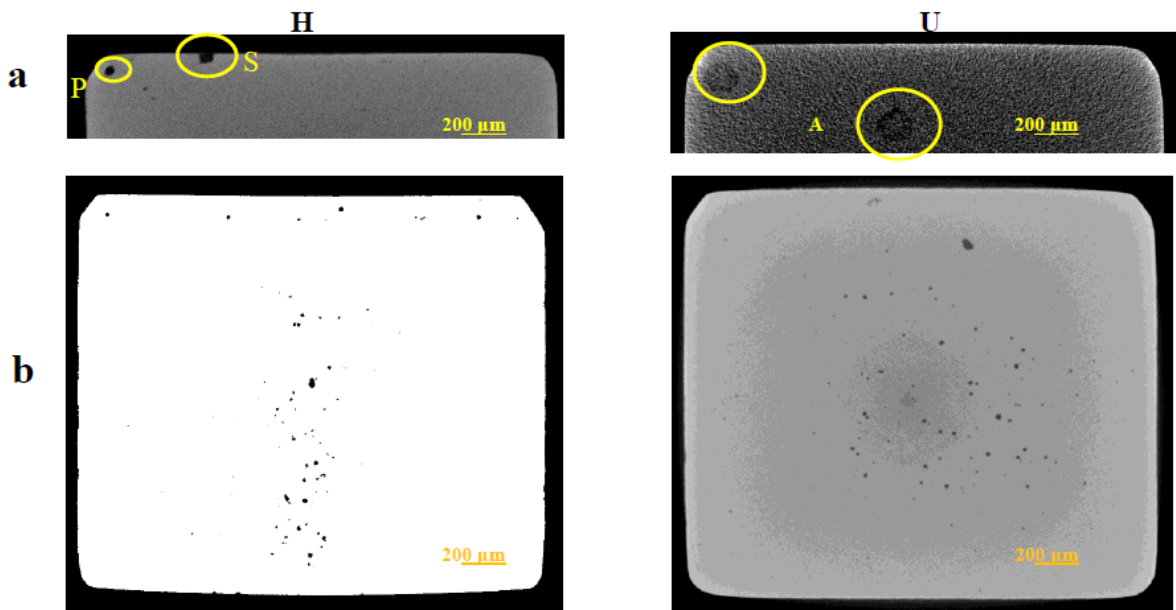
Fig. 2. Examples of flaws detected on cross sections (a): (pores (P), surface defects (S) and agglomerates (A)) and (b) plane projection showing the pore repartition.

A good correlation (Fig. 3) was obtained between $_{CT-f}$ and the effective strength at the location of the detected defect, $_{eff}$, calculated from the apparent measured strength and taking into account the linear decrease of the stress in 3-point bending configuration. These results indicate that X- ray CT analysis is relevant to characterize the defects in AM dense ceramics in order to monitor and optimize their manufacturing process.

Conclusions

This study shows that the non-destructive X-ray CT is relevant to characterize the defects in AM dense ceramics in order to monitor and optimize their manufacturing process. It allowed the identification of potential critical defects in Y-TZP zirconia, with a good correlation with bending strength measurements.

80
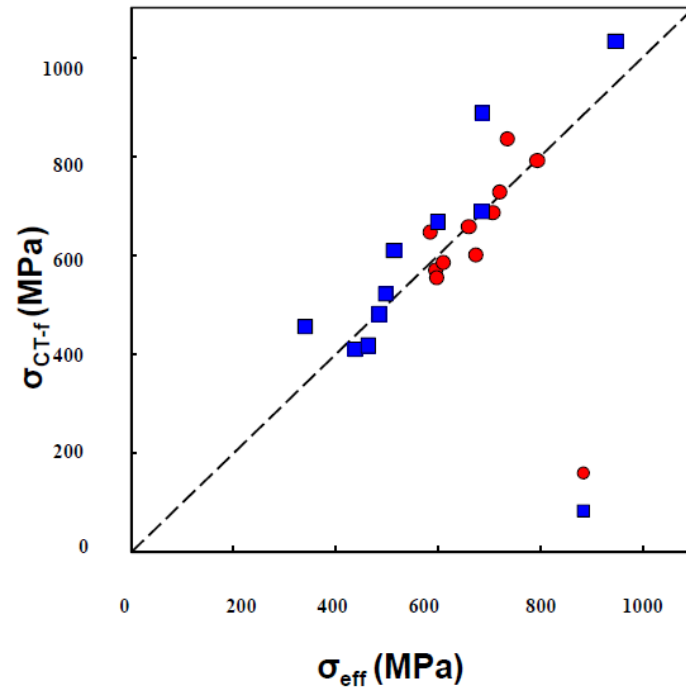
Fig. 3. Comparison between the CT derived and the effective strengths.

References

[1] S. Singh, S. Ramakrishna, R. Singh, Material issues in additive manufacturing: A review, J. Manuf. Process. 25 (2017) 185-200.

[2] J. Gardan, Additive manufacturing technologies: state of the art and trends, Int. J. Prod. Res. 54 (2015) 3118-3132.

[3] W. Harrer, M. Schwentenwein, T. Lube, R. Danzer, Fractography of zirconia-specimens made using additive manufacturing (LCM) technology, J. Eur. Ceram. Soc. 37 (2017) 4331-4338.

[4] E. Maire, P. Colombo, J. Adrien, L. Babout, L. Biasetto, Characterisation of the morphology of porous ceramics by 3D image processing of X-ray tomography data, J. Eur. Ceram. Soc. 27 (2007) 1973-1981

Functional ion doping of mesoporous zirconia structures for biomedical applications

F. Tana[1], A. Serafini, E. De Giglio, S. Cometa[3], R. Chiesa[1], L. De Nardo[1]

[1] *Department of Chemistry, Materials and Chemical Engineering "G. Natta". Politecnico di Milano, Via Mancinelli 7, 20131 Milano, Italy* francesca.tana@polimi.it, andrea.serafini@polimi.it, roberto.chiesa@polimi.it, luigi.denardo@polimi.it

[2] *Department of Chemistry, Università di Bari Aldo Moro, Via E. Orabona 4, 70125 Bari, Italy* elvira.degiglio@uniba.it

[3.] *Jaber Innovation srl, Via Calcutta 8, 00100 Roma, Italy* stefania.cometa@jaber.it

Abstract

In this work, we investigated the effects of ion doping (Ga^{3+} and Ca^{2+}) in zirconia mesoporous coatings intended for biomedical applications. ZrO_2 coatings were prepared via evaporation induced self-assembling of solutions containing a sacrificial soft template agent (Pluronic F127) and metal salts precursor ($ZrCl_4$). Given amount of either calcium or gallium nitrate precursor (from 5 up to 25%mol) were added to prepare ion-doped structures. A thermal treatment was then performed to remove the template at increasing temperature (400-600 °C).

An ordered array of pores, showing a size between 5-10 nm in diameter, was observed by TEM, both for pure and ion-doped ZrO_2 surfaces. X-ray diffraction, combined with TEM, revealed that the introduction of ions played a major role as metastable tetragonal phase stabilizer, further increasing thermal resistance of the mesoporous structure. The ions content and their release were confirmed by XPS and ICP analyses. The non-toxicity of coatings was assessed by citocompatibility test *in vitro*.

Keywords

Ion-doped zirconia, mesoporous zirconia coatings, surface modification

Introduction

A large body of literature is devoted to the investigation of the interaction mechanisms occurring between the biological environment and implanted material interfaces. Surface area and roughness were reported to enhance the cell-material interactions improving the final biological outcome (e.g. osseointegration) of implanted devices [1,2]. Zirconia (ZrO_2) has been widely used in biomedical applications (mainly for orthopedic restorations) due to its mechanical reliability and non-toxicity. Because of its opacity and similarity with natural teeth, zirconia has been further used in dentistry, and fully zirconia abutments have been recently used, showing advantages in overcoming allergic reaction towards metallic components. Nevertheless, in order to improve the outcome of zirconia implants while maintaining satisfactory mechanical performance, the modification through surface treatments, as

82

acid etching or sandblasting [3,4], and the deposition of surface coatings, as bioactive glass [5], has been recently exploited.

The combination of sol–gel processes and self-assembly techniques represents an effective bottom-up synthesis of complex tailor-made nanostructured inorganic materials, as membrane or filters [6].

In this work, the formation of mesoporous ZrO_2 surfaces, exploiting the evaporation induced self-assembly of a precursor sol-gel solution containing a template agent, was investigated. Zirconia structure was doped with functional ions selected for their relevant biological functions, such as calcium for protein binding and biomineralization [7,8], or gallium, as inhibitor of bacterial activity. Moreover, the creation of spatially ordered arrays of nanocavities offer an increased surface area that potentially enhance final cellular and tissue responses.

Ion doping was further intended to improve the performances of pristine ZrO_2 substrate, stabilizing the porous network and metastable phases alongside.

Results and discussion

TEM micrographs revealed an ordered array of pores, showing a size between 5-10 nm in diameter, the same architecture being observed in pristine ZrO_2 and doped samples calcined at 400 °C (Figure 1). Of note, as the calcination temperature increased up to 600 °C, small crystals formed in pure zirconia samples, while still ordered mesoporous framework was observed in doped samples (Figure 1). The collapse of the organized inorganic network was attributed to the transition from the amorphous to the crystalline phase in calcined samples and moreover, to the bigger dimensions of crystallites in un-doped zirconia compared with the Ca-doped and Ga-doped samples. Differences in crystalline growth for doped and un-doped zirconia were previously reported [9].

TEM results were supported by XRD measurements on samples calcined at 400-600 °C, which show an evolution of the crystalline structure by increasing calcination temperature, thus inducing morphological changes in the porous architecture. For samples treated at 400 °C, a broad diffraction peak was observed, indicating that at this stage the oxide structure is only partially crystallized. By increasing the calcination temperature, instead of the thermodynamically stable monoclinic phase, the sharper peaks were associated with a tetragonal metastable phase (Figure 2). It is well known that zirconia is a polymorph that occurs in different crystalline phases depending on the environmental conditions. Nonetheless, the addition of stabilizing agents (e.g. divalent and trivalent cations such as Mg^{2+}, Ca^{2+}, and Y^{3+}) is usually exploited to stabilize metastable tetragonal phases in environmental conditions [10,11].

In vitro citocompatibility confirmed that both porous un-doped and doped zirconia surfaces support cell adhesion and proliferation. Cell lines representative of both soft and hard tissue were selected, depending on the final intended application. Osteoblasts-like SAOS-2 cells were tested for Ca-doped samples while human primary gingival fibroblasts and human osteoblasts progenitors were cultured on Ga-

83

_____

doped ones. All the experiments were run concurrently on un-doped ZrO_2 surfaces, as control. The adhering cells assumed a well-spread and elongated morphology on all surfaces. Changes in cell morphology from round to elongated shape normally occur when cells adhere onto substrates that promote their viability. With this regard, the pore size could play a relevant role in dictating interactions with biological environment [12]. An increased viability was observed on Ca-doped samples while the absence of toxic effect, even concerning the highest Ga amount, in Ga-doped surfaces was confirmed.

84
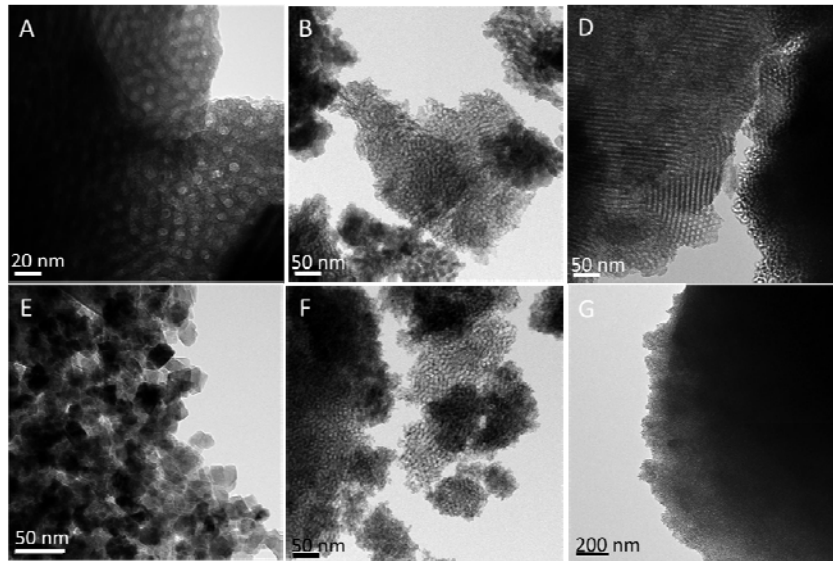
Fig. 1. Representative TEM micrographs of A) pure zirconia B) Ca- ZrO_2 and C) Ga- ZrO_2 mesoporous zirconia samples calcined at 400 °C. At the bottom the corresponding samples E), F), and G), calcined at 600 °C.
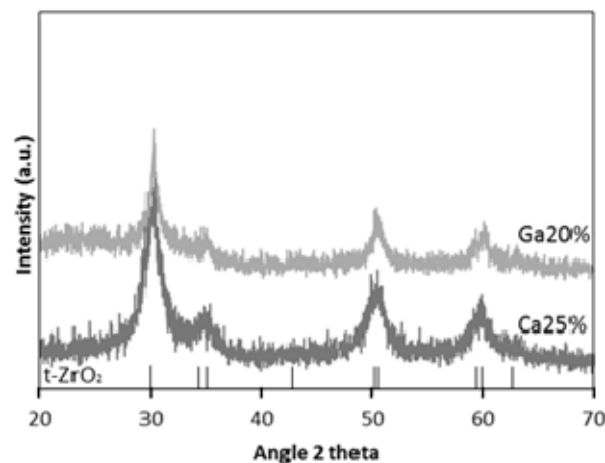
Fig. 2. Representative XRD spectra of Ca- and Ga- ZrO_2 powders calcined at 600 °C.

Conclusions

The introduction of doping ions was easily performed at different concentration via the deposition of a template sol-gel solution. A porous structure was successfully

_____

_____

obtained both for pure and doped surfaces. All samples were characterized concerning their physicochemical properties revealing the increased thermal resistance of doped mesoporous structures. *In vitro* biological assays revealed a non-toxic effect of Ga-doped surfaces and an increase cell viability in Ca-doped mesoporous ones. The obtained results were considered an effect of concurrent modification in surface patterning and chemistry.

Acknowledgements

References

[1] L. Tang, P. Thevenot, W. Hu, Surface chemistry influences implant biocompatibility, Current topics in medicinal chemistry. 8(4), (2008) 270-280.

[2] F. Variola, J. B. Brunski, G. Orsini, P. T. de Oliveira, R. Wazen, A Nanci, Nanoscale surface modifications of medically relevant metals: state-of-the art and perspectives. Nanoscale. 3(2), (2011) 335-353.

[3] H. Schliephake, T. Hefti, F. Schlottig, P. Gédet, H. Staedt, Mechanical anchorage and peri-implant bone formation of surface-modified zirconia in minipigs. J. Clin. Periodontol. 37(9), (2010) 818-828.

[4] O. Hoffmann, N. Angelov, G. G. Zafiropoulos, S. Andreana, Osseointegration of zirconia implants with different surface characteristics: an evaluation in rabbits. Int J Oral Maxillofac Implants. 27(2), (2012) 352-358.

[5] M. Araujo, M. Miola, A. Venturello, G. Baldi, J. Perez, E Verne, Glass coatings on zirconia with enhanced bioactivity. J. Eur. Ceram. Soc. 36(13), (2016) 3201-3210.

[6] G.J.A.A. Soler-Illia, O. Azzaroni, Multifunctional hybrids by combining ordered mesoporous materials and macromolecular building blocks, Chem. Soc. Rev. 40 (2011) 1107–1150.

[7] B. Feng, J. Chen, X. Zhang, Interaction of calcium and phosphate in apatite coating on titanium with serum albumin, Biomaterials. 23 (2002) 2499–2507.

[8] N.Y. Hou, J. Zhu, H. Zhang, H. Perinpanayagam, Ultrafine calcium–titania–polyester dry powder coatings promote human mesenchymal cell attachment and biomineralization, Surf. Coatings Technol. 251 (2014) 177–185.

[9] Q. Yuan, L. L. Li, S. L. Lu, H. H. Duan, Z. X. Li, Y. X. Zhu, C. H. Yan, Facile synthesis of Zr-based functional materials with highly ordered mesoporous structures, J. Phys. Chem. C. 113 (2009) 4117–4124.

[10] R.C. Garvie, The Cubic Field in the System CaO-ZrO$_2$, J. Am. Ceram. Soc. 51 (1968) 553–556.

[11] D.L. Porter, A.H. Heuer, Microstructural Development in MgO-Partially Stabilized Zirconia (Mg-PSZ), J. Am. Ceram. Soc. 62 (1979) 298–305.

[12] V.L. Chavez, L. Song, S. Barua, X. Li, Q. Wu, D. Zhao, K. Rege, B.D. Vogt, Impact of nanopore morphology on cell viability on mesoporous polymer and carbon surfaces, Acta Biomater. 6 (2010) 3035–3043.

85

Incorporating two-dimensional nanostructures as a second phase to a zirconia matrix

C. Muñoz-Ferreiro[1], R. Poyato[2], A. Morales-Rodríguez[1], Á. Gallardo-López[1]

[1] *Dpto. Física de la Materia Condensada, Universidad de Sevilla, Avda Reina Mercedes s/n, 41080 Sevilla, Spain*
[2] *Inst. Ciencia de Materiales de Sevilla (ICMS), CSIC – Universidad de Sevilla, Avda. Américo Vespucio 49, 41092 Sevilla, Spain*

Abstract

In this work, we have studied the incorporation of 1 and 4-5 vol% few layer graphene (FLG) and BN nano sheets (BNNS) in a zirconia (3YTZP) matrix. All composites were densified using electric pulsed discharge sintering (also known as spark plasma sintering, SPS) and the resulting microstructures have been analyzed. In order to assess the nano sheets integrity and their degree of dispersion in the matrix, we have used Raman spectroscopy and scanning electron microscopy, among other techniques. Mechanical properties, such as Vickers hardness, have also been tested and correlated to the microstructure.

Keywords

Few layered graphene (FLG); Boron nitride nanosheets (BNNS); zirconia composites; microstructure; hardness.

86

Introduction

Two-dimensional nanomaterials, among which graphene is the best known, are a new class of materials that have been attracting increasing attention because of their unique properties. The exceptional characteristics of these nanostructures have motivated their introduction as a second phase in advanced ceramic matrices in order to enhance their properties. Many works are being done on graphene based nanomaterials (GBN) / ceramic composites to overcome the inherent fragility of the matrix. Depending on the number of layers, dimensions and chemical modifications, different properties can be achieved [1]. Although some ameliorations have been achieved by introducing these nanostructures, an increase in electrical conductivity and fracture toughness with increasing graphene nanoplatelets (GNP) content [2], other properties, such as hardness, deteriorate above a certain threshold [3]. Therefore, further studies are needed.

More recently, other two-dimensional nanomaterials having an analogue structure to graphene (known as inorganic graphene analogues, IGA) are gaining relevance. Hence, some investigations have been carried out, and are still in development, to obtain those IGA out of layered materials, such as boron nitride (BN) [4]. Two-dimensional BN in the form of nanoplatelet (BNNP) or nanosheet (BNNS) has mechanical properties comparable to those of graphene - elastic modulus between 700 and 900 GPa [5] - and some advantages over it, such as its chemical stability up

to 950 ºC approximately. So, new functionalities can be achieved by incorporating these new nanostructures to ceramics and a comparison between them and graphene may be of great interest.

There are some works already made on ceramic composites with BN nanotubes (BNNT) which shows a better performance, regarding mechanical properties: flexural strength, fracture toughness or scratch resistance. However, only the external surface of BNNTs act as reinforcement whereas BNNPs, due to their 2D structure, would maximize the interfacial contact area. Despite the promising improvements on mechanical properties, few studies have been done on BNNP/ceramic composites up to date. Sun et al. have analyzed fused silica composites with BNNPs [6, 7] and found out 53% and 32% increasement in flexural resistance and fracture toughness, respectively, when incorporating 0.5 wt% BNNPs. This content is also a limit for the amelioration of mechanical properties, which was attributed to agglomeration problems according to these authors.

So one of the most difficult issues about the processing of composites incorporating two-dimensional nanostructures (GBNs and BNNPs) is to achieve a correct and homogeneous dispersion of the second phase through the ceramic matrix, due to result of their high tendency to agglomerate [6, 8].

In this work, we have prepared tetragonal zirconia (3YTZP) composites with 1 and 4-5 vol% BNNSs/FLGs. The nanostructures were dispersed by ultrasonication for 30 mins and then mixed with the ceramic. The microstructural characteristics of the SPSed composites were studied, such as density, homogeneity and integrity of the nanosheets, as well as some of their mechanical properties in order to elucidate the influence of the introduction of the second phase into the matrix.

Results and discussion

All the sintered composites achieved 99-100 % of the theoretical densities, except for the composite containing 5 vol% FLGs, as shown in Table 1, and showed similar homogeneities of their microstructure. Scanning electron micrographs of the fracture surfaces (fig. 1) showed that thin, small nanosheets from both materials were placed at 3YTZP grain boundaries, but as it can be seen in fig. 1 a), some agglomerates were also found.

Table 1. Experimental, theoretical and relative density of the studied composites.

Type of 2D nanomaterial	content (vol%)	Nomenclature	ϱ_{exp} (gcm^{-3})	ϱ_{th} (gcm^{-3})	$\varrho_{relative}$ (%)
FLG	1	1FLG	6.000±0.013	6.0115*	99.81±0.22
	5	5FLG	5.66±0.04	5.8575*	96.7±0.7
BNNS	1	1BNNS	5.96±0.04	6.0105*	99.1±0.6
	4	4BNNS	5.87±0.03	5.8920*	99.6±0.6

*The densities used for the calculation were 6,05 gcm^{-3}, 2,2 gcm^{-3} and 2,1 gcm^{-3} for 3YTZP, FLG and BNNS, respectively.

87

A decrease in the grain size of the ceramic matrix was found to take place when increasing the nanostructures content and there is also a difference in composites with different nanosheets, the introduction of FLGs inhibits grain growth more than BNNSs (Table 2). The Vickers hardness of the composites in plane (i.p.) and in the cross section (c.s.) shown in Table 2 relates to the anisotropy of the composites with FLGs. On the contrary, composites containing BNNS do not present mechanical anisotropy.

Table 2. Grain size and hardness of the studied composites.

Nomenclature	d_{planar} (μm)	s.d. (μm)	$H_{Vi.p.}$ (GPa)	$H_{Vc.s.}$ (GPa)
1FLG	0.24	0.12	12.8 ± 1.3	13.0 ± 1.1
5FLG	0.23	0.11	-*	9.9 ± 1.1
1BNNS	0.26	0.13	14.5 ± 2.0	14.1 ± 1.6
4BNNS	-**	-**	13.0 ± 2.0	13.2 ± 1.4

*Spaling impeded measuring
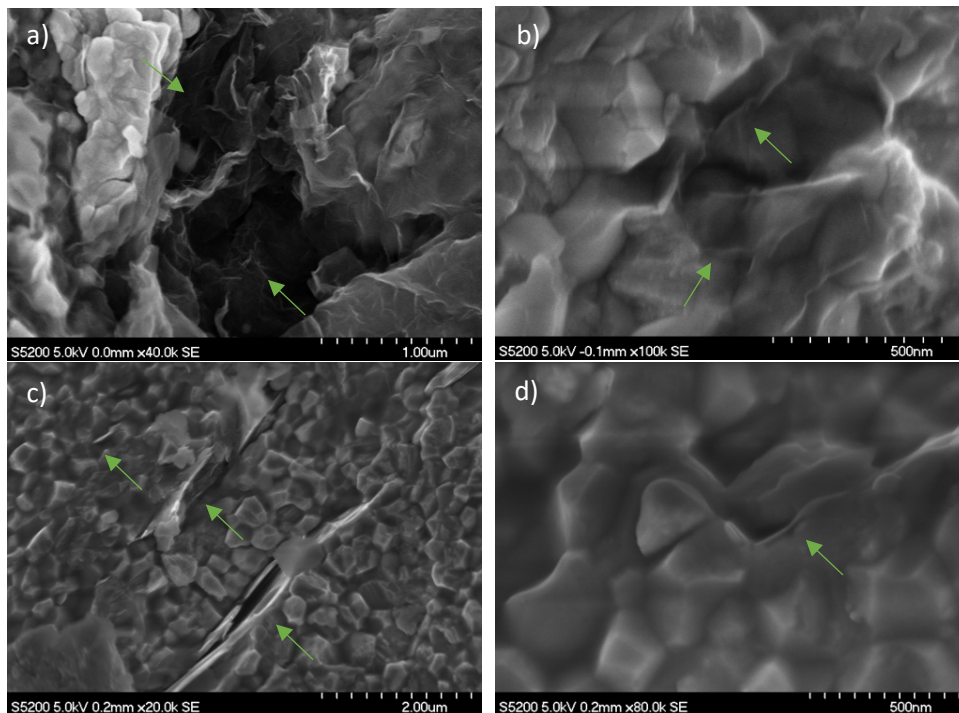**Problems with the sample impeded measuring

Fig.1. SEM micrographs of the fracture surfaces of the composites with the two different 2D nanomaterials: (a) and (b) 1 vol% FLGs, and (c) and (d) 1 vol% BNNSs.

Conclusions

We have achieved high densification of all composites. Samples having BNNSs show higher Vickers hardness whereas the ones incorporating FLGs are more anisotropic.

_____

Acknowledgements

References

[1] A. Bianco *et al.*, "All in the graphene family - A recommended nomenclature for two-dimensional carbon materials," *Carbon*, vol. 65. pp. 1–6, 2013.

[2] J.-H. Shin and S.-H. Hong, "Fabrication and properties of reduced graphene oxide reinforced yttria-stabilized zirconia composite ceramics," *J. Eur. Ceram. Soc.*, vol. 34, no. 5, pp. 1297–1302, 2014.

[3] A. Gallardo-López, I. Márquez-Abril, A. Morales-Rodríguez, A. Muñoz, and R. Poyato, "Dense graphene nanoplatelet / yttria tetragonal zirconia composites: processing, hardness and electrical conductivity," *Ceram. Int.*, vol. 43, no. 15, pp. 11743–11752, 2017.

[4] K. G. Zhou, N. N. Mao, H. X. Wang, Y. Peng, and H. L. Zhang, "A mixed-solvent strategy for efficient exfoliation of inorganic graphene analogues," *Angew. Chemie - Int. Ed.*, vol. 50, no. 46, pp. 10839–10842, 2011.

[5] D. Lee *et al.*, "Enhanced Mechanical Properties of Epoxy Nanocomposites by Mixing Noncovalently Functionalized Boron Nitride Nanoflakes," *Small*, vol. 9, no. 15, pp. 2602–2610, Aug. 2013.

[6] G. Sun, J. Bi, W. Wang, and J. Zhang, "Microstructure and mechanical properties of boron nitride nanosheets-reinforced fused silica composites," *J. Eur. Ceram. Soc.*, vol. 37, no. 9, pp. 3195–3202, Aug. 2017.

[7] G. Sun, J. Bi, W. Wang, and J. Zhang, "Enhancing mechanical properties of fused silica composites by introducing well-dispersed boron nitride nanosheets," *Ceram. Int.*, vol. 44, no. 5, pp. 5002–5009, 2018.

[8] V. Singh, D. Joung, L. Zhai, S. Das, S. I. Khondaker, and S. Seal, "Graphene based materials: Past, present and future," *Prog. Mater. Sci.*, vol. 56, no. 8, pp. 1178–1271, 2011.

_____

Key findings in the processing of ceramic composites made from zirconia and graphene based nanostructures

A. Gallardo-López[1*], C. López-Pernía[1], C. Muñoz-Ferreiro[1], C. González Orellana[1], A. Morales-Rodríguez[1], R. Poyato[2]

[1] Universidad de Sevilla, Departamento de Física de la Materia Condensada, ICMS, CSIC-Universidad de Sevilla, apdo. 1065, 41080 Sevilla, Spain, *angela@us.es
[2] Instituto de Ciencia de Materiales de Sevilla, ICMS, CSIC-Universidad de Sevilla, Avda. Américo Vespucio 49. 41092 Sevilla, Spain

Abstract

In this work, we have dealt with various key parameters to fabricate different graphene based nanostructures / tetragonal zirconia (GBN / 3YTZP) composites. GBN with number of layers ranging from 3 to ~150 have been used to prepare composites with a tetragonal zirconia matrix and a high GBN content (10 and 20 vol%). The number of graphene layers of the GBN has a great influence on the final composite homogeneity. Dry and wet powder-processing techniques, some of them including planetary ball milling have been used to prepare the composite powders, which have been densified by spark plasma sintering (SPS). The density, anisotropy and homogeneity of the composites along with the morphology and integrity of the graphene phase have been quantified and analyzed. The electrical conductivity of the composites with distinct microstructural features have also been approached. The high correlation between electrical properties with the GBN content and type and also with the processing technique has been explained by the microstructural features.

90

Keywords

Graphene based nanomaterials, zirconia (3YTZP), ceramic nanocomposites, SPS, electrical conductivity.

Introduction

Ceramic composites with graphene based nanostructures are currently generating a considerable interest in the scientific community due to the combination of properties of both phases, mainly: extremely large electric and thermal conductivity and Young's modulus of graphene versus refractoriness, inertness, resistance to corrosion, biocompatibility and inherent fragility of the ceramics. However, the properties of the composites can vary in a large range. The quality, dimensions, number of layers and content of the graphene-based phase, as well as the ceramic matrix chosen and the processing approach, sintering technique and sintering conditions of the composites are key issues to obtain specific properties. While the electrical conductivity and the fracture toughness in ceramic/graphene nanoplatelet (GNP) composites increase with GNP content [1], the hardness decreases for contents above a certain threshold content ~2 vol% GNP [2].

_____

The properties of GBNs depend strongly on the number of stacked graphene layers (thickness) and planar diameter. The cost of the GBN also depends on their thickness and the synthesis route. Therefore, the evaluation of the influence of the type of GBN used as fillers in ceramic composites not only can help to understand the composites' properties, but it can also be useful to control their fabrication cost.

One of the open and most difficult issues about the processing of these composites is achieving a high microstructural homogeneity, especially for high GBN contents, due to their high tendency to form agglomerates [3]. These agglomerates decrease the percolation degree of the GBN network, affecting the mechanical and electrical properties of the composites. For that reason, the mixing of the GBN with the ceramic powder before sintering is a critical step in the processing. Ultrasonic probe agitation for controlled time lapses improves de-agglomeration of GNPs without degrading them [2]. Although the combination of ultrasonication and planetary ball milling in isopropyl alcohol has been signaled as the most suitable routine for minimizing GBN agglomerates in Si_3N_4 composites, [4], dry milling avoiding the use of organic media will also be addressed in the present study to make the process eco-friendlier [5].

Sintering techniques with applied pressure are usually preferred to obtain fully dense composites as required for structural applications. Spark plasma sintering (SPS) is up to now the dominant method [2,6,7] since it reduces both the sintering time and the sintering temperature. Previous studies have shown that sintering conditions of 5 min holding time at 1250°C produce fully dense GBN/3YTZP composites with sub-micrometric ceramic grains and preserved GBN [2]. Due to the uniaxial pressure exerted on the powders during the sintering process, the two-dimensional GBN adopt a preferential orientation and the resulting composites exhibit anisotropic mechanical and electrical properties [7,8], which can be useful for functional applications.

The main goal of this work is to explore some of the mentioned main issues in GBN / 3YTZP composites, namely the content (10-20 vol%) and dimensions (3 layers – referred as few layer graphene, FLG-, 150 layers –referred as GNP-) of the GBN, the powder-processing conditions (dry vs wet) and the homogenization method (ultrasound agitation versus high-energy planetary ball milling). Relevant physico-mechanical and microstructural properties of the spark plasma sintered (SPS) composites, such as density, anisotropy, integrity of the graphene based nanostructures, homogeneity and electrical conductivity are assessed, giving valuable information concerning the composites' microstructure and their potential applications.

Results and discussion

Densification of the 3YTZP/GBN composites sintered by SPS (1250°C for 5 min) from the powders mixed with ultrasonic agitation and/or planetary ball milling was between 98-100% of the theoretical density, except those with 20 vol% FLG and dry milled 10 vol% GNP, with slightly lower density values ~95%. Thus, it seems that increasing GBN content from 10 to 20 vol% decreases densification of the composites with FLG.

91

_____

Table 1 compares the morphological parameters of the 3YTZP-GBN composite powders with 10 vol% GBN, mixed with the different techniques indicated in the table with those from the as-received FLG and GNP. The major (D_{maj}) and minor (D_{min}) diameter of the GNBs were obtained from SEM image analysis.

Table 1. Morphological and electrical parameters for the GBN and for the composites with 10 vol% GNP.

Filler	Mixing routines		GBN morphology		3YTZP grain morphology	Average conductivity	Electrical isotropy
	Ultras.	Milling	D_{major} (µm)	D_{min} (µm)	$d_{planar} \pm$ s.d. (µm)	σ (S/m)	$\sigma_{//} / \sigma_{\perp}$ (0-1)
FLG	Yes	No	≤ 10 [*]	0.01 [*]	0.14 ± 0.06	440 ± 20	0.1
GNP	Yes	No	≤ 4.3	0.2 -1.0	0.22 ± 0.10	128 ± 6	0.1
	Yes	Wet	≤ 3	0.14 - 0.56	0.30 ± 0.12	45 ± 4	0.1
	Yes	Dry	≤ 0.6	0.07 - 0.25	0.22 ± 0.10	230 ± 80	0.5
	No	Dry	≤ 0.6	0.10 - 0.26	0.18 ± 0.07	440 ± 30	0.9

[*] Data from the supplier.
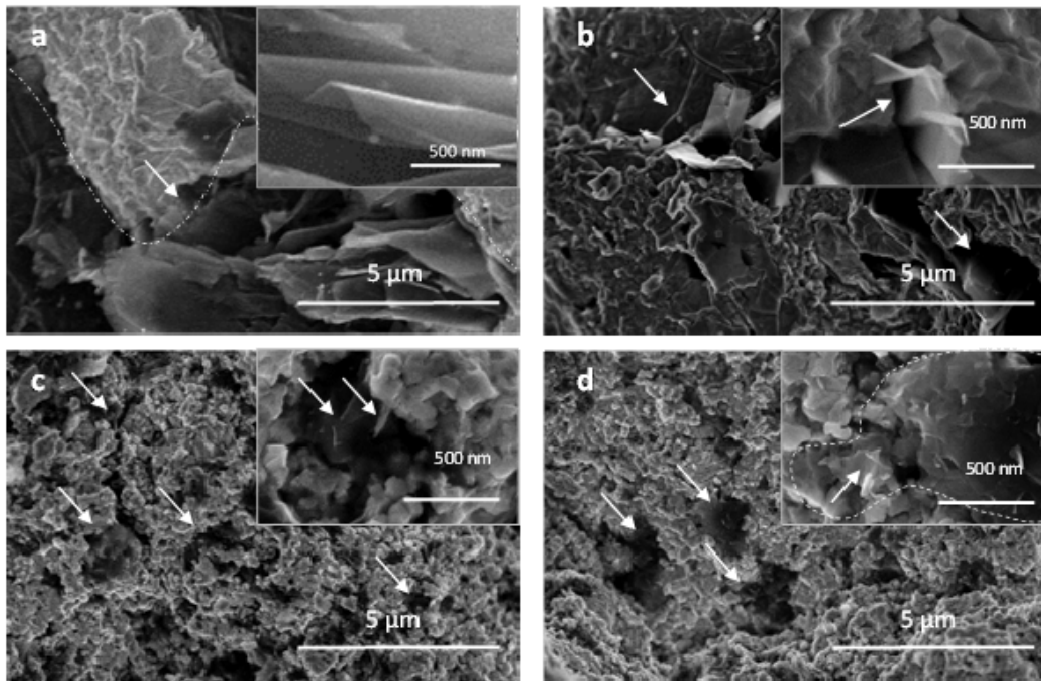
Fig.1. SEM micrograph showing the morphology of the ceramic grains and arrowed GBNs in composites with 10 vol% GNP processed with: (a) ultrasound probe (u.p.), (b) u.p. and wet milling, (c) dry milling, (d) u.p. and dry milling. The inserts show zoomed areas.

The results indicate that the high energy planetary ball milling of the GNP/3YTZP powder mixture reduces noticeably the average GNP agglomerate size, as it also can be observed in the scanning electron micrographs of fig. 2, improving homogeneity. Although composites with FLG are much more homogeneous than the ones with

GNP, the homogeneity of the high energy planetary milled composites with GNP is the highest. The improved GNB homogeneity results in a more effective grain growth inhibition in the composite and in an increase of the electrical conductivity.

Conclusions

Wet milling of 3YTZP-GNP composite powder achieves a 40% reduction in the GNP minor diameter, while dry milling is much more effective in reducing particle size (70%). When the GBN size decreases, an improvement in the percolation of the GBN network takes place, with a more homogeneous GBN distribution in the ceramic grain boundaries. This increases electrical conductivity, in the same way as by increasing the GBN content. The reduced lateral dimensions of the GNPs subjected to dry milling diminish their intrinsic anisotropy and produce electrical isotropic composites.

Acknowledgements

References

[1] J.-H. Shin, S.-H. Hong, Fabrication and properties of reduced graphene oxide reinforced yttria-stabilized zirconia composite ceramics, J. Eur. Ceram. Soc. 34 (2014) 1297–1302.

[2] A. Gallardo-López, I. Márquez-Abril, A. Morales-Rodríguez, A. Muñoz, R. Poyato, Dense Graphene Nanoplatelet/Yttria Tetragonal Zirconia Composites: Processing, Hardness and Electrical Conductivity, Ceram. Int. 43 (2017) 11743–11752.

[3] V. Singh, D. Joung, L. Zhai, S. Das, S.I. Khondaker, S. Seal, Graphene based materials: Past, present and future, Prog. Mater. Sci. 56 (2011) 1178–1271.

[4] M. Michalkova, M. Kasiarova, P. Tatarko, J.J. Dusza, P. Sajgalik, M. Effect of homogenization treatment on the fracture behaviour of silicon nitride/graphene nanoplatelets composites, J. Eur. Ceram. Soc. 34 (2014) 3291–3299.

[5] V.M. Candelario, R. Moreno, F. Guiberteau, A.L. Ortiz, Fabricating eco-friendly nanocomposites of SiC with morphologically-different nano-carbonaceous phases, J. Eur. Ceram. Soc. (2018).

[6] A. Centeno, V.G. Rocha, B. Alonso, A. Fernández, C.F.F. Gutierrez-Gonzalez, R. Torrecillas, A. Zurutuza, Graphene for tough and electroconductive alumina ceramics, J. Eur. Ceram. Soc. 33 (2013) 3201–3210.

[7] B. Román-Manso, E. Domingues, F.M. Figueiredo, M. Belmonte, P. Miranzo, Enhanced electrical conductivity of silicon carbide ceramics by addition of graphene nanoplatelets, J. Eur. Ceram. Soc. 35 (2015) 2723–2731.

[8] R. Poyato, J. Osuna, A. Morales-Rodríguez, Á. Gallardo-López, A. Gallardo-López, Electrical conduction mechanisms in graphene nanoplatelet/yttria tetragonal zirconia composites, Ceram. Int. (2018).

_____

Fabrication and characterization of a new calcium phosphate/PCL graded scaffolds in view of biomedical applications

C. Petit[1], J. M. Tulliani[1], P. Palmero[1], S. Meille[2], S. Tadier[2], J. Chevalier[2]

[1] *Department of Applied Science and Technology and INSTM Research unit PoliTO LINCE Laboratory, Politecnico di Torino, Corso Duca degli Abruzzi 24, Torino, Italy*
[2] *Université Lyon, INSA Lyon, MATEIS UMR CNRS 5510, Bât. Blaise Pascal, 7 Avenue Jean Capelle, Villeurbanne, France*

Abstract

Scaffolds for bone tissue engineering require a combination of bioactivity and biodegradation on the sample surface and high mechanical properties in the bulk. This work presents an original calcium phosphate (CaP)/polycaprolactone (PCL) scaffold with a gradation of composition and porosity fraction from bulk to surface. The scaffold is made of three layers: (i) a dense hydroxyapatite (HA)/β-tricalcium phosphate (β-TCP) core, (ii) a macroporous HA/β-TCP transition layer and (iii) a macroporous PCL/(HA/β-TCP) external layer. The gradation of composition and porosity consisted of a gradation of the HA/β-TCP weight ratio and an increase of volume fraction of pores. The core was first obtained by gel-casting. Then the transition layer was fabricated around the core by gel-casting combined with the use of porogens. After sintering of the two-layer samples, the outer composite layer was obtained by a solvent casting/particle leaching process. The microstructure, phase composition and biodegradation of the scaffolds were characterized. The gradation of porosity was clearly obtained. However, the gradation of phase composition was less pronounced due to an important decomposition of the HA phase into β-TCP during thermal treatment. An *in vitro* dissolution test was performed by immersing the scaffolds in a TRIS solution. The characterizations conducted on the immersed samples show a dissolution phenomenon with possible differentiated mechanisms in the different layers, in relation with the targeted multi-functionality.

Keywords

Calcium phosphate, Tissue engineering, Scaffold, Biodegradation

Introduction

Scaffolds for bone substitutes aim at favouring bone growth thanks to an interconnected macroporosity and bioresorption thanks to progressive dissolution of the materials [1]. Hydroxyapatite (HA) and β-tricalcium phosphate (β-TCP) have been extensively studied for this application [1] because they are biocompatible, osteoconductive and have a chemical composition close to the mineral part of bone. Biodegradable polymers/CaP composites have also been developed: poly-(ε-caprolactone) (PCL) is one of the aliphatic polyester mostly used for biomedical applications [2]. A high volume fraction of interconnected porosity favours bone colonization and vascularization of the implants [3] but decreases the mechanical

94

_____

properties. So, multifunctional implants are needed to combine sufficient mechanical resistance with bioactivity/bioresorbability. To fulfil these requirements, functionally graded materials (FGM) were developed with different layers with a gradation of properties. In this work, we have developed a new graded scaffold combining a gradation of composition and porosity, based on CaP and PCL. HA and β-TCP were combined for the ceramic phase to exploit the difference of properties between them [4]. Our scaffold is made of: (i) a dense BCP core, to supply the necessary mechanical strength (BCP1); (ii) an intermediate macroporous BCP layer, to join the dense ceramic and the porous composite layers (BCP2); (iii) an external macroporous PCL/BCP layer for a high bioresorption rate on the surface (PCL/BCP3). From the centre to the periphery, the HA/β-TCP ratio decreases. The two ceramic layers were made by gel-casting (combined with porogens for the porous intermediate layer) whereas the external composite layer was fabricated by solvent casting coupled to salt leaching. The microstructure and phase composition of each layer were characterized. Its bioresorption behavior was assessed by means of an *in vitro* dissolution test in a TRIS-buffered solution [5].

Results and discussion

Fig. 1a shows a scheme of the targeted graded structure which is overlapped with the experimentally developed scaffold, showing the good joining of the three different layers. The stereomicroscopy image in Fig. 1b highlights the continuous and crack-free interface between the two ceramic layers. Moreover, the comparison between the scheme and the picture in Fig. 1a shows that our approach was successful to produce a three-layer scaffold with good interfaces between the layers. In particular, the polymer adhered strongly to the ceramic porous layer. This is a key point for the structures developed in this work.

95

(a)   (b)
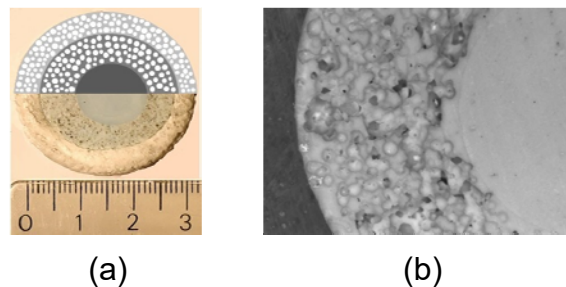
Fig. 1. (a) Digital picture (bottom part) and scheme (upper part) of the three-layer scaffold and (b) stereomicroscopy image of a polished surface showing the BCP1 and BCP2 layers

To characterize each layer in terms of composition and density, BCP1, BCP2 and PCL/BCP3 pellets were prepared with the same process as described above. The relative densities of the pellets were (80.1 ± 1.0) %, (34.6 ± 1.6) % and (23.8 ± 1.8) % for BCP1, BCP2 and PCL/BCP3 samples, respectively. Despite the incomplete sintering of the all-ceramic samples, a gradient of porosity was obtained from the

BCP1 to the PCL/BCP3 layer. The two processes used to prepare the porous layers are effective to obtain the expected volume fraction of pores. The phase composition was analysed by XRD (not shown). The two ceramic layers contain HA and β-TCP due to an important decomposition of HA during sintering. The HA/β-TCP weight ratios from XRD were 58/42 and 47/53 respectively. The XRD pattern of the PCL/BCP3 shows that the HA/β-TCP weight ratio is 32/68. Despite the HA decomposition, affecting especially the dense core, a gradation of composition through the layers was successfully achieved.

Fig. 2 shows the evolution of the three-layer scaffold's weight during immersion in TRIS. The samples underwent significant weight losses during the test. After 17 days of immersion, the samples lost around 13.9% of their initial weight. The measured weight losses prove that a dissolution phenomenon took place.
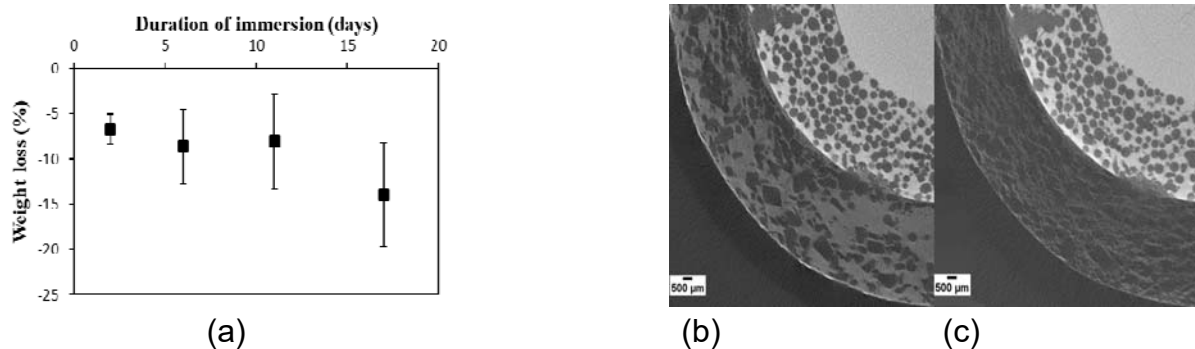

(a)   (b)   (c)

96

Fig. 2. (a) Evolution of the scaffolds' weight along the immersion test and slices of 3D images of a scaffold (b) before and (c) after immersion for 17 days in TRIS.

Slices of the 3D images (tomography) of a scaffold before and after 17 days of immersion are shown in Fig. 2b and 2c. After immersion, no significant changes were visible for the BCP1 and BCP2 layers, while the PCL/BCP3 layer was clearly less dense, as visible from the different gray levels in the external layer. Therefore, the images prove that the weight loss observed during the test mainly originated from the PCL/BCP3 layer. Despite the important dissolution of the external polymer layer, it is important to underline that even after 17 days of immersion, it was still joined to the ceramic part, further highlighting the effective interface between the two layers. Each scaffold was analyzed by XRD on the lateral (flat) surface of the cylindrical sample before and after immersion. The resulting XRD patterns characterized an average of the phase composition on the whole surface (i.e., including the three layers). Comparing the evolution of each scaffold before and after immersion, the HA/β-TCP weight fractions did not vary for immersion times of 2, 6 and 11 days. On the opposite, this ratio increased significantly after 17 days of immersion, suggesting the partial dissolution of the β-TCP phase. This is coherent with the known highest solubility of β-TCP, compared to HA [6].

Conclusions

In this work, a three-layer graded scaffold was successfully obtained via gel-casting and solvent casting/particle leaching processes. The aim was to obtain a gradation of composition and porosity from a dense core to a porous external layer. In addition, an external polymer layer was strongly joined to an inner ceramic one, being a strong point of innovation in this structure as compared to previous literature. Characterization of the scaffolds demonstrated a clear gradation of porosity between the layers, whereas the gradation of phase composition was less marked than the targeted one, because of the partial HA decomposition during sintering. An *in vitro* dissolution test was conducted by immersion of scaffolds in TRIS solution at 37°C for durations ranging from 2 to 17 days. Different signs of dissolution were found in the three layers. The results give some indications about different behaviors in the different layers. This fits with the targeted multi-functionality of the graded samples, with a bioresorbable external layer in contact with bone and a core devoted to the mechanical function.

Acknowledgements

References

[1] A.J. Wagoner-Johnson, B.A. Herschler, A review of the mechanical behavior of CaP and CaP/polymer composites for applications in bone replacement and repair, Acta Biomater. 7 (2011) 16-30.

[2] A. Baji, S.-C. Wong, T.S. Srivatsan, *et al*. Processing methodologies for polycaprolactone-hydroxyapatite composites: a review, Mater. Manuf. Process. 21 (2006) 211-218.

[3] A. Bignon, J.J. Chouteau, J. Chevalier, *et al.* Effect of micro- and macroporosity of bone substitutes on their mechanical properties and cellular response, J. Mater. Sci.Mater. Med. 14 (2003) 1089-1097.

[4] R.Z. LeGeros, S. Lin, R. Rohanizadeh, *et al.* Biphasic calcium phosphate bioceramics: preparation, properties and application, J. Mater. Sci. Mater. Med. 14 (2003) 201-209.

[5] T. Kokubo, H. Kushitani, S. Sakka, *et al.* Solution able to reproduce in vivo surface-structure change in bioactive glass ceramic A-W, J. Biomed. Mater. Res. 24 (1990) 721-734.

[6] S. Raynaud, E. Champion, J.P. Lafon, *et al.* Calcium phosphate apatites with variable Ca/P atomic ratio III. Mechanical properties and degradation in solution of hot pressed ceramics, Biomaterials 23 (2002) 1081-1089.

Promising strategies to improve the therapeutic effect of mesoporous bioactive glasses for bone regeneration

C. Pontremoli[1], E. Peretti[1], A. Bari[1], C. Vitale-Brovarone[1] and S. Fiorilli[1]

[1] *Department of Applied Science and Technology, Politecnico di Torino, Corso Duca degli Abruzzi 24, 10129 Torino, Italy*

Abstract

Over the last years, mesoporous bioactive glasses (MBGs) gained increasing interest as bone regeneration systems, due to their excellent bioactivity and ability to store and release therapeutic molecules. However, despite the significant progress in the design of advanced biomaterials, the treatment of bone defect still represents a challenging clinical issue. A severe limit to successful therapies is represented by the occurrence of bacterial infections. The development of biomaterials able to inhibit bacterial adhesion and, simultaneously, to stimulate pro-osteogenic effect could be a very promising strategy to face this challenge.

To this purpose, MBGs able to combine the effects of therapeutic ions/drugs with an antibacterial action are very promising candidates.

In this study, in order to impart specific biological functions and antibacterial potential, SiO_2-CaO based MBGs containing therapeutic ions (Cu^{2+}, Sr^{2+}) were synthesized in the form of nano- and micro-particles and, successively, loaded with drugs using two different incorporation methods (adsorption method and incipient wetness). With the aim to impart bacterial anti-adhesive properties to the MBG surface, zwitterionisation, which involves the functionalization with an equal number of surface positively and negatively charged moieties, represents a promising approach, thanks to the high amount of surface silanol groups. For this purpose, two functionalization routes were explored: the first one based on silane chemistry to graft primary/secondary amines to surface –OH groups and the second one involving the anchoring of amino acid molecules.

Samples were characterized through FE-SEM, EDS, N_2 adsorption-desorption measurement, FT-IR and TGA before and after drug loading. Functionalized MBGs were characterized through FT-IR, TGA, DLS and zeta potential analysis, to confirm the successful zwitterionisation of the surface.

In addition, the ability to release therapeutic ions/drugs and *in vitro* bioactivity (in terms of hydroxyapatite deposition) were evaluated.

Keywords

Mesoporous bioactive glasses, therapeutic ions, drug incorporation, zwitterionisation, bone regeneration.

Introduction

The use of organized mesoporous materials in biomedical applications is gaining increasing interest due to their well-defined nanoporous structures and their ability to store and release different molecules based on their nanopore size.

Furthermore, the high amount of free silanol groups present on mesoporous material surfaces allows to tune their hydrophilic/hydrophobic character and to impart stimuli-responsive and/or functional properties. In the field of advanced bioceramics, mesoporous bioactive glasses (MBGs), which combine the textural parameters of ordered mesoporous matrices with the properties of bioactive sol-gel glasses, have received increasing attention as bone-tissue regeneration systems [1].

More recently, the challenge is to provide them with further biological functions, including anti-bacterial activity and stimulation of osteogenesis and angiogenesis by addition of therapeutic ions and incorporation of drugs [2].

The resulting multifunctional nanocarriers are ideal candidates to develop novel smart devices able to simultaneously target all the causes that lead to compromised tissue healing. In view of the final application, the incorporation of these carriers into a vehicle phase based on thermosensitive hydrogels, in which an aqueous solution undergoes a sol to gel transition in physiological conditions (37 °C), represents an effective strategy to develop non-invasive devices that can be injected into the defect, and after gelling *in situ*, will consist of a depot for prolonged and localized release of ions and drugs [3]. However, despite the significant progress in the field of advanced biomaterials, a severe limit to successful therapies for bone regeneration is represented by the occurrence of bacterial infections. Therefore, the development of biomaterials able to inhibit bacterial adhesion and, simultaneously, to stimulate pro-osteogenic effect could be a very promising strategy to face this challenge. In this contribution, SiO_2-CaO based MBGs containing therapeutic ions (Cu^{2+}, Sr^{2+}) were synthesized in the form of nano- and micro-particles and successively, the MBG surface was functionalized, with the aim to impart bacterial anti-adhesive properties. To this aim zwitterionisation of MBGs, which involves the functionalization with an equal number of surface positively and negatively charged moieties, is reported to be a successful approach [4].

99

Results and discussion

MBGs based on the SiO_2-CaO system containing therapeutic ions (Cu^{2+}, Sr^{2+}) were prepared by a base-catalyzed sol–gel method and by an aerosol-based spray-drying process, in order to obtain nanoparticles and microparticles, respectively. FE-SEM images of the samples showed particles with a uniform, spherical morphology with size between 150 and 200 nm (Figure1, A1 and B1) for MBGs prepared by sol-gel procedure (MBG_Sr2%_SG and MBG_Cu2%_SG) and microspheres with size mostly in the range of 1-5 μm for spray-dried samples (MBG_Sr2%_SD and MBG_Cu2%_SD, Figure 1, A2 and B2).

EDS quantitative analyses revealed element concentrations very close to the theoretical ones. The specific surface area (SSA) and the pore size distribution were

detected by N_2 adsorption-desorption measurement. SG samples showed SSA around 800 m^2/g and uniform mesopores with a mean diameter of 4 nm, while SD samples exhibited SSA around 200 m^2/g and multi-sized pores ranging between 8 and 11 nm.
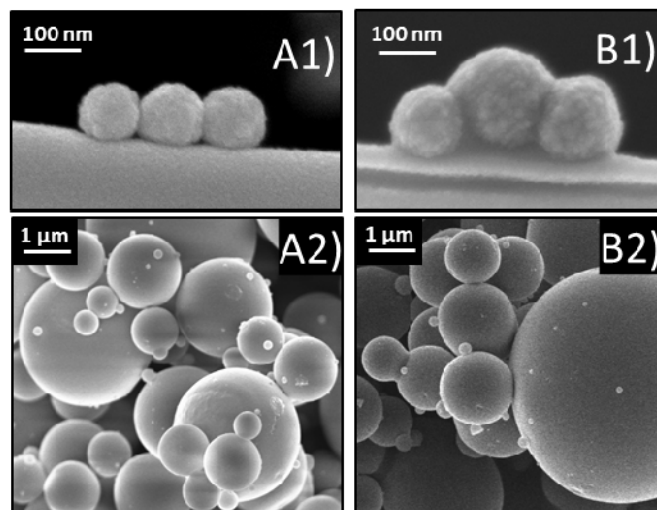
Fig.1. FE-SEM images of A1) MBG_Sr2%_SG; A2) MBG_Sr2%_SD; B1) MBG_Cu2%_SG; B2) MBG_Cu2%_SD.

Excellent bioactivity, in terms of hydroxy-apatite-like forming ability in SBF, was found for all MBG samples, showing that the incorporation of therapeutic ions did not affect the bioactive response. The release profile of Sr^{2+} and Cu^{2+} was obtained by inductively coupled plasma-atomic emission spectrometry (ICP-AES) analysis. The total amount of incorporated strontium was released with a final concentration of about 2.4 ppm and 7.2 ppm for SG and SD samples, respectively. Concerning Cu-containing samples, approximately the 60% of incorporated Cu^{2+} was released, suggesting the presence of a residual amount of copper into the MBG framework or the occurrence of re-precipitation phenomena.

Ibuprofen (ibu) loading into MBG pores, chosen as reference drug molecule, was conducted through two methods: the adsorption method (ads) and the incipient wetness method (IW). The presence of ibu in amorphous state into the pores was confirmed by FT-IR, DSC and XRD analysis. According to thermogravimetric analysis (TGA), about 8.5 mg (ads) and 12 mg (IW) of ibu per 100 mg of MBGs were loaded. SSA and pore volume decreased after ibu loading most likely due to the mesoporous channels being occupied by the presence of drug molecules. Drug release tests were performed in Tris-HCl and ibu was detected by HPLC: the total amount of incorporated drug was released.

Zwitterionisation procedures were performed on MBGs in order to provide them with bacterial anti-adhesive properties. Specifically, carboxyethylsilanetriol (CES) and (3-aminopropyl)silanetriol (APST), carrying a negative and a positive charge respectively, were grafted to surface –OH groups. Compared to bare MBGs, functionalized samples displayed a decrease in SSA and pore size distribution;

specifically, functionalized SG samples showed SSA of 554 m^2/g and pore size of 3.4 nm, whilst functionalized SD samples exhibited SSA of 73 m^2/g and pore size between 6.5 and 8.5 nm. Zeta potential values became less negative after functionalization; specifically, shifts from -28.5 mV to -12.5 mV and from -29.2 mV to -12.2 mV were observed for SG and SD samples, respectively. The amount of functional agents, according to TGA, was 9.26 mg/100 mg MBGs for SG samples and 7.29 mg/100 mg MBGs for SD samples. EDS quantitative analyses, XRD patterns, FE-SEM images and release profiles of ions in Tris-HCl buffer were not significantly affected by functionalization. The drug loading on zwitterionic MBGs was confirmed both by TGA and FT-IR analyses.

Conclusions

Sr and Cu-containing MBGs were synthesized by sol-gel and spray-drying procedures. Samples showed high surface area, excellent bioactivity, the ability to incorporate ibu and ion/drug release properties. In order to achieve a zwitterionic surface, able to impart bacterial anti-adhesive activity, functionalization procedures of MBGs were also carried out. The obtained multi-functional MBGs can be considered promising devices to improve the bone regeneration therapies.

Acknowledgements

101

References

[1] X. Yan, C. Yu, X. Zhou, J. Tang, D. Zhao, Highly ordered mesoporous bioactive glasses with superior in vitro bone-forming bioactivities, Angew. Chemie - Int. Ed. 43 (2004) 5980–5984.

[2] C. Wu, J. Chang, Multifunctional mesoporous bioactive glasses for effective delivery of therapeutic ions and drug/growth factors, J. Control. Release. 193 (2014) 282–295.

[3] C. Pontremoli, M. Boffito, S. Fiorilli, R. Laurano, A. Torchio, A. Bari, C. Tonda-Turo, G. Ciardelli, C. Vitale-Brovarone, Hybrid injectable platforms for the *in situ* delivery of therapeutic ions from mesoporous glasses, Chem. Eng. J. 340 (2018) 103–113.

[4] I. Izquierdo-Barba, M. Colilla, M. Vallet-Regí, Zwitterionic ceramics for biomedical applications, Acta Biomater. 40 (2016) 201–211.

Bioactive hybrid formulations for 3D printing of bone scaffolds

G. Montalbano[1], G. Molino[1], G. Ciapetti[2], S. Fiorilli[1], C. Vitale-Brovarone[1]

[1] *Politecnico di Torino, Department of Applied Science and Technologies, Corso Duca degli Abruzzi 24, Turin, Italy, chiara.vitale@polito.it*
[2] *Istituto Ortopedico Rizzoli, Laboratorio di Fisiopatologia Ortopedica e Medicina Rigenerativa, via G. C. Pupilli 1, Bologna, Italy, gabriela.ciapetti@ior.it*

Abstract

Pathological conditions such as osteoporosis often lead to severe bone fractures due to bone loss and deterioration. The currently in use pharmacological treatments aim to gradually reduce bone fragility but fail to restore the physiological balance between osteoblast (Ob) and osteoclast (Oc) activities [1]. For this reason, bone tissue engineering is now emerging as valid alternative, aiming to design biomaterials and scaffolds able to elicit a specific cell behavior. In this context, the objective of the ERC BOOST project is to design and develop smart bioactive scaffolds able to mimic the natural features of human bone in terms of composition, nanostructure and biochemical cues. Human bone samples provided by Istituto Ortopedico Rizzoli have been studied in order to detect the main differences between osteoporotic and healthy tissues. In addition, computed tomography analyses provided CAD/CAM models of healthy bone used to reproduce bone like scaffolds by means of a biofabrication platform. A bioactive hybrid formulation based on type I collagen and both strontium-doped mesoporous bioactive glass (MBG) and hydroxyapatite (HA) nanoparticles as inorganic phases has been optimized and characterized, with special focus on its suitability for 3D printing applications.

Rheological studies on collagenous suspensions clearly showed shear thinning and a fast sol-gel transition at 37°C. Preliminary 3D structures have been printed through 30 G needles in order to define the optimal printing parameters and conditions.

In order to better mimic the native structure of bone while improving the material stability after deposition, different cross-linking methods will be tested and compared.

The final 3D construct will also be able to provide biochemical signals due to the incorporation of different growth factors such as IGF-1 and TGF-β, naturally present in bone tissues.

Keywords

Bone tissue engineering; 3D printing; mesoporous bioactive glasses; type I collagen; bioactive materials

Introduction

Bone loss and deterioration experienced by osteoporotic subjects is the result of the impairment on the physiologic dynamic balance between bone resorption by osteoclasts (Oc) and bone deposition by osteoblasts (Ob). Up to now, pharmacological treatments aim to gradually increase bone mineral density and

102

decrease bone fragility, without restoring the physiological coupling between Ob and Oc [1]. Bone tissue engineering can thus be considered a potential solution to the increasing demand for healthy bone regeneration by means of biomimetic and bioactive constructs able to promote specific cell behavior [2]. Furthermore, the use of 3D printing technologies enables to step over the structure limitation while offering versatile and reproducible processes [3].

Based on these innovative concepts, the ERC BOOST project aims to design a biomimetic smart scaffold able to reproduce the natural bone architecture, topography and chemistry to restore the physiological balance between Ob and Oc activities.

In this contribution in order to investigate the main differences in the internal architecture of healthy and osteoporotic bone and obtain CAD models for the 3D printing of bone-like scaffolds, samples provided by Istituto Ortopedico Rizzoli have been analyzed by means of nanocomputed tomography (nanoCT) (Fig. 1).
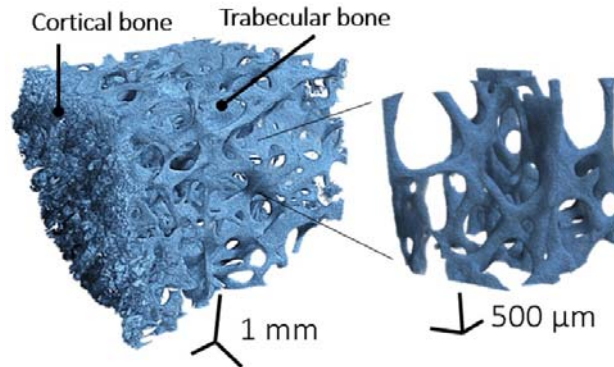
Fig. 1. CAD/CAM models of healthy bone derived from nanoCT analyses.

With the aim to mimic the natural composition of bone, bioactive hybrid systems based on type I collagen and both strontium-containing mesoporous bioactive glass and nanosized hydroxyapatite particles have been designed and characterized in order to investigate their physico-chemical and bioactive properties.

A comprehensive rheological study and preliminary printing tests have been conducted in order to prove the potential suitability of the hybrid material for the 3D printing of complex structures. Different crosslinking methods will be tested to increase the final mechanical properties of the printed constructs, while better mimicking the native structure of bone. Different growth factors, such as IGF-1 and TGF-β, will be incorporated in the final optimized structure to enable the release of biochemical cues.

Results and discussion
Computed tomography analyses showed a greater and less interconnected porosity, lower trabecular thickness and larger pores in osteoporotic bone samples compared to the structural properties of heathy bone.

Type I collagen dissolved in 0.5 M acetic acid was combined with both inorganic particles of pro-osteogenic strontium-containing mesoporous bioactive glasses (MBG_Sr) and hydroxyapatite nanoparticles (nanoHA) considering the volume percentage of the organic and inorganic phases in the natural bone tissues. Rheological analyses proved the pseudo-plastic behavior of the hybrid suspensions as well as the presence of a yield stress and a fast sol-gel transition due to the physical crosslinking of collagen at 37°C (Fig. 2).
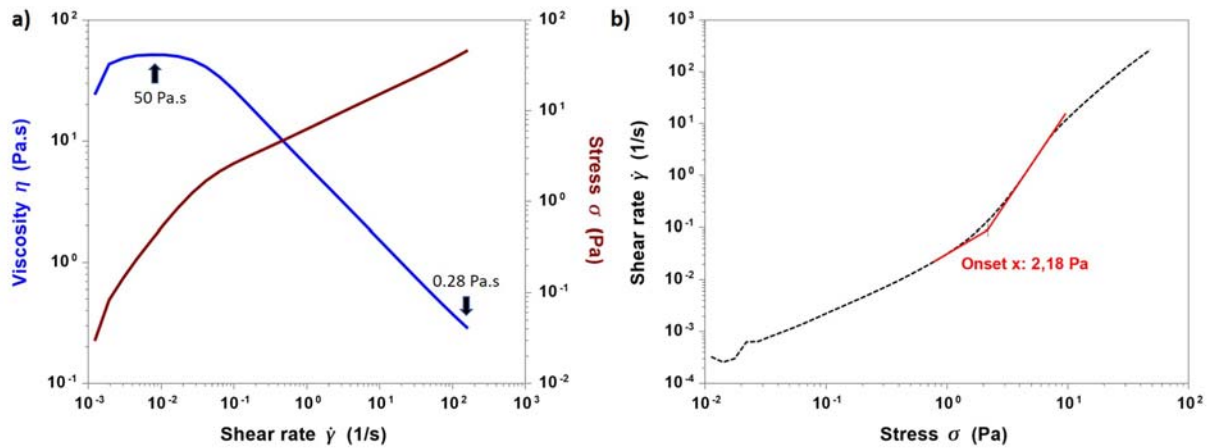

Fig. 2. Pseudo-plastic behavior (a) and yield stress (b) of collagen/MBG_Sr suspension at 4°C.

104

Field Emission Scanning Electron Microscopy (FE-SEM) images of solid samples clearly showed the reconstitution of collagen fibers and the homogeneous embedding of the inorganic particles in the fibrous matrix. Furthermore, samples incubated in Simulated Body Fluid (SBF) at 37°C up to 7 days displayed a great deposition of HA crystals, confirming the high bioactivity of the material [4].

The visco-elastic properties of the collagen-based suspensions enabled the successful printing of mesh-like constructs (10 x 10 x 1 mm) in a supporting gelatin bath (Fig. 3). 3D structures were realized by means of a BIOX 3D Bioprinter (CELLINK), using 30 G needles with an internal diameter of about 120 μm without showing needle clogging, proving the suitability of the hybrid systems for the potential printing of high-resolution complex structures. Despite the promising results obtained, further studies will be required to optimize both printing parameters and proper crosslinking methods to stabilize the final structures while increasing the printing fidelity.

Conclusions

Early studies conducted in the frame of the ERC BOOST project showed the relevant structural differences between osteoporotic and healthy bone samples, highlighting a more fragile structure for the osteoporotic bone. Homogeneous hybrid systems based on type I collagen combined with inorganic particles of both MBG_Sr and HA proved fast sol-gel transition at 37°C and high bioactivity properties. Rheological

_____

characterization and the successful printing of 3D mesh-like structures highlighted the potential of the developed collagen-based systems as promising bioactive materials for the 3D printing of complex bone-like scaffolds. As future activity, CAD models derived from nanoCT analyses on bone samples will be used to design biomimetic scaffolds and crosslinking methods will be investigated to provide the final printed structures with the required mechanical properties.
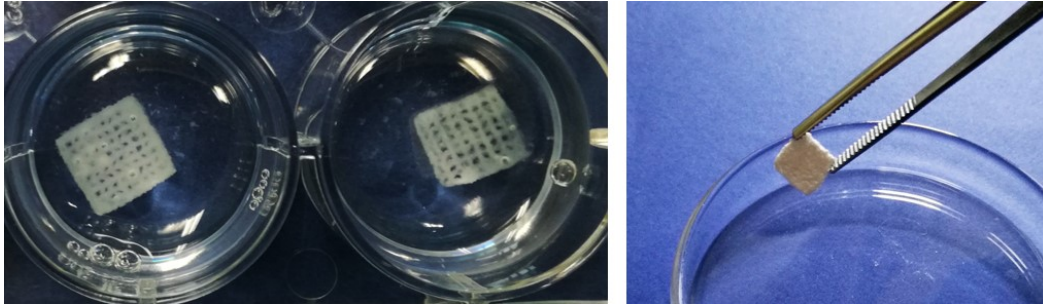
Fig. 3. 3D mesh-like structures printed by using a supporting gelatin bath.

Acknowledgements

105

References

[1] F. Jakob, R. Ebert, A. Ignatius, T. Matsushita, Y. Watanabe, J. Groll, H. Walles, Bone tissue engineering in osteoporosis. Maturitas *75* (2013), 118–124.

[2] J. M. Holzwarth, X. Ma. Peter, Biomimetic nanofibrous scaffolds for bone tissue engineering. Biomaterials 32.36 (2011): 9622-9629.

[3] F. P. W. Melchels, W. J. A. Dhert, D. W. Hutmacher, J. Malda, Development and characterisation of a new bioink for additive tissue manufacturing. Material Chemistry (2014), 2282–2289.

[4] G. Montalbano, S. Fiorilli, A. Caneschi, C. Vitale-Brovarone, Type I Collagen and Strontium-Containing Mesoporous Glass Particles as Hybrid Material for 3D Printing of Bone-Like Materials. Materials 11.5 (2018).

_____

_____

Comparison of microwave sintering of microsized and nanosized hydroxyapatite powders

P. Lefeuvre[1], A. Thuault[1], J.C. Hornez[1], A. Leriche[1], S. Hocquet[2]

[1] : *Laboratoire des Matériaux Céramiques et Procédés Associés, boulevard Général de Gaulle, 59600 Maubeuge, France*
[2] : *Belgian Ceramic Research Center, Av. Gouverneur E. Cornez 4, 7000 Mons, Belgium*

Introduction

Natural bones are mainly constituted by calcium phosphate minerals with several doping elements (Mg, F, …). Their porous structure is continuously broken down and rebuilt by cells (osteoblasts and osteoclasts respectively) in the form of nanosized crystals embedded in collagen (Figure 1). Therefore, the human bone is a continuously moving structure. It can repair itself up to a certain extent, from which medical treatment is needed. Amongst those treatments is the use of biocompatible ceramics like hydroxyapatite ($Ca_{10}(PO_4)_6(OH)_2$) (HA) characterized by a Ca/P ratio of 1.667 close to the human bone. Osteoclasts and osteoblasts (two type of cells in the organism) are able to metabolize hydroxyapatite (HA) and turn it into natural bone, making HA bioactive.
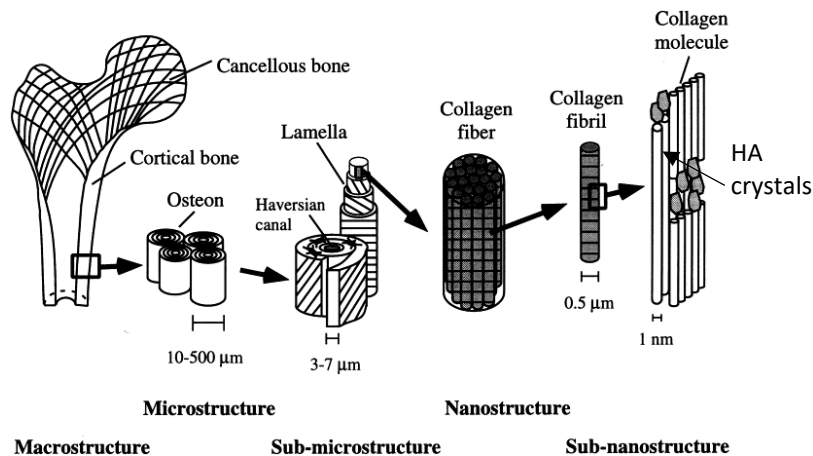
Fig. 1. Hierarchical structure of the human bone (Zioupos, 1998)

Thereby, HA is used in numerous appliances in the medical field: void fillers, implant coating and bone tissue engineering. Until now, those appliances are standardized, mass-produced and require long processing times. Today, there are two challenges in the bioceramics field: (1) to fabricate individually tailored prosthesis. For that, fast prototyping techniques such as 3d-printing or robocasting are being used (Guido Staffa, 2012); (2) to mimic the bone structure by using nanosized HA powders.

The production of customized prosthesis also needs shortened processing times and leads to the development of faster sintering techniques such as microwave sintering. Indeed, microwave sintering presents many advantages compared to conventional sintering: volumetric heating and good microwave absorption properties for HA

_____

_____

leading to a faster and more efficient sintering, as shown in figure 2. This figure present the grain size as a function of the density for HA samples sintered conventionally at different temperatures or by using a microwave sintering method with three different dwell times. 5 minutes dwelling time with microwave sintering gives higher density (99.6%) than a 5 hours dwell time by conventional sintering with a similar submicronic grain size. Moreover, such sintering time reduction allows a much lower energy consumption.
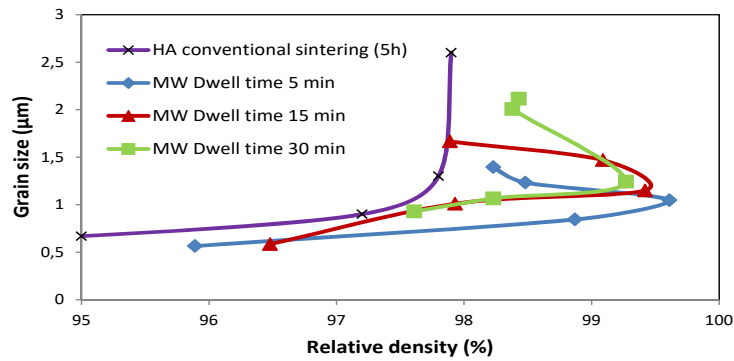

Fig. 2. Comparing microwave and conventional sintering

The microwave sintering is therefore an interesting way to densify customized scaffolds. The natural nanostructure of the human bone shows the interest to use nanosized HA powder in order to mimic the natural bone structure. So, nanosized HA powders are now commercially available.

The aim of this study is to apply the microwave sintering technique to a commercial nanosized powder and compare results with a micronized, laboratory-made powder.
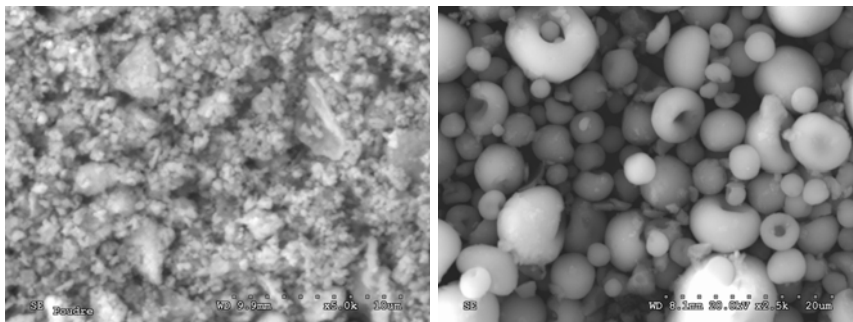
107

Fig. 3. SEM micrographs of M powder (left) and N powder (right)

Starting powders

Two hydroxyapatite powders were chosen for the purpose of this study. A microsized powder was synthesized by co-precipitation from diammonium phosphate and calcium nitrate precursors (Michel Descamps, 2012). After precipitation, the powder was calcined at 950°C and grinded for 12 hours to obtain the M powder (figure 3: SEM micrograph of the powder, with an agglomerate size of 3 μm). The influence of parameters such as the calcination temperature on the sinterability by microwave sintering was studied in a previous publication (A Thuault, 2014). The nanometric

_____

size powder was obtained by hydrothermal synthesis followed by spray-drying treatment to obtain handle able powder as shown by the SEM micrographs in figure 3b (donut shaped granulates with an average size of 10 µm). The X-Ray diffractogram (fig 4b) followed by Scherrer analysis show that both powders are well crystallized with a much smaller crystal size for the N powder (23nm) than for the M powder (150nm). The powder sinterability was tested by dilatometry assay (figure 4a shows the linear shrinkage as a function of time for both powders) with heating rate of 5°C/min up to 1300°C. For the M powder, a classical behaviour, with an expansion before sintering followed by 14% shrinkage at 1040°C has been observed. For the N powder, a 19% shrinkage is measured with a lower temperature for densification and a loss of water before 300°C. The different green densities (61% for the M powder, 56% for the N powder) explain the 5% shrinkage difference. Thermogravimetric analysis does not show any organic decomposition for the spray-dried powder which supposes that the spray drying treatment was carried out at a higher temperature than recommended.

Experimental

Pellets are made following the procedure: uniaxial pressing at 500kg for 60s followed by cold isostatic pressing at 2500 bars for 10 minutes. In the case of the spray-dried nanosized (N) powder, the uniaxial pressing step requires the use of a lubricant (stearic acid).

Microwave sintering is carried out using a Sairem 2KW single-mode resonant cavity (figure 5). The samples were held in a fibrous alumina box containing an annular SiC susceptor to initiate the HA heating. Sintering started at a power of 100W, and power was raised until it reaches 220-250W. Five sintering temperatures were investigated between 1190°C and 1270°C. Dwell times of 5, 15 or 30 minutes were chosen. To compare the results of microwave sintering with conventional sintering, M powder and N powders samples were conventionally sintered for 5 hours at 1210°C with a 5°C heating/cooling rate.
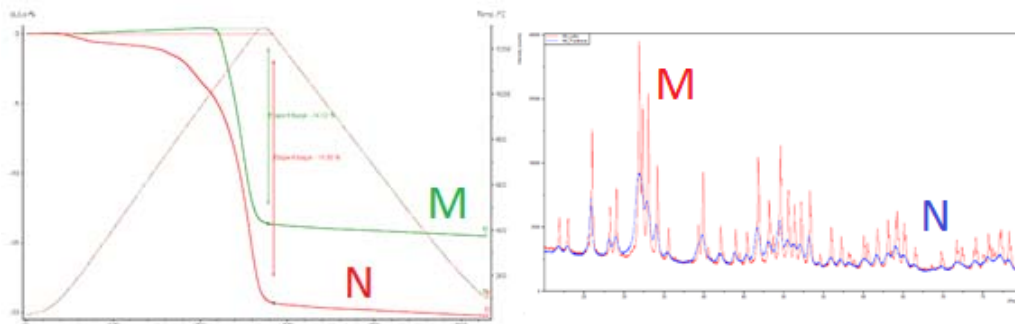
108

Fig. 4. Dilatometry of both M (green) and N (red) powders (a) and XRD of both powders (b)

The following characterization have been carried out:
- Grain size and microstructure analysis with a JEOL-JCM 6000 SEM after thermal etching for 10 minutes 80°C below the sintering temperature
- Density with Archimedes method (3 times on each sample)
- Phase purity with a PANalytical X-Ray diffractometer (20 to 80 degrees)
- Mechanical properties with a Zwick macro-indenter (30s of loading with 2N of force).

Results

Conventional sintering was carried out according to parameters previously used to sinter the M samples. However, all the samples made of nanosized (N) powders were damaged, a few of them suffered a catastrophic fragmentation. Microwave sintering allowed to produce mostly intact pellets, with a few of them presenting some cracks. The conclusion is that volumetric heating during microwave sintering allowed a more uniform temperature within the samples and reduced the heat-gradient induced stress.

Concerning the microwave sintering, densities of samples have shown (figure 6a) that the microsized powder requires higher sintering temperatures to reach densities similar to nanosized powder. The densities of nanosized powders are quite similar no matter the sintering time used. Two maxima of densities can be observed: sintering at 1210°C for 30 minutes or at 1230°C for 15 minutes.

Elastic modulus measurements (figure 6b) show that similar values between microsized and nanosized powders for larger dwell times.

109
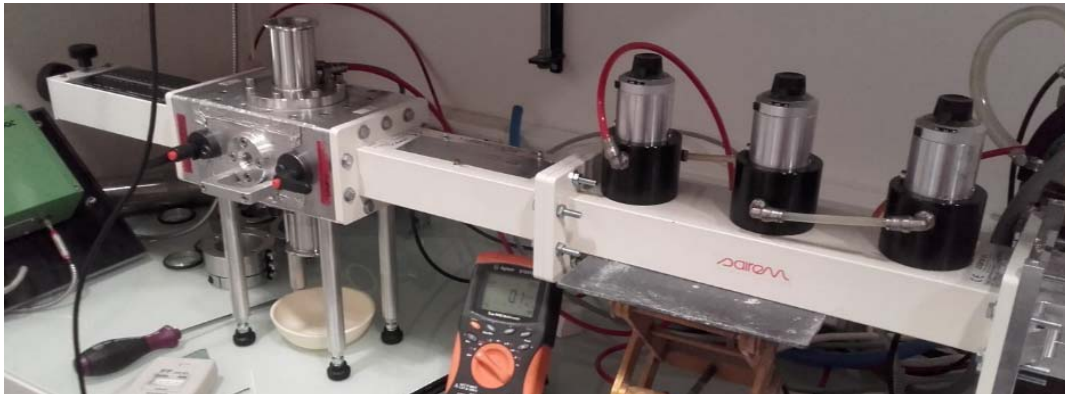
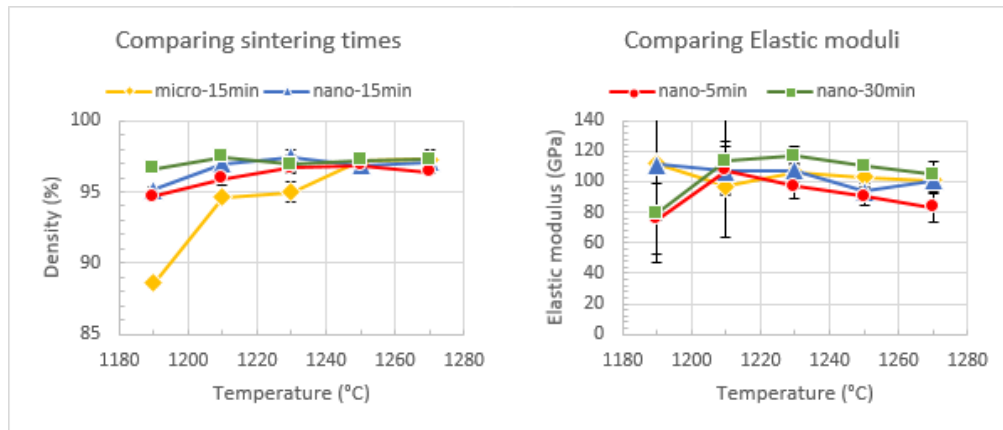*Fig. 5. Microwave sintering apparatus at LMCPA*

_____

Fig. 6. (a) Influence of sintering parameters on density; (b) influence of temperature on Young modulus.

Conclusion

This preliminary study has demonstrated the ability to microwave-sinter spray-dried nanosized HA powder. Densities and Young modulus values similar to microsized powder were obtained. Sintering conditions have to be adjusted to control the microstructure and mimic the natural bone structure.

References

Zioupos, J.-Y. R.-S. (1998). Mechanical properties and the hierarchical structure of bone. *Medical Engineering & Physics*, 92-102.

Guido Staffa, A. B. (2012). Custom made bioceramic implants in complex and large cranial reconstruction: A two-year follow-up. *Journal of Cranio-Maxillo- Facial Surgery*, 65-70.

Michel Descamps, E. M.-C. (2013). Processing and properties of biphasic calcium phosphates bioceramics obtained by pressureless sintering and hot isostatic pressing. *Journal of the European Ceramic Society 33*, 1263-1270

A Thuault, E. S.-C. (2014). Improvement of the hydroxyapatite mechanical properties by direct microwave sintering in single mode cavity. *Journal of the European Ceramic Society*, 1865-1871.

110

_____

Link between microstructure and compressive strength of lightweight building materials

J. Devillard [1, 2], R. Marull [1], X. Brajer [1], J. Adrien [2], S. Meille [2], E. Maire [2]

[1] *Saint-Gobain Recherche, Aubervilliers, France, julie.devillard@saint-gobain.com, roxane.marull@saint-gobain.com, xavier.brajer@saint-gobain.com*
[2] *Univ. Lyon, INSA Lyon, MATEIS UMR CNRS 5510, 23 Av. Jean Capelle, 69621 Villeurbanne, France, jerome.adrien@insa-lyon.fr, sylvain.meille@insa-lyon.fr, eric.maire@insa-lyon.fr*

Abstract

Reducing weight is an effective way of reducing the grey energy of plasterboards. However mechanical requirements are crucial, especially in terms of local resistance. Foamed gypsum, which is the core material of lightweight plasterboards, is thus tested with spherical indentation tests and its microstructure is analyzed thanks to 3D tomography. In order to understand precisely the compression behavior of foamed gypsum, *in situ* indentation tests are conducted using tomography and monitered by digital volume correlation.

Keywords

Gypsum, tomography, X-ray, in situ, spherical indentation, volume

Introduction

To reduce energy cost of manufacturing and transport, weight reduction of construction materials is a solution. In our case, a compromise between density and mechanical properties of lightweight plasterboards has to be found, particularly for its core material: lightweight gypsum. Mechanical requirement in terms of local resistance are indeed crucial in this case. Understanding of the relation between structure and mechanical properties is hence essential.

Results and discussion

Lightweight gypsum contains three levels of porosity: macro-pores (around 500 μm) obtained by foam introduction, meso-pores (around 50 μm) due to hemihydrate particles dissolution and micro-pores (around 1 μm) created during gypsum crystallization. This microstructure is observed by X-ray tomography and only macro-porosity and meso-porosity are visible as in Figure 1 (voxel size of 2 μm).

A method of image analysis has been developed. Segmentation is divided in two stages for the two porosity scales: local threshold according to the method of Li [1] for meso-pores and auto-threshold Phansalkar method [2] for macro-pores. Coalesced pores are then separated and measured with 3D watershed technique.

Homogeneity of the porous phase is also characterized by two different criteria. The first one is used on tomography scans with a 2 μm voxels resolution. It consists of measuring and plotting the distribution of local volume fraction of macro-pores [3].

Homogeneous samples have a monodisperse distribution of local volume fraction while heterogeneous samples have a distribution with several peaks (cf. Figure 2). The second homogeneity criterion uses the minimum path algorithm. It involves the calculation of the most energy saving path (or minimum path) for a fracture coming from one side of a 2D image to its opposite side. This algorithm is applied repeatedly on several slices of the volumes scanned with a 15 µm voxels resolution. The standard deviation of the minimum path cost gives an indication on the homogeneity of the macro-porosity.
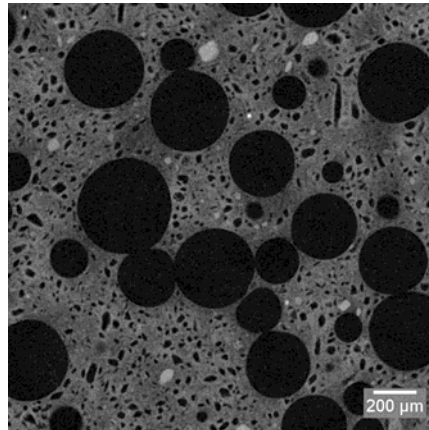

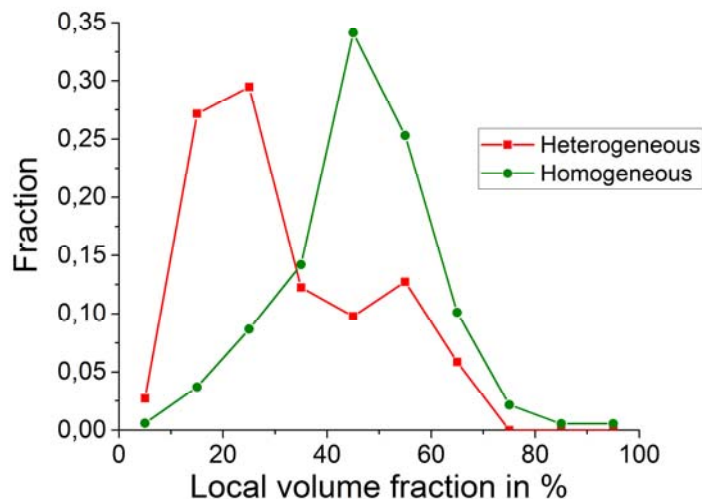*Fig. 1. Slice of a tomography volume with a voxel size of 2 µm*

112

Fig. 2. Example of two distributions of local volume fraction

Tomography also allows conducting *in situ* tests of spherical indentation. Displacement fields are measured by digital volume correlation in order to study and identify the material mechanical behavior [4]. The aim is to understand the behavior of the transition zone between the damaged and the undamaged material. Finite elements allow the simulation of this mechanical behavior from actual microstructure

containing the information of meso-porosity and macro-porosity. The link between mechanical properties and porosities distribution can then be determined.
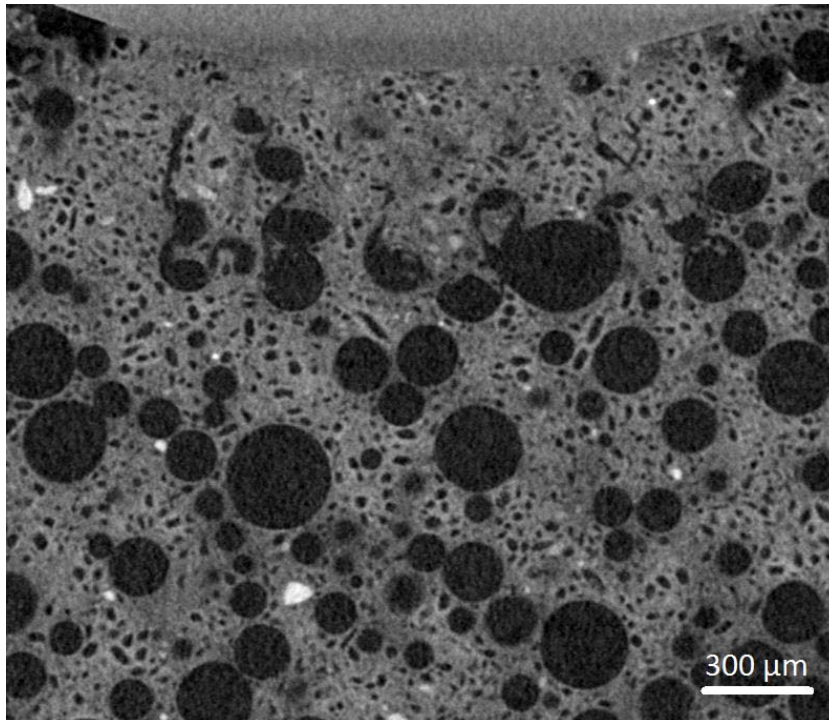

Fig. 3. In situ indentation test of foamed gypsum with a 6 mm diameter hard ball

113

Conclusions

The microstructure of foamed gypsum is finely analyzed thanks to the image processing of 3D tomography volumes. Moreover, the local resistance of this material has been tested with indentation tests in order to find a relation between the microstructure and the mechanical properties. Some *in situ* indentation tests have also been conducted with digital volume correlation monitoring (DVC). Displacements fields obtained by DVC and the foamed gypsum microstructure are then used as input data in a finite element modelling.

Acknowledgements

References

[1] C. Li & P. Tam, An iterative algorithm for minimum cross entropy thresholding, Pattern Recognition Letters, 8 (1998), 771-776
[2] Phansalkar N. & al., Adaptive local thresholding for detection of nuclei in diversity stained cytology images, International Conference on Communications and Signal Processing, (2011), 218-220
[3] A. Delarue & D. Jeulin, 3D Morpholigical Analysis of Composite Materials with Aggregates of Spherical Inclusions, Image Analysis & Stereology, 3 (2011), 153-161
[4] A. Bouterf & al., Identification of the crushing behavior of brittle foam: From indentation to oedometric tests, Journal of the Mechanics and Physics of Solids, 98 (2017), 181–200.

_____

Influence of biochar addition on mechanical properties of mortars

L. Restuccia[1,*], G. A. Ferro[1,°], J. M. Tulliani[2]

[1] *Politecnico di Torino, Department of Structural, Geotechnical and Building Engineering, Corso Duca degli Abruzzi, 24, 10129 Torino, Italy, *: luciana.restuccia@polito.it, °: ferro@polito.it*
[2] *Politecnico di Torino, Department of Applied Science and Technology, INSTM R.U PoliTO-LINCE Laboratory, Corso Duca degli Abruzzi, 24, 10129 Torino, Italy, jeanmarc.tulliani@polito.it*

Abstract

Concrete is a quasi-brittle material which, depending on its constituents, can be very strong in compression but usually also presents a low resistance in tension and consequently a limited bending strength. It has also a relatively low fracture toughness. Therefore, in this work, the influence on the mechanical properties of cementitious composites of the addition of sub-micronized pyrolized agricultural residues, specifically bamboo, peanut and hazelnut shells was investigated.

Keywords

Biochar, mechanical strength, toughness, crack deviation.

Introduction

114

Concrete is by far the most widely used man-made material in the world. However, it is a quasi-brittle material which, depending on its constituents, can be very strong in compression but usually also presents a low resistance in tension and consequently a limited bending strength. It has also a relatively low fracture toughness. Therefore, fibers have been added to concrete for almost 50 years to increase its tensile and flexural strength [1]. In the last years, carbon nanotubes [2], graphene [3], cellulose fibers [4] and $CaCO_3$ whiskers [5] have been also investigated to this aim. Although CNTs and graphene are ideal candidates because of their high specific surface area, low density and high aspect ratio, there are several major drawbacks that limit their use: among them, their still rather high production cost and their effective dispersion in cement matrix. Thus, the influence on cementitious composites' mechanical properties of the addition of sub-micronized pyrolized agricultural residues, specifically bamboo (PB), peanut (PS) and hazelnut shells (HS) was investigated.

Results and discussion

All the raw materials were first washed with tap water and dried in an oven for 48 hrs at 105±5°C. The washed and dried raw materials were then pyrolyzed in a quartz reactor at 850°C for 1 h under a constant flow of argon (0.2 bar pressure). Finally, the carbonized materials were manually ground in an agate mortar with an agate pestle, and then in ethanol to sub-micron scale by ball milling for 24 hrs, followed by 2 hrs of attrition milling. After grinding, the powders were dried in an oven at 50°C.

_____

Raman analyses were carried out on carbonized particles by means of a micro-Raman spectrometer (Olympus BH-2 UMA, Japan) equipped with a CCD detector. All the measurements were performed at room temperature.

Field emission scanning electron microscopy (FESEM, Hitachi S4000) was used to study the morphology and particle size distribution of the carbonized particles. The amount of carbonized nano/microparticles was 0.025, 0.05, 0.08, 0.2, and 0.5 wt% with respect to cement. Based on preliminary tests, the water to cement ratio (w/c) was kept constant to 0.35, while the superplasticizer (Mapei Dynamon SP1, Italy; modified acrylic based polymer) content was always fixed to 1.5 wt% with respect to cement. Four samples were prepared for each composition. Ordinary Portland cement (provided by Buzzi Unicem, Italy, Type-1, grade 52.5R) was used.

The carbonized particles and the admixture were added into the measured quantity of distilled water and the mixture was sonicated for 15 minutes. Then, the mixture was transferred into the mixing bowl (Janke and Kunkel homogenizer) while the cement was added gradually. The total mixing time was 4 min. After mixing, the cement paste was poured into polymethylmetacrylate molds ($20 \times 20 \times 75$ mm^3), which were then kept in closed plastic containers having 90% humidity for 24 h. Finally, the samples were demolded, weighed, labeled and cured in water for 28 days at room temperature.

Flexural strength was evaluated according to ASTM C348 (standard test method for flexural strength of hydraulic cement mortars) with a single column displacement controlled flexural testing machine (Zwick Line-Z010) with load cell capacity of 1 kN. The crack mouth opening displacement (CMOD) mode was used and a 0.003 mm/min rate was adopted. Prior to the flexural testing, 6 mm deep U-shaped notches were made in the specimens with a 2 mm thick diamond cut-off wheel. After the flexural testing, the portions of broken prisms were tested in compression according to ASTM C349 (standard test method for compressive strength of hydraulic cement mortars) with a displacement-controlled compression testing machine (Zwick Line-Z010) with load cell capacity of 100 kN. The displacement rate was kept at 0.50 mm/min and 0.80 mm/min for loading and unloading, respectively.

115

From FESEM observations, carbonized materials have an average diameter ranging from 600 to 800 nm. However, few particles up to 30 microns in size were sometimes observed too.

The Raman spectra of the carbonized materials showed a first peak of disorder band (D-band) at about 1350 cm^{-1} and a second peak related to graphitic band (G-band) at around 1600 cm^{-1}, characteristics of structurally disordered graphite materials. The intensity peaks ratios (I_D/I_G) of the materials were 0.78, 0.98 and 0.98, respectively for PB, PS and HS. These values are close to the ones of burnt wood (0.77) and of glassy carbon (0.91) [6].

FESEM observations also revealed that the carbonized particles were well dispersed in the cementitious matrix (Fig. 1). In addition, the rather limited presence of cement paste residue onto carbonized particles seems to indicate a weak adhesion between the pyrolyzed particles and the cementitious matrix.
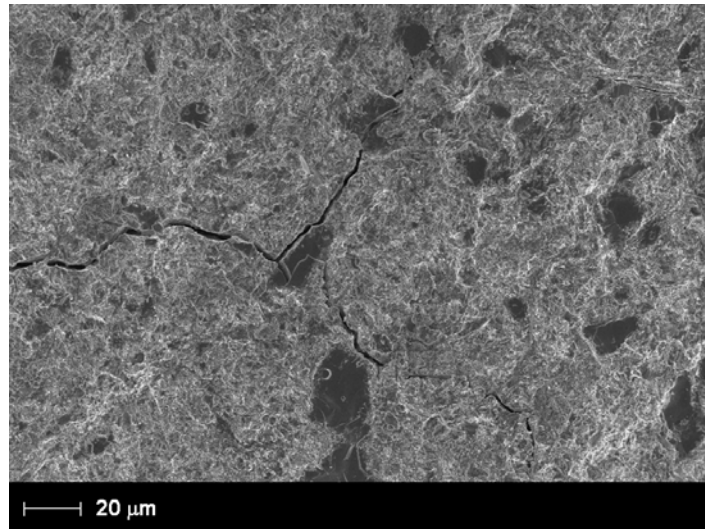
_____

Fig. 1. FESEM micrograph of a bamboo-based composite.

Generally, the modulus of rupture (MOR) of HS-cement samples and PS-cement samples were higher respect to PB composites (Fig. 2). This fact may be due to the nature of the pyrolyzed materials: in cementitious samples with PB particles more intragranular fractures were observed (Fig.1). The area under the stress-separation curve represents the total energy dissipated by fracture per unit area of the crack plane (G_F, J/m^2) [7]: fracture energy increased too with respect to plain cement samples after pyrolyzed particles addition.
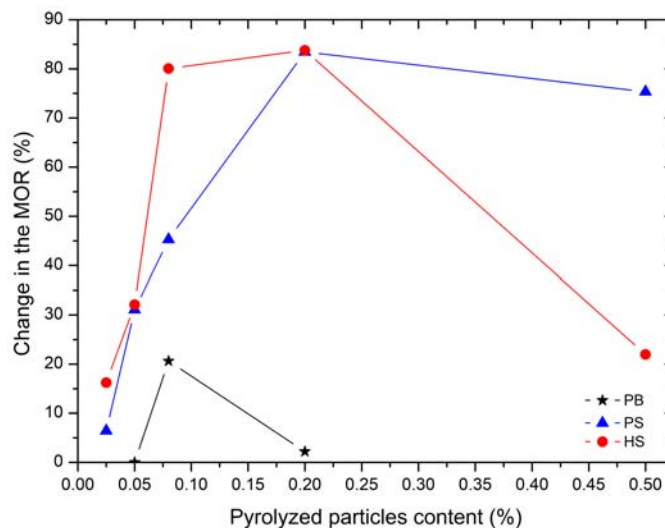
116

Fig. 2. Change in the MOR respect to plain cement in function of the pyrolyzed particles content.

In a material, cracks open or propagate when local stresses provide the energy necessary for rupture of material bonds and for the creation of fracture surfaces. In composite materials, when cracks face obstacles like aggregates, pores, voids and

_____

fibers, they are stopped and an increase of energy by increasing the external load is necessary for their further propagation [8]. Then, cracks may pass across these obstacles or may contour them to follow other paths along weaker regions [8]. In that case, cracks may be subdivided into several finer cracks, leading to crack branching because of an obstacle. Additional energy is also needed for breaking grains or for destroying the bond strength in the interface around them. Therefore, all kinds of inhomogeneities, which produce crack deviation, branching or multiplication increase the total area of fracture surface [8].

Conclusions

From FE-SEM observations it is evident that the presence of these small particles disturbs the propagation of microcracks that generally deviate their trajectory to follow the carbon nano/micro-particles contour. Crack pinning and crack branching are also other mechanisms that can explain the increase of toughness in the composite samples. Pyrolysis of organic wastes to produce biochar, to be used as additive in cement mortar, promotes waste recycling in cementitious composites in place of field amendment in agriculture. Finally, biochar has the potential to be successfully used as a carbon sequestering admixture in concrete constructions too [9].

Acknowledgements

References

[1] A.M. Brandt, Cement-based Composites, Materials, Mechanical Properties and Performance, Second ed., Routledge Editor, London and New York, 2009, p. 296.

[2] G.Y. Li, P.M. Wang, X. Zhao, Mechanical behavior and microstructure of cement composites incorporating surface-treated multi-walled carbon nanotubes. Carbon. 43, 6 (2005) 1239–1245.

[3] M.S. Konsta-Gdoutos, Z.S. Metaxa, S.P. Shah, Multi-scale mechanical and fracture characteristics and early-age strain capacity of high performance carbon nanotube/cement nanocomposites. Cem. Concrete Compos. 32, 2 (2010) 110–115.

[4] S.J. Peters, T.S. Rushing, E.N. Landis, T. Cummins, Nanocellulose and microcellulose fibers for concrete. Transportation Research Record. 2142 (2010) 25–28.

[5] M. Cao, C. Zhang, J. Wei, Microscopic reinforcement for cement based composite materials. Constr. Build. Mater. 40 (2013) 14–25.

[6] D.S. Knight, William B. White, Characterization of diamond films by Raman spectroscopy. J. Mater. Res. 4, 2 (1989) 385-393.

[7] V.C. Li, M. Maalej, Toughening in cement based composites. Part I: Cement, mortar, and concrete. Cem Concr Compos. 18 (1996) 223–237.

[8] A.M. Brandt, Cement-based Composites, Materials, Mechanical Properties and Performance, Second ed., Routledge Editor, London and New York, 2009, pp. 264–265.

[9] S. Gupta, H.W. Kua, C.Y. Low, Use of biochar as carbon sequestering additive in cement mortar, Cem. Concrete Compos. 87 (2018) 110-129